



Title	Formation dynamics of resident electron spin polarization and ensemble spin coherence in CdTe single quantum well
Author(s)	嚴, 麗平
Citation	北海道大学. 博士(工学) 甲第11878号
Issue Date	2015-03-25
DOI	10.14943/doctoral.k11878
Doc URL	http://hdl.handle.net/2115/58582
Type	theses (doctoral)
File Information	Yan_Liping.pdf



[Instructions for use](#)

DIVISION OF APPLIED PHYSICS GRADUATE SCHOOL OF ENGINEERING
HOKKAIDO UNIVERSITY



**Formation Dynamics of Resident Electron Spin
Polarization and Ensemble Spin Coherence in CdTe
Single Quantum Well**

A dissertation presented

by

LIPING YAN

Advisor: Professor Satoru ADACHI

2014

**FORMATION DYNAMICS OF RESIDENT ELECTRON SPIN
POLARIZATION AND ENSEMBLE SPIN COHERENCE IN CDTE
SINGLE QUANTUM WELL**

**A Doctoral Thesis Submitted to Hokkaido University
for the Doctoral Degree in Applied Physics**

by

Liping YAN

Advisor: Professor Satoru ADACHI

Division of applied physics

Graduate School of Engineering

Hokkaido University

Dec. 2014

ABSTRACT

The resident electron spin polarization (RESP) in quantum wells (QWs) has gained considerable attention for the potential applications of spin degree of freedom in the spintronic devices and quantum information processing. This is because of the optical controllability, the robust and long spin coherence free from the recombination annihilation. Therefore, massive research has been conducted on resident electron spin relaxation, transport, control, coherence, initialization, the interaction with other excited states, donors, lattice nuclei and so on, especially in GaAs and InAs QWs. Owing to these studies, the RESP can be better manipulated within the decoherence time after its generation. Unfortunately, it is almost a blank to the important spin formation dynamics in the initial temporal region, due largely to the ultrafast internal transitions and complicated many-body interactions. This issue, specifically, unclear initial phase, has been emphasized in our study with overcoming the problems successfully.

The formation dynamics of RESP and ensemble spin coherence in a naturally n-doped CdTe single QW have been studied with picosecond laser pulses by a time-resolved Kerr rotation (TRKR) method. The careful analysis of TRKR signals as compared to the theoretical fittings around time origin reveals the appealing phenomenon for the first time: a negative initial phase shift (IPS) in the precessional motion of RESP. After detailed experimental studies on the IPS of RESP, along with rate equations analysis, the theoretical model of the interplay between the excitons and RESP has been simulated. Consequently, the possibility of the negative IPS and of ensemble spin dynamics discussed gave a deep understanding of RESP generation, involving the formation and evolution of excitons, particularly in the elusive early time region.

The experimental Kerr signals with high precision both in time and phase show that the magnitude of IPS as well as the amplitude of RESP precession can be affected by external parameters such as excitation power, the strength of magnetic field. Such overall trends in the experiments agree well with the model calculations. Moreover, the negative IPS is almost constant for the pulse photon energy around the transition energy in resonance with trion. Through studying nonzero IPSs, we have confirmed the RESP formation dynamical process, associated especially with a fast asymmetric hole-spin flip in trions spin dynamics.

There is still a dominant remained obstacle characterized by hyperfine interaction (HFI), the coupling of electron spins to the lattice nuclear spins, although the particular benefit of RESP is the long lifetime of spin coherence without energy relaxation or forceful coupling with semiconductor environments. The HFI interaction was often ignored in the previous electron spin research of CdTe semiconductors. But the nuclear spin polarization (NSP) in an oblique magnetic field configuration has been evaluated after exploring the longitudinal and in-plane electron g factors precisely. This investigation indicates that RESP gives rise to a small effective nuclear field of a few mT.

This study makes the integral RESP formation process, initial behaviors and ensemble spin coherence well-established quite fully. Moreover, the IPS is founded to provide an important tool for researching into the spin dynamics of excitons. In a word, RESP performances with the feature of low nuclear field are preferred for spintronic devices that require the long ensemble spin coherence and the manipulation at rather low magnetic fields.

TABLE OF CONTENTS

LIST OF FIGURES	ix
LIST OF TABLES	xiv
LIST OF ABBREVIATIONS.....	xv
CHAPTER 1 INTRODUCTION	1
1.1 Background.....	1
1.2 Perspective and Motivation	4
1.3 Organization.....	6
1.4 References.....	8
CHAPTER 2 FUNDAMENTALS OF SPIN IN OPTICAL SEMICONDUCTORS	13
2.1 Spintronics Development.....	13
2.1.1 Brief Spin History	13
2.1.2 Spintronics	15
2.2 Band Structures in Zinc-blende Semiconductors.....	16
2.2.1 Bloch's Theorem	17
2.2.2 K•P Perturbation without Spin-orbit Interaction	18
2.2.3 K•P Model with Spin-orbit Interaction	19
2.3 Density of State.....	22
2.3.1 3D Density of State	23
2.3.2 2D Density of State	26
2.4 Spin Injection	29
2.4.1 Electrical Generation	29

2.4.2	Optical Initialization	30
2.5	Spins in the Bloch Sphere	32
2.6	Spin Polarization Detection	36
2.6.1	Polarized Photoluminescence	37
2.6.2	Hanle Effect	37
2.6.3	Pump-probe Faraday (Kerr) Rotation Techniques.....	38
2.7	Spin Relaxation.....	42
2.7.1	Longitudinal Time	42
2.7.2	Transverse Time.....	43
2.7.2.1	Homogeneous spin dephasing	45
2.7.2.2	Inhomogeneous spin dephasing.....	46
2.8	References.....	48
CHAPTER 3 EXPERIMENTAL SAMPLE AND METHOD		53
3.1	CdTe QW Sample.....	53
3.1.1	MBE Preparation	53
3.1.2	Crystal Structure	54
3.1.3	CdTe SQW and Confinement Effects.....	55
3.2	Carriers in the SQW Sample.....	57
3.2.1	Selection Rule of Heavy Hole and Light Hole in a SQW.....	57
3.2.2	Resident Electrons Density in a SQW	58
3.2.3	Photoluminescence (PL) Measurement	60
3.2.4	Neutral Exciton	62
3.2.5	Trion.....	63
3.3	Ultra-short Pulse	65
3.4	Precession under Magnetic Field	69

3.5	Experimental Fundamental Setup	71
3.6	References.....	76
CHAPTER 4 INITIAL PHASE SHIFT (IPS) OF RESP.....		79
4.1	Introduction.....	79
4.1	IPS Phenomenon.....	80
4.2	Theoretical IPS of RESP from Trion Dynamics.....	83
4.2.1	Model AI.....	85
4.2.2	Model AII.....	87
4.2.3	Model AIII	91
4.3	Theoretical IPS from Exciton Transformation Dynamics	94
4.3.1	Model BI	94
4.3.2	Model BII.....	97
4.4	Three Pulses Experiments.....	98
4.4.1	Experimental Setup.....	99
4.4.2	Dependence of IPSs on Control Power.....	99
4.5	Dependence of IPSs on Excitation Power	101
4.6	Dependence of IPSs on Magnetic Field.....	103
4.7	Dependence of IPSs on Excitation Photon Energy.....	105
4.7.1	Photon Energy Dependence under the Invariant Power	106
4.7.2	Energy Dependence with the Equal Amount of Photons.....	109
4.8	Signal Components during Carriers Evolution	111
4.8.1	Kerr Signal Components at Trion Resonance.....	111
4.8.2	Conversion of Excitons.....	114
4.9	Summary	116
4.10	References.....	118

CHAPTER 5 DYNAMIC NUCLEAR SPIN POLARIZATION	121
5.1 Nuclear Hyperfine Research Background	121
5.1.1 Nuclear Spin Research Review.....	121
5.1.2 Hyperfine Interaction Theory	124
5.2 Nuclear Spin Polarization Experiment	125
5.2.1 Overview of Experimental Techniques	125
5.2.2 Tilted Configuration.....	126
5.2.3 PEM Configuration.....	128
5.3 Experimental Results	129
5.3.1 G-factors	129
5.3.2 Nuclear Field on Magnetic Field Angle.....	132
5.3.3 Nuclear Field on Magnetic Field Strength and Pump Power	135
5.4 Theoretical Nuclear Field	136
5.5 Summary.....	138
5.6 References.....	139
CHAPTER 6 CONCLUSIONS AND OUTLOOK	144
6.1 Conclusions.....	144
6.2 Outlook	146
ACKNOWLEDGMENTS	148
LIST OF PUBLICATIONS	151

LIST OF FIGURES

Figure 2-1: The band structure for CdTe: Direct band gap transitions occur at the Γ -point [20].....	16
Figure 2-2: $\mathbf{K}\bullet\mathbf{P}$ band structures without spin-orbit coupling.	19
Figure 2-3: Energy dispersion curves near $k = 0$ for the conduction, heavy-hole, light-hole, and split-off bands.....	21
Figure 2-4: DOSs of 3D and 2D semiconductors.....	28
Figure 2-5: A schematic diagram illustrating the envelope functions, subbands and density of states of a typical square QW.....	29
Figure 2-6: Optical selection rules for dipole coupling states in the valence and the conduction band for CdTe. The states labeled by $ J, J_z\rangle$ represents their total angular momentum and z-component of spin angular momentum. The coupling transitions with σ^+ and σ^- circular polarized lights are indicated by green and blue arrows, solid for e-hh and dotted for e-lh.	31
Figure 2-7: Bloch sphere. The “up” and “down” eigen-states are just the vectors pointing to the north and south poles of the Bloch sphere. Moreover, all rest other points on the sphere represent the quantum-coherent super positions of these two eigen-states [45, 46].	35
Figure 2-8: Schematic of the Kerr effect. The polarization axis of linearly polarized light is rotated upon reflection from a birefringent material. This rotation angle is proportional to the magnetization along the direction of the light, which in turn is proportional to the difference in the index of refraction for right and left circularly polarized light.	40
Figure 2-9: Spin-induced Kerr rotation. The refractive indices are shown as a function of photon energy for right and left circularly polarized light. The shift between the two polarizations is due to the different absorption by spin-dependent state-filling. The difference of the refractive index is proportional to the Kerr rotation angle [56].	41
Figure 3-1: (a) Unit cell of a CdTe crystal; (b) 2-D representation of CdTe crystal: Cd and Te alternate through the lattice on their individual FCC sub-lattices.....	55

Figure 3-2: (a) The confinement energy bands for the QW sample used in our research. (b) The sample structure consisting of 10 nm CdTe well and Cd _{0.85} Mg _{0.15} Te barriers.	57
Figure 3-3: Schematic presentation of generation of carrier spin coherence by circular polarized laser pulses. The three cases differ with respect to the density of the 2DEG in the QW: (a) Empty well, only photo-generated carriers are present, which become bound to form excitons; (b) Low density of diluted resident electrons, trions with a singlet ground state are formed by a photo-generated exciton and a background electron. The interaction of the trion with the 2DEG is negligible; (c) Dense 2DEG with a Fermi energy exceeding the exciton binding energy. Bound complexes such as excitons and trions are suppressed [13].	60
Figure 3-4: PL spectrum excited at 1.65 eV at 10 K in the studied CdTe/(CdMg)Te SQW. Negative trion (T) and neutral exciton (X ⁰) are clearly separated. Excitation bandwidth is also indicated by a bar.	62
Figure 3-5: (a) Diagram of an exciton where an electron-heavy hole pair forms an e-hh particle like a hydrogen atom; (b) An exciton in the Band diagram. A electron and a hole are bound by the Coulomb attraction into excitons with a hydrogen-like spectrum.	63
Figure 3-6: (a) The trion which is made up of two electrons and a single heavy hole; (b) A trion in the Band diagram. Electrons and hole are bound by the Coulomb attraction into trions with a Helium-like particle.	64
Figure 3-7: Optical diagram of an auto-correlator. The input pulse is split into two parts, one of which is sent into a delay stage. Besides, they are recombined onto a nonlinear crystal for a second-harmonic generation. Scanning the time-delay of the two parts gives the SHG intensity as a function of delay time, which corresponds to the time-domain profile of the input light.	66
Figure 3-8: The calculated picosecond pulse of 1.96 ps (b) and its SHG autocorrelation trace (a). The SHG trace is fitted to a Gaussian curve (blue curve) with its FWHM = 2.77 ps.	68
Figure 3-9: (a) Zeeman effect in the non-magnetic QW under external magnetic field. Electron energy in the conduction band versus the magnetic field (B_x); (b) The spin vector is precessing over time about B_x .	71
Figure 3-10: A schematic of a time-resolved Kerr rotation setup. PBS refers to polarized beam splitter, P refers to polarizer and M refers to mirror. Other detailed illustrations are described in the text.	72
Figure 4-1: A typical TRKR signal (B_x = 146 mT and 10 K) and the fitting of RESP precession component (green solid line). Inset: the negative IPS ϕ of RESP is shown by a backward temporal shift ϕ/ω_L (P_{pump} = 1 mW).	81

Figure 4-2: Schematic of the RESP dynamics, where the interplay between resident electrons and optically excited negative trion is illustrated. (I) The electron spins with the non-polarized initial state are precessing around the magnetic field \mathbf{B}_x . (II) The e-hh (+1/2, -3/2) pair generated by a σ^- excitation captures an electron with -1/2 to form a negative trion and makes the net polarization in the resident electron ensemble. (III) Trion does not precess in the magnetic field, but its hole spin may flip during the trion recombination time (τ_r^T). (IV) The electron spin left behind by the trion recombination returns back to the ensemble of resident electrons. Moreover, it changes the net RESP and the initial phase.....	82
Figure 4-3: RESP building up from trions' formation and recombination. The detailed analysis is referred in the text.....	86
Figure 4-4: The dependence of calculated IPSs on Larmor frequency $\omega_L = 0 \sim 0.1$ rad/ps and recombination time $\tau_r^T = 10 \sim 85$ ps for Model AI system.....	87
Figure 4-5: Schematic AII of modeling RESP generation.	88
Figure 4-6: The dependences of theoretical IPSs on the relaxation time $\tau_s^T = 0 \sim 100$ ps and the recombination time $\tau_r^T = 0 \sim 110$ ps with the Larmor frequency $\omega_L = 0.0188$ rad/ps for Model AII system.....	90
Figure 4-7: Calculated IPSs (a) and RESP amplitudes (b) depending on Larmor frequency for Model AII system under the condition of $\tau_s^T = 0 \sim 60$ ps, $\omega_L = 0.001 \sim 0.10$ rad/ps.	91
Figure 4-8: Schematic AIII for modeling RESP generation.....	93
Figure 4-9: Schematic BI of modeling RESP generation based on the neutral excitons conversion. Also the schematic diagram displays the corresponding evolution of excitons based on the TRKR data in Figure 4-22 later.	95
Figure 4-10: Schematic BII of modeling the common conversion of neutral excitons to trions and RESP.....	97
Figure 4-11: A schematic of a three pulses TRKR setup. All the detailed illustrations are same as that in Section 3.5	99
Figure 4-12: TRKR signals obtained by both σ^- pumps of 10 mW and (a) σ^- or (b) σ^+ controls with different excitation power and the delay by $\pi/2$ (136 mT, 10 K). The dark dashed signal is a $\text{IPS} = 0$ curve as the reference. (c) The corresponding phase shifts from the fitting of the signals (a) (green) and (b) (red). Both the phase shifts almost converge to -0.38 rad in the limit of zero control power.....	101
Figure 4-13: (a) TRKR signals as a function of pump power (146 mT, 10 K). (b) Experimental IPSs (symbols) of RESP with varying pump power (the solid line is a guide for eyes). (c) The calculated IPS contour plot as functions of the recombination	

time τ_r^T and the hole spin relaxation time τ_{sh}^T . (d) The theoretical IPS as a function of τ_{sh}^T , which is a slice of (c) at $\tau_r^T = 85$ ps. 102

Figure 4-14: Experimental spin lifetimes (symbols) of RESP with varying pump power (the solid line is a guide for eyes), from the fittings of the TRKR signals. 103

Figure 4-15: (a) The dependence of the TRKR signals on B_x in the range of 35~716 mT at $P_{pump} = 8$ mW. (b) The corresponding IPS (solid circles), as well as the simulated IPS denoted by a solid line. (c) The corresponding relative amplitude (open circles) and the calculated amplitude denoted by a solid line. The calculated IPS and amplitude are plotted as a function of Larmor frequency under $\tau_{sh}^T = 15$ ps and $\tau_r^T = 85$ ps. The dashed lines in (b) and (c) are the guides for eyes. 104

Figure 4-16: TRKR signals for the different pulse photon energy under $B_x = 190$ mT. 106

Figure 4-17: The relative amplitude (black symbols) and the SDT (red line) curves of RESP as a function of pulse photon energy from the TRKR signals with the same pump power 3 mW. The pink and green vertical dashed lines are used to mark the resonant transition energy of trion and neutral exciton, respectively. 108

Figure 4-18: The photon energy dependence of IPSs (circular blue symbols). The pink and green dashed lines are used to mark the resonant transition energies of neutral trion and exciton, respectively. 109

Figure 4-19: The relative amplitudes (black symbols) and the SDTs (red circles) of RESP as a function of pulse photon energy for the TRKR signals excited by the pump with almost the equal amounts of photons. The pink and green vertical dashed lines are used to mark the resonant transition energy of neutral trion and exciton, respectively. 110

Figure 4-20: The photon energy dependence of IPSs (blue dots). The blue line is a guideline for eyes. The pink and green dashed lines are used to mark the resonant transition energy of the trion and neutral exciton, respectively. 111

Figure 4-21: (a) A general TRKR signal ($P_{pump} = 10$ mW; $B_x = 331$ mT and 10 K) denoted by the red symbols; the fitting of RESP precessional component (blue solid line) and the extend curve (green solid line) of extrapolating back to zero time delay for the fitting curve. (b) The simulated components of the heavy hole spin polarization of the trions (yellow curve), the z-component of RESP (blue plot), separately, and the combination of the two components (red line). 113

Figure 4-22: An example of the TRKR signal excited under the photon energy of 1.6146 eV above the neutral exciton resonant energy. 115

Figure 5-1: (a) Experimental tilted configuration and (b) its schematic illustration of tilted-field geometry under σ pump excitation with the tilted magnetic field by an angle of θ 128

Figure 5-2: Experimental PEM modulation configuration. All other detailed illustrations are same as that in Section 3.5 and Figure 4-14	128
Figure 5-3: (a) The magnetic field strength dependence of TRKR signals $S_K(t)$ in Voigt geometry; (b) Observed Larmor frequencies in different magnitude from 0 mT to 452 mT; (c) The dependence of T^* on the magnetic field in the same range. The solid curve indicates the expected values assuming the Gaussian distribution of g factor with the FWHM of $\Delta g = 0.009$	130
Figure 5-4: Effective g factor g_θ of RESP measured by using a PEM with different tilted angle θ of magnetic field. The solid line is a fitting curve according to Eq. 5-4 ..	132
Figure 5-5: TRKR signals after PEM (upper) and σ^- (lower) pump excited at $\theta = 18^\circ$, $B = 170$ mT, $T = 9$ K	133
Figure 5-6: (a) Larmor frequencies of RESP measured for PEM model and σ^- polarization excitations; (b) The effective nuclei magnetic field and its trendline for circularly polarized pump excitation at $T = 9$ K under the external magnetic field of 170 mT with different slope angle.....	135
Figure 5-7: (a) The nuclear field and its trend line for pump power 9 mW on the dependence of the external magnetic field strength with the tilted angle of $\theta = 15^\circ$; (b) The nuclear field and its trend line with the varying pump excitation power under the external magnetic field of 88 mT at $\theta = 15^\circ$	136

LIST OF TABLES

Table 1-1: Important Development History of Spin [2-6]	14
---	----

LIST OF ABBREVIATIONS

RESP	Resident electron spin polarization
SQW	Single quantum well
QWs	Quantum wells
TRKR	Time-resolved Kerr rotation
IPS	Initial phase shift
HFI	Hyperfine interaction
NSP	Nuclear spin polarization
NMR	Nuclear magnetic resonance
DNSP	Dynamic nuclear spin polarization
GMR	Giant magneto-resistance
DOS	Density of states
TRFR	Time-resolved Faraday rotation
TRKM	Time-resolved Kerr microscopy
MBE	Molecular-beam epitaxy
FCC	Face-centered cubic
PL	Photoluminescence
2DEG	Two-dimensional electron gas
T	Trion
X ⁰	Neutral exciton
SHG	Second Harmonic Generation; frequency doubling
CW	Continuous wave
FWHM	Full width at half maximum
BS	Beam splitter
QWP	Quarter wave plate
PEM	Photo-elastic modulator
ND	Neutral density
HWP	Half wave plate

WP	Wollaston prism
ONMR	Optical nuclear magnetic resonance

CHAPTER 1

INTRODUCTION

1.1 Background

Spin-based electronics or semiconductor spintronics has the potential to afford new device functionalities, to overcome the shortcoming of heating and power consumption, also improve the performances for the future spintronic devices, quantum information processing and quantum computation, compared to the charge current based devices [1, 2]. Electron spins are the crucial components of the spin-based semiconductor devices. Additionally, electron spins are expected to bring new functions at the same time with non-volatility and increased data processing speed [3]. In addition, the mature semiconductor technology also promises the large scale integration and incorporation for spintronics with other existing semiconductor devices. For this purpose, spin polarization with a sufficiently long coherence time must be brought in. Therefore, there has been a great deal of interest in the residual electron spin polarization (RESP) in quantum wells (QWs) and its spin dynamics in quantum nanostructures, because of the robust spin coherence required for the potential applications of the spin degree of freedom in the semiconductor devices and quantum information processing [4-7]. Although, the spin of a single electron particularly in QDs is a hotspot due to the application as a stationary qubit in quantum computers [8], the electron spin ensemble also plays a significant role in a distributed quantum networks for information storage [9]. In addition, the quantum

repeaters [10, 11] and the generation of entangled photon pairs [12] would be other applications of spin ensemble in quantum information processing.

We know a majority of quantum coherences experience a large of interactions with the surrounding semiconductor environment [13], which lead to that they are so delicate to survive on the order of picoseconds for the coherence time. However, by comparison, the excess electrons ensemble spins of the conduction band in a single quantum well (SQW) have the infirm coupling with the semiconductor environment [14], which makes for the coherence time on the order of nanoseconds sometimes. From the basic research perspective, the spin of the ensemble electron localized in a SQW has been considered to be promising carriers of quantum bit due to the expected unlimited lifetime and strong coherence property. By the way, the negative trion dynamic is one of the key features for residual electron spin related dynamic phenomena in a SQW.

Up to now, the extensive investigations only have been carried out a lot in III-V semiconductor compounds, especially in GaAs [15-20] and InAs [21] based structures, which have featured in numerous recent proposals for quantum computing and information processing. However, there was so far less work done in the II-VI semiconductors. For example, CdTe crystal is a II-VI semiconductor material that is usually used in X-ray and Γ -ray detectors and optoelectronic devices, due to its favorable optical properties and near-infrared direct band gap [22]. CdTe compound is also a feasible material for spintronics. Moreover, it has the same crystal structure but different material parameters with the III-V semiconductors, such as the lattice constant, spin-orbit coupling, effective masses, as well as importantly the smaller effects of HFI and strain due to the small abundance of the isotopes with nonzero nuclear spin [23, 24]. There are a

few reports of the spin dynamics via time-resolved Kerr rotation (TRKR) measurements at low temperatures and room temperature on CdTe-based semiconductor [25], which will be mentioned in detail below. To get a better understanding of carriers' spin dynamics in CdTe, we make a deep exploration in a single CdTe QW by means of TRKR technique in this dissertation.

Even the resident electron spin ensemble has a high coherence, there still is a dominant mechanism for the residual electron spin decoherence, namely, the HFI (the coupling of electron spins to nuclear spins). Therefore, we note that the lattice nucleus spin is an unavoidable factor for a number of interesting effects in a SQW, which has been studied over the past 50 years [26, 27]. The specific interest is the phenomenon attributable to the contact HFI, which couples the polarized electron spin in the conduction band to those of the nuclei. Through this interaction, optical excitation can result in the dynamic nuclear polarization (DNP) for nuclear moments in QWs [28] to replace the detection of nuclear magnetic resonance (NMR) with a sensitivity several orders of magnitude larger than that conventional methods provided [29-31]. Therefore, the hyperfine coupling of electronic and nuclear spins enables all-optical DNP measurement via electron spins [32, 33]. What is more, the CdTe nanostructures provide a promising medium for the application of their favorable electronic properties without strong hyperfine interactions. Although the decoherent effect of electron spins caused by nuclear spins has been ignored in some works [34, 35], in this dissertation, a nuclear spin polarization (NSP) has been evaluated precisely to study the resident electron spin dynamics wholly.

Ultrafast optical techniques have enabled the precise manipulation and sensitive detection of coherent spin dynamics in semiconductors. This technology for studying spin dynamics in semiconductors is to use the circularly-polarized light to optically orient non-equilibrium electron spin with relatively high spin polarization and to measure the steady-state circular polarization. Furthermore, pulsed methods allow for the measurements of resonant spin amplification [36] and frequency modulated spin precession [37]. From the TRKR measurement, we also can be able to identify the primary electron spin dynamical mechanisms [38-40] and observe the polarization of nuclear spins [2, 41, 42] in a QW with the graded material compositions.

1.2 Perspective and Motivation

There are more and more touchable novel quantum systems in laboratories with the developing physical theories and technologies, such as, the micro level system of semiconductor quantum dots (QDs) [43-48], QWs [46, 49, 50], and quantum wires [51, 52], the macroscopic system of Bose-Einstein condensate of atoms [53, 54]. In all of these systems, the coherent quantum spin effects have recently been investigated. Then they could adapt themselves to be used as quantum logic devices based on quantum mechanics corresponding to the traditional charged logic devices [55]. However, some relative fundamental problems have to be investigated thoroughly before these systems are used for the real quantum computation. For instance: how to handle with the quantum dynamics with a long coherence time for realizing the desired quantum logic operations; how to clarify the formation and decoherence processes of the carriers which play key roles on the quantum operations.

In order to improve the general understanding of the quantum properties of spin dynamics from many-body interactions in complex environments, as well as to provide inspirations for new spintronic research avenues and device applications hopefully, the mesoscopic system of a single semiconductor QW is used to intend to obtain the knowledge of spin dynamics for ensemble electron spins by focusing on the RESP initial spin dynamics and its evolution and the excitons spin dynamics in this dissertation.

As mentioned above, the resident electron without recombining with holes, as a kind of carrier itself, is very advantageous in maintaining a longer spin-polarized state. On the other hand, the resident electron spins have a high coherence in the potential well confinement [56]. By the way, the resident electron ensemble is considered to be capable of easily generating a spin polarization selectively [2]. Therefore, our interests have been focused on the II-VI material-CdTe QW nanostructure with a large binding energy, which has exhibited potentials for quantum applications of the ensemble electron spins in the information processing realized by ultra-fast laser techniques. The TRKR measurement method is used to measure the spin polarization over time directly. Therefore, the mostly creative focuses in this work are placed on the following points:

1. The formation and initial dynamical process about RESP, as well as the dynamical evolutions of negative trions and neutral excitons under an external magnetic field had to be figured out clearly by the experimental results and theoretical simulations.
2. The relation between RESP and negative trions was to be studied fully by ultrafast optics techniques. The initial characters of RESP would be determined by spin dynamics of trions, even that from excitons' transformation.

3. For the third purpose, the formation of nuclear spin-polarized state was raised by the parallel components of RESP in the direction of external magnetic field, which can reflect the knowledge about the generation of dynamic nuclear spin polarization (DNSP) through the HFI between the nuclear spin and RESP. The effective nuclear field magnitude would be used to make and evaluate the RESP decoherence caused by DNSP through measuring the Larmor frequency variation of RESP precessions.

1.3 Organization

As mentioned above, most of this dissertation deals with the quasi two-dimensional electrons trapped in a single CdTe QW. For attaining a better understanding of the ensemble resident electron spin dynamics, firstly, we have acquired the exact information about its structure and energy levels. Secondly, we perform TRKR measurements on the SQW sample and discuss electron spin dynamics, excitons' spin dynamics based on theoretical models involving the initial phase shift (IPS) in the RESP precessional motion, as well as HFI with nuclei spins.

The outline of the work presented in this dissertation is as follows:

Chapter 2 contains a brief introduction to the relative fundamental concepts of spin followed by a more detailed discussion of band energy, the density of states, spin initialization and the spin interactions in the zinc-blende nanosemiconductors.

Chapter 3 details the CdTe QW sample and TRKR experiments that generating arbitrary RESP profiles and detecting them with a double lock-in technique under the applied magnetic field.

Chapter 4 covers the RESP temporal evolution and presents the trion and excitons' formation. We discussed the dependences of IPS in RESP precession on the pump power,

magnetic field and photon energy, then shifted the discussions to the trions dynamics. Finally, the intrinsic properties of RESP and trions such as their formation dynamics, evolution and oscillator strength dynamics have been analyzed from experimental and theoretical points.

Chapter 5 demonstrates the contact HFI and the effective field of lattice nuclei spin. The demonstration of the weak coupling of electron spins to nuclear spin system is presented.

Finally, chapter 6 contains the conclusions and a discussion of possible directions for future work.

1.4 References

- [1] S. A. Wolf, D. D. Awschalom, R. A. Buhrman, J. M. Daughton, S. von Molnar, M. L. Roukes, et al. Spintronics: A spin-based electronics vision for the future[J]. *Science* 2001; **294**: 1488-1495.
- [2] M. I. Dyakonov. Spin Physics in Semiconductors[B]. Berlin: Springer; 2008.
- [3] D. Awschalom, D. Loss, N. Samarth. Semiconductor spintronics and quantum computation[B]. Berlin ; New York: Springer; 2002.
- [4] W. H. Lau, M. E. Flatte. Tunability of electron spin coherence in III-V quantum wells[J]. *Journal of Applied Physics* 2002; **91**: 8682-8684.
- [5] S. Crankshaw, F. G. Sedgwick, M. Moewe, C. Chang-Hasnain, H. L. Wang, S. L. Chuang. Electron Spin Polarization Induced by Linearly Polarized Light in a (110) GaAs Quantum-Well Waveguide[J]. *Phys. Rev. Lett.* 2009; **102**: 206604.
- [6] M. M. Glazov. Coherent spin dynamics of electrons and excitons in nanostructures (a review)[J]. *Phys. Solid State* 2012; **54**: 1-27.
- [7] A. Tackeuchi, T. Kuroda, S. Muto, Y. Nishikawa, O. Wada. Electron spin-relaxation dynamics in GaAs/AlGaAs quantum wells and InGaAs/InP quantum wells[J]. *Jpn. J. Appl. Phys.* 1999; **38**: 4680-4687.
- [8] D. Loss, D. P. DiVincenzo. Quantum computation with quantum dots[J]. *Physical Review A* 1998; **57**: 120-126.
- [9] H. J. Kimble. The quantum internet[J]. *Nature* 2008; **453**: 1023-1030.
- [10] L. M. Duan, M. D. Lukin, J. I. Cirac, P. Zoller. Long-distance quantum communication with atomic ensembles and linear optics[J]. *Nature* 2001; **414**: 413-418.
- [11] F. Bussieres, N. Sangouard, M. Afzelius, H. de Riedmatten, C. Simon, W. Tittel. Prospective applications of optical quantum memories[J]. *Journal of Modern Optics* 2013; **60**: 1519-1537.
- [12] M. Zwierz, P. Kok. Applications of Atomic Ensembles in Distributed Quantum Computing[J]. *International Journal of Quantum Information* 2010; **8**: 181-218.
- [13] A. P. Heberle, W. W. Ruhle, K. Ploog. Quantum Beats of Electron Larmor Precession in Gaas Wells[J]. *Physical Review Letters* 1994; **72**: 3887-3890.

- [14] J. M. Kikkawa, D. D. Awschalom. Resonant spin amplification in n-type GaAs[J]. Phys. Rev. Lett. 1998; **80**: 4313-4316.
- [15] K. Akiba, T. Yuge, S. Kanasugi, K. Nagase, Y. Hirayama. Optically induced nuclear spin polarization in a single GaAs/AlGaAs quantum well probed by a resistance detection method in the fractional quantum Hall regime[J]. Phys. Rev. B 2013; **87**: 235309.
- [16] I. Y. Gerlovin, Y. P. Efimov, Y. K. Dolgikh, S. A. Eliseev, V. V. Ovsyankin, V. V. Petrov, et al. Electron-spin dephasing in GaAs/Al_{0.34}Ga_{0.66}As quantum wells with a gate-controlled electron density[J]. Phys. Rev. B 2007; **75**: 115330.
- [17] T. Takahashi, S. Matsuzaka, Y. Ohno, H. Ohno. Optical detection of zero-field spin precession of high mobility two-dimensional electron gas in a gated GaAs/AlGaAs quantum well[J]. Physica E-Low-Dimensional Systems & Nanostructures 2010; **42**: 2698-2701.
- [18] C. R. Bowers, J. D. Caldwell, G. Gusev, A. E. Kovalev, E. Olshanetsky, J. L. Reno, et al. Dynamic nuclear polarization and nuclear magnetic resonance in the vicinity of edge states of a 2DES in GaAs quantum wells[J]. Solid State Nuclear Magnetic Resonance 2006; **29**: 52-65.
- [19] D. W. Snoke, W. W. Ruhle, K. Kohler, K. Ploog. Spin flip of excitons in GaAs quantum wells[J]. Phys. Rev. B 1997; **55**: 13789-13794.
- [20] S. Adachi, T. Miyashita, S. Takeyama, Y. Takagi, A. Tackeuchi. Exciton spin dynamics in GaAs quantum wells[J]. Journal of Luminescence 1997; **72-4**: 307-308.
- [21] S. S. Krishtopenko, V. I. Gavrilenko, M. Goiran. Spin-wave excitations and electron spin resonance in symmetric and asymmetric narrow-gap quantum wells[J]. Phys. Rev. B 2013; **87**: 155113.
- [22] R. K. Katiyar, S. Sahoo, A. P. S. Gaur, A. Singh, G. Morell, R. S. Katiyar. Studies of photovoltaic properties of nanocrystalline thin films of CdS-CdTe[J]. Journal of Alloys and Compounds 2011; **509**: 10003-10006.
- [23] C. Le Gall, A. Brunetti, H. Boukari, L. Besombes. Electron-nuclei spin dynamics in II-VI semiconductor quantum dots[J]. Phys. Rev. B 2012; **85**: 195312.
- [24] C. Testelin, B. Eble, F. Bernardot, G. Karczewski, M. Chamarro. Signature of the Overhauser field on the coherent spin dynamics of donor-bound electrons in a single CdTe quantum well[J]. Phys. Rev. B 2008; **77**: 235306.

- [25] P. Nahalkova, P. Nemec, D. Sprinzl, E. Belas, P. Horodysky, J. Franc, et al. Spin dynamics in bulk CdTe at room temperature[J]. Materials Science and Engineering B-Solid State Materials for Advanced Technology 2006; **126**: 143-147.
- [26] F. Meier, B. P. Zakharchenya. Optical orientation[B]. North-Holland; 1984.
- [27] G. Lampel. Nuclear Dynamic Polarization by Optical Electronic Saturation and Optical Pumping in Semiconductors[J]. Phys. Rev. Lett. 1968; **20**: 491-493.
- [28] D. Henriksen, T. Kim, I. Tifrea. Nuclear spin diffusion effects in optically pumped quantum wells[J]. Eur Phys J B 2014; **87**: 17.
- [29] S. E. Barrett, R. Tycko, L. N. Pfeiffer, K. W. West. DIRECTLY DETECTED NUCLEAR-MAGNETIC-RESONANCE OF OPTICALLY PUMPED GAAS QUANTUM-WELLS[J]. Phys. Rev. Lett. 1994; **72**: 1368-1371.
- [30] M. Eickhoff, B. Lenzman, G. Flinn, D. Suter. Coupling mechanisms for optically induced NMR in GaAs quantum wells[J]. Phys. Rev. B 2002; **65**: 125301.
- [31] V. K. Kalevich. Optically Induced Nmr in Semiconductors[J]. Fiz Tverd Tela+ 1986; **28**: 3462-3465.
- [32] J. M. Kikkawa, D. D. Awschalom. All-optical magnetic resonance in semiconductors[J]. Science 2000; **287**: 473-476.
- [33] G. Salis, D. T. Fuchs, J. M. Kikkawa, D. D. Awschalom, Y. Ohno, H. Ohno. Optical manipulation of nuclear spin by a two-dimensional electron gas[J]. Phys. Rev. Lett. 2001; **86**: 2677-2680.
- [34] R. Oulton, A. Greilich, S. Y. Verbin, R. V. Cherbunin, T. Auer, D. R. Yakovlev, et al. Subsecond spin relaxation times in quantum dots at zero applied magnetic field due to a strong electron-nuclear interaction[J]. Phys. Rev. Lett. 2007; **98**: 107401.
- [35] A. Greilich, S. E. Economou, S. Spatzek, D. R. Yakovlev, D. Reuter, A. D. Wieck, et al. Ultrafast optical rotations of electron spins in quantum dots[J]. Nature Physics 2009; **5**: 262-266.
- [36] I. P. Smorchkova, F. S. Flack, N. Samarth, J. M. Kikkawa, S. A. Crooker, D. D. Awschalom. Spin transport and optically-probed coherence in magnetic semiconductor heterostructures[J]. Physica B: Condensed Matter 1998; **249–251**: 676-684.

- [37] Y. Kato, R. C. Myers, D. C. Driscoll, A. C. Gossard, J. Levy, D. D. Awschalom. Gigahertz electron spin manipulation using voltage-controlled g-tensor modulation[J]. *Science* 2003; **299**: 1201-1204.
- [38] X. Z. Ruan, B. Q. Sun, Y. Ji, W. Yang, J. H. Zhao, Z. Y. Xu. Direct observation of coherent spin transfer processes in an InGaAs/GaAs quantum well via two-color time-resolved Kerr rotation measurements[J]. *Semicond. Sci. Technol.* 2008; **23**: 075021.
- [39] S. Cronenberger, P. Barate, A. Brunetti, M. Vladimirova, D. Scalbert, F. J. Teran, et al. Electron spin relaxation in very diluted CdMnTe quantum wells[J]. *Superlattices and Microstructures* 2008; **43**: 427-430.
- [40] A. Kanno, Y. Masumoto. Spin relaxation mechanism of strain-induced GaAs quantum dots studied by time-resolved Kerr rotation[J]. *Phys. Rev. B* 2006; **73**: 073309.
- [41] H. Sanada, Y. Kondo, S. Matsuzaka, K. Morita, C. Y. Hu, Y. Ohno, et al. Optical pump-probe measurements of local nuclear spin coherence in semiconductor quantum wells[J]. *Phys. Rev. Lett.* 2006; **96**: 067602.
- [42] H. Sanada, S. Matsuzaka, K. Morita, C. Hu, Y. Ohno, H. Ohno. Gate Control of Dynamic Nuclear Polarization in GaAs Quantum Wells[J]. *Phys. Rev. Lett.* 2005; **94**: 097601.
- [43] A. Uhrig, A. Worner, C. Klingshirn, L. Banyai, S. Gaponenko, I. Lacis, et al. Nonlinear Optical-Properties of Semiconductor Quantum Dots[J]. *Journal of Crystal Growth* 1992; **117**: 598-602.
- [44] N. H. Bonadeo, J. Erland, D. Gammon, D. Park, D. S. Katzer, D. G. Steel. Coherent optical control of the quantum state of a single quantum dot[J]. *Science* 1998; **282**: 1473-1476.
- [45] G. Bacher, R. Weigand, J. Seufert, N. A. Gippius, V. D. Kulakovskii, A. Forchel, et al. Dynamics of excitons and biexcitons in one single quantum dot[J]. *Physica Status Solidi B-Basic Research* 2000; **221**: 25-29.
- [46] I. A. Merkulov, A. L. Efros, M. Rosen. Electron spin relaxation by nuclei in semiconductor quantum dots[J]. *Phys. Rev. B* 2002; **65**: 205309.
- [47] D. H. Feng, I. A. Akimov, F. Henneberger. Nonequilibrium nuclear-electron spin dynamics in semiconductor quantum dots[J]. *Phys. Rev. Lett.* 2007; **99**: 036604.

- [48] I. A. Merkulov, G. Alvarez, D. R. Yakovlev, T. C. Schultheiss. Long-term dynamics of the electron-nuclear spin system of a semiconductor quantum dot[J]. Phys. Rev. B 2010; **81**: 115107.
- [49] D. Sanvitto, D. M. Whittaker, A. J. Shields, M. Y. Simmons, D. A. Ritchie, M. Pepper. Dynamic of spin triplet and singlet trions in a GaAs quantum well[J]. Physica Status Solidi a-Applied Research 2002; **190**: 809-812.
- [50] M. W. Wu, H. Metiu. Kinetics of spin coherence of electrons in an undoped semiconductor quantum well[J]. Phys. Rev. B 2000; **61**: 2945-2956.
- [51] M. W. Wu, J. H. Jiang, M. Q. Weng. Spin dynamics in semiconductors[J]. Physics Reports 2010; **493**: 61-236.
- [52] J. L. Cheng, M. Q. Weng, M. W. Wu. Manipulation of spin dephasing in InAs quantum wires[J]. Solid State Commun. 2003; **128**: 365-368.
- [53] B. Mihaila, S. A. Crooker, D. G. Rickel, K. B. Blagoev, P. B. Littlewood, D. L. Smith. Quantitative study of spin noise spectroscopy in a classical gas of K-41 atoms[J]. Physical Review A 2006; **74**: 043819.
- [54] H. Sigurdsson, T. C. H. Liew, O. Kyriienko, I. A. Shelykh. Vortices in spinor cold exciton condensates with spin-orbit interaction[J]. Phys. Rev. B 2014; **89**: 035302
- [55] M. A. Nielsen, I. L. Chuang. Quantum Computation and Quantum Information: 10th Anniversary Edition[B]. Cambridge University Press; 2010.
- [56] R. J. Warburton. Single spins in self-assembled quantum dots[J]. Nat Mater 2013; **12**: 483-493.

CHAPTER 2

FUNDAMENTALS OF SPIN IN OPTICAL SEMICONDUCTORS

In this chapter, just after a brief spintronics history at first, the fundamentals of optical interactions in a direct band gap semiconductor II-VI QW are presented to better understand the physical environment and optical processes excited by ultrafast pulses associated with excitons and electron spin coherence.

2.1 Spintronics Development

2.1.1 Brief Spin History

Before the spin angular moment concept was put forward, the degree of polarization of angular moment had been discovered by mercury vapor fluorescence as early as in 1923 [1]. In theory, George Uhlenbeck and Samuel Goudsmit first experimentally described the observation of doublets in spectroscopy for deducing a spin which is the intrinsic angular momentum of a particle in 1925. After that it is formalized by Wolfgang Pauli in 1926. Since then, the spin related researches began to take place, as well as the great events are shown in **Table 1-1** [2-6].

As can be seen from **Table 1-1**, the theoretical study of spin physics had been carried out for years. Till 1950's, the spin study started to draw more attention since the non-equilibrium distribution of atomic angular moments was manipulated by the luminescence polarization [1]. Later, the carrier spin polarization degree can be surveyed directly by the circular polarization of the recombination luminescence in semiconductors.

The spin of lattice nuclei was firstly measured for a number of intriguing effects in GaAs [7]. Subsequently, the first experimental demonstration of optical spin orientation of electrons was done by Lampel in 1968 in Si by a circularly polarized light [8]. Until 1988, the groups of Albert Fert and Peter Grünberg observed a giant change in the electrical resistance of thin metal layers as a function of an external magnetic field [9], for which they won two Nobel Prizes in Physics in 2007. This giant magnetoresistance (GMR) is just caused by the spin scattering of electrons travelling across the metallic thin films [9]. The breakthrough of experimental spin science has brought semiconductors towards the later actual spintronic applications stated below.

Table 1-1: Important Development History of Spin [2-6]

Time	Spin Development Event
1925	Theoretical definition of spin
1928	Dirac equation and Quantum magnetism
1932	Isospin
1940	Spin-statistics connection
1946	Nuclear magnetic resonance
1950	NMR for chemical analysis
1950s	Development of magnetic devices
1951	Einstein–Podolsky–Rosen argument in spin variables
1963	The spin of lattice nuclei [7]
1964	Kondo effect
1968	The spin of electrons [8]
1971	Super symmetry
1972	Superfluid helium-3
1973	Magnetic resonance imaging
1975	NMR for protein structure determination
1978	Dilute magnetic semiconductors
1988	Giant magneto-resistance [9]
1990	Functional MRI & Proposal for spin field-effect transistor

1991	Magnetic resonance force microscopy
1996	Mesoscopic tunnelling of magnetization
1997	Semiconductor spintronics [10]
2012	Persistent spin helices for more than 1ns

2.1.2 Spintronics

Most of the electronic devices in our everyday life, as the semiconductor electronic structure, are using electrical field to control charge transport. However, the energy needed to generate and transport electron spins is much less than that necessary to create charge electron currents. In addition, the electron spin polarization has a lot of possibilities which can be applied to store the quantum coherence [11] and be used as qubits for quantum information processing [12], as high-speed all-optical switches and light modulators in spin-based technologies [13]. On the account of the greater advantages of electron spin polarization as discussed above, integrating the control of the spin degree of freedom of electrons into current technology leads to the emergent of spintronics devices. Although the term spintronics was not proposed until 1996 in the proposal to the U.S. Department of Defense Advanced Research Projects Agency to apply magnetic materials and devices of the study by Wolf [14], the electron spin study in the electronic devices had already started before. Especially after discovering the coherence time for spin states of up to 1 ns in a II–VI compound [6]— proving that the spin state could live for a long enough time, the spintronics became an extreme research hotspot, since it can reach an essential requirement for any spintronic device [10, 15-17]. In 2012, IBM scientists revealed persistent spin helices of synchronized electrons persisting for more than a nanosecond in a GaAs/AlGaAs QW. This is a 30 times increase from the previously observed results and longer than the modern processor clock

cycle, which indicates that electron spins available for information processing [18]. In a word, spintronics has recently aroused great interest in the scientific community due to its promising future for creating circuits faster and more efficient than that existing in the current semiconductor devices. In practice, the main obstacle that spintronics face is to produce polarized spin currents without any loss of polarization during the process [4]. Especially, the resident electron spins polarization (RESP) has a long coherence time even in a QW [19]. In addition, highly sensitive techniques of ensemble electron spin manipulation and deep understanding of spin coherence play significant roles in the initiation of spintronics.

2.2 Band Structures in Zinc-blende Semiconductors

We should know the electronic structure and wave functions for various bands to understand the optical properties in semiconductor QWs. For our sample material of CdTe, which is a direct band gap semiconductor, as shown in **Figure 2-1**, where the blue line indicates the conduction band of CdTe, the red curves are the heavy- and light-hole valence bands [20].

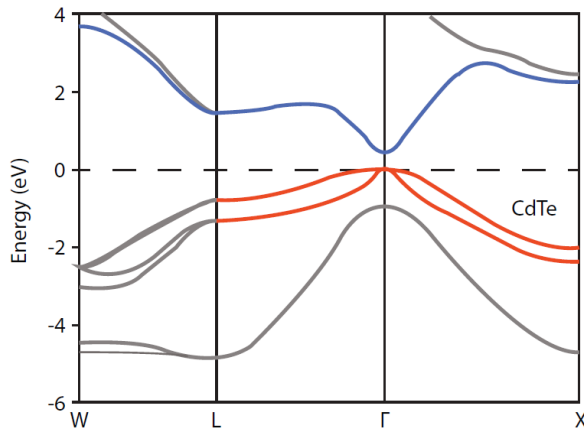


Figure 2-1: The band structure for CdTe: Direct band gap transitions occur at the Γ -

point [20].

Here, the electronic states are expected to be near the center of the Brillouin zone where $k = 0$. What is more, the bottom of the conduction band and the top of the valence band form a direct band-gap in CdTe [20]. An extremely useful method for modeling the band structure is the **K•P** method as presented below.

2.2.1 Bloch's Theorem

Based on quantum mechanics, an electron in any state has a wave function which can be described by the following Schrödinger equation, which neglects the spin-orbit effect [21]:

$$H\Psi(\vec{r})=(\frac{\vec{p}^2}{2m_0}+V(\vec{r}))\Psi(\vec{r})=E(\vec{k})\Psi(\vec{r}) \quad \text{Eq. 2-1}$$

Where, H is one-electron Hamiltonian operator; $\Psi(\vec{r})$ describes the one-electron Bloch wave function; p is the quantum-mechanical momentum operator, that is $P=-i\frac{\hbar}{m_0}\langle c|P_z|v\rangle$, which is the Kane's parameter, the momentum matrix element between the conduction band and the valence band. Additionally, in this equation, $\hbar = 6.58211928\times10^{-16}$ eV·s is a reduced Planck constant [22]. m_0 is the mass of an electron; E is the eigen-energy. In a crystalline solid, V is a periodic function: $V(\vec{r})=V(\vec{r}+\vec{R})$, which is a periodic potential and is invariant under crystal transmission, where, R is an integer distance between lattice sites inside the crystal.

Due to the periodicity of the lattice potential by applying the Bloch theorem, the general solution for the differential equation of the Hamiltonian in **Eq. 2-1** can be written by the Bloch wave function in the form of [23]:

$$\Psi_{n,\vec{k}}(\vec{r}) = e^{i\vec{k} \cdot \vec{r}} u_{n,\vec{k}}(\vec{r}) \quad \text{Eq. 2-2}$$

Where, variable k is the wave-vector, equaling the physical quantity of momentum, if it is multiplied by the reduced Planck's constant; n is the band index; $u_{n,\vec{k}}$ is a periodic Bloch lattice function $u_{n,\vec{k}}(\vec{r}) = u_{n,\vec{k}}(\vec{r} + \vec{R})$ with the same translational symmetry and periodicity as the crystal lattice. The associated state for any given n is a band, in which there will be a relationship, labeled as the band dispersion, between the wave-vector and the state energy. In the semiconductors, the dispersion is nothing but the free electron dispersion, which also can be calculated by the $\mathbf{K} \cdot \mathbf{P}$ perturbation theory, as we all know.

2.2.2 $\mathbf{K} \cdot \mathbf{P}$ Perturbation without Spin-orbit Interaction

Substituting the Bloch wave function **Eq. 2-1** into Schrodinger equation **Eq. 2-2**, we can arrive at another equation, similar to the Schrodinger equation, in which the $\mathbf{K} \cdot \mathbf{P}$ method begins with two extra terms [23], namely:

$$H * u_{n,\vec{k}}(\vec{r}) = \left(\frac{\vec{p}^2}{2m_0} + V(\vec{r}) + \frac{\hbar}{m_0} \vec{k} \cdot \vec{p} + \frac{\hbar^2 \vec{k}^2}{2m_0} \right) * u_{n,\vec{k}}(\vec{r}) = E(\vec{k}) * u_{n,\vec{k}}(\vec{r}) \quad \text{Eq. 2-3}$$

In which, the unperturbed Hamiltonian is the part $H_0 = \frac{\vec{p}^2}{2m_0} + V(\vec{r})$, which in fact equals

to the exact Hamiltonian at $k = 0$, the Γ point. The perturbation is the term

$H_k = \frac{\hbar}{m_0} \vec{k} \cdot \vec{p} + \frac{\hbar^2 \vec{k}^2}{2m_0}$. Note that the perturbation term H_k gets progressively small, as k

approaches to zero [23].

To describe the bands, the numerical solutions of **Eq. 2-3** are required to calculate the general energy band along the different k directions. We focused on the dynamics during the k small values of near zero, the Γ point, shown in **Figure 2-2**. Then we can

know that the three valence bands are degenerate at $k = 0$ in the absence of spin-orbit interaction.

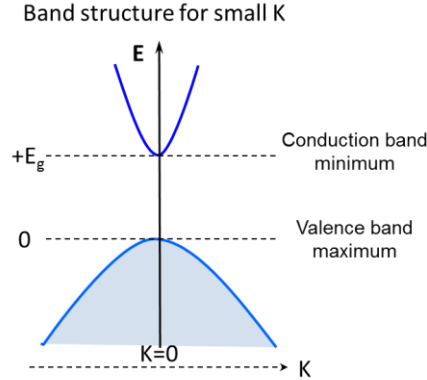


Figure 2-2: $\mathbf{K}\cdot\mathbf{P}$ band structures without spin-orbit coupling.

Supposing Bloch wave equations and energies for bands are known at $k = 0$, we can treat the terms $\frac{\hbar}{m_0} \vec{k} \cdot \vec{p}$ and $\frac{\hbar^2 \vec{k}^2}{2m_0}$ as perturbations in either degenerate or non-degenerate perturbation theory to calculate the wave equations and energies near $k = 0$ [24].

2.2.3 $\mathbf{K}\cdot\mathbf{P}$ Model with Spin-orbit Interaction

For describing the energy bands of a direct band gap semiconductor fully, it is necessary to interpret the effects of spin-orbit coupling, which is a result of torque acted on the spin of the electron by a magnetic field of the positively charged nuclei [1]. This method for calculating bands of merging the spin-orbit interaction Hamiltonian into the $\mathbf{K}\cdot\mathbf{P}$ method is shown by the following Hamiltonian:

$$H = \frac{\vec{p}^2}{2m_0} + \frac{\hbar}{m_0} \vec{k} \cdot \vec{p} + V(\vec{r}) + \frac{\hbar^2 k^2}{2m_0} + \frac{\vec{\sigma} \times \nabla V}{4m^2 c^2} \cdot (\hbar \vec{k} + \vec{P}) \quad \text{Eq. 2-4}$$

Where, $\vec{\sigma} = (\sigma_x, \sigma_y, \sigma_z)$ is Pauli-spin matrices, to the Schrödinger equation in **Eq. 2-3**.

Additionally, the perturbation is considered by the interaction Hamiltonian:

$$H_{\text{int}} = \frac{\hbar}{m_0} \vec{k} \cdot \vec{p} + \frac{\vec{\sigma} \times \nabla V}{4m^2 c^2} \cdot (\hbar k + \vec{P}) \quad \text{Eq. 2-5}$$

The wave functions are based on the atomic s-like and p-like wave functions. Besides orbital angular momentum, the spin angular momentum in the conduction and valence bands must also be taken into account. The calculations of band dispersion near the Γ point can be performed in a fairly simple manner using the **K•P** method [25]. Finally, by utilizing symmetry properties of the conduction band near $k = 0$, the energy dispersion bands including the conduction band in **Eq. 2-6**, heavy-hole band in **Eq. 2-7**, light-hole band in **Eq. 2-8**, an energy offset- Δ , for the split-off band in **Eq. 2-9** resulting from spin-orbit coupling term are calculated as shown below:

$$E_c(\vec{k}) = E_g + \frac{\hbar^2 \vec{k}^2}{2m_e^*} \quad \text{Eq. 2-6}$$

$$E_{hh}(\vec{k}) = -\frac{\hbar^2 \vec{k}^2}{2m_{hh}^*} \quad \text{Eq. 2-7}$$

$$E_{lh}(\vec{k}) = \frac{\hbar^2 \vec{k}^2}{2m_0} - \frac{2P^2 \vec{k}^2}{3E_g} = -\frac{\hbar^2 \vec{k}^2}{2m_{lh}^*} \quad \text{Eq. 2-8}$$

$$E_{so}(\vec{k}) = -\Delta + \frac{\hbar^2 \vec{k}^2}{2m_0} - \frac{2P^2 \vec{k}^2}{3(E_g + \Delta)} = -\Delta - \frac{\hbar^2 \vec{k}^2}{2m_{so}^*} \quad \text{Eq. 2-9}$$

Where, m_e^* is the effective mass of the electron; E_g is the energy band gap; P is Kane's parameter; Δ is the split-off energy. Each of the band gap and the split off energy is a parabolic function with curvature defined by an effective mass.

Using the expressions above for the energy dispersion relation, a simplified expression for the effective mass in the conduction band of a semiconductor can be found

[26]. The effective mass is given by $m_e^* \approx E_g \frac{m_0^2}{2P^2}$. The effective mass of an electron in the conduction band of CdTe is $m_c^* = 0.1m_0$, where $m_0 = 9.10938291 \times 10^{-31}$ kg, the mass of an electron. The heavy hole and light hole effective masses are $m_{hh}^* = 0.45m_0$ and $m_{lh}^* = 0.1 m_0$, respectively [27]. Besides, the $E_g = 1.575$ eV is used here.

From the above model, we could be able to obtain the eigen-functions for the conduction band and valence bands, as well as the corresponding energy shift for the split-off band, shown as $-\Delta$ in **Figure 2-3**. The solution based on these four bands does not give the correct curvature for the heavy-hole valence band. However, the incorporation of higher bands corrects this [28]. A diagram for the typical bandstructure dispersion curves of CdTe semiconductors is shown in **Figure 2-3**.

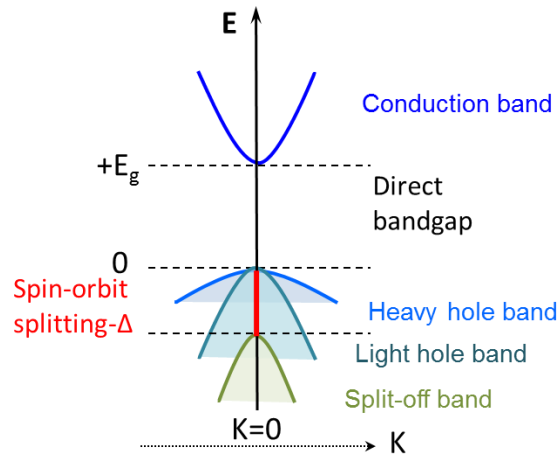


Figure 2-3: Energy dispersion curves near $k = 0$ for the conduction, heavy-hole, light-hole, and split-off bands.

For this zinc-blende semiconductor, at $k = 0$, the conduction band state is s-like, moreover the valence band states are linear combinations of the three p-like orbitals, as we know. From the energy corrections, for the new eigen-functions in the different bands, their total angular momentum and z-projection are shown here: Conduction band-

$$\left| \frac{1}{2}, -\frac{1}{2} \right\rangle, \left| \frac{1}{2}, \frac{1}{2} \right\rangle; \text{ Heavy-hole band-} \left| \frac{3}{2}, -\frac{3}{2} \right\rangle, \left| \frac{3}{2}, \frac{3}{2} \right\rangle; \text{ Light-hole band-} \left| \frac{3}{2}, -\frac{1}{2} \right\rangle, \left| \frac{3}{2}, \frac{1}{2} \right\rangle;$$

And split-off band- $\left| \frac{1}{2}, -\frac{1}{2} \right\rangle, \left| \frac{1}{2}, \frac{1}{2} \right\rangle$ [29].

For the optical quantum properties studies, the most obvious difference between bulk and QW is the enhanced band-gap energy in QWs. Because the non-zero energy of the QW ground state shifts the lowest electron and hole subbands further from each other in energy levels, thus, there is an increase in the separation of the conduction and valence bands [29]. In addition, this simple classification of holes into "heavy" and "light" is only valid near the center of the Brillouin zone. The detailed structure of the valence bands for a larger range is particularly complicated, since the various subbands would actually appear to cross one another. Hence we would not discuss such valence band effects further here. The detailed relative content in our QW sample will be described in next chapter.

2.3 Density of State

In a semiconductor structure, the density of states (DOS: number of states per unit area per unit energy) is directly related to the movable degrees of freedom of the carriers. Carriers can move freely inside the sufficiently large three dimensions semiconductor,

along with this, the wave functions are typically extended throughout the crystal. The description given in Section 2.3 is according to that presented in Ref. [30-32].

2.3.1 3D Density of State

In other words, the density of states, denoted by $g(E)$, indicates how densely packed quantum states in a particular system. So, what is the importance of the density of states? Consider the expression $g(E)dE$ which represents the number of states between E and dE , integrating the density of the quantum states over a range of energy will produce a number of states:

$$N(E) = \int_E^{\Delta E} g(E)dE \quad \text{Eq. 2-10}$$

The number of quantum states is important in the determination of a material's optical properties, such as semiconductor QDs, QWs, as well as carbon nanotubes.

From the Schrodinger equation mentioned above, we know that the energy of a particle is quantized and is given by $E = k^2\hbar^2/2m$. Moreover, a particle's energy is $E = mv^2/2 = m^2v^2/2m = p^2/2m$. Relating these two equations yields $k = p/\hbar$.

The momentum is a vector which has components in the x, y, and z directions. Therefore, k must also have direction components k_x , k_y , and k_z . Since energy is not a vector, the more accurate expression for energy is:

$$E = \frac{|k|^2 \hbar^2}{2m} \quad \text{Eq. 2-11}$$

In a 3D system, then, the total energy is given by

$$E = \frac{\hbar^2}{2m} (k_x^2 + k_y^2 + k_z^2) \quad \text{Eq. 2-12}$$

In three dimensions, each directional component of k would be

$$k_x = \frac{n_x \pi}{a}, k_y = \frac{n_y \pi}{a}, \text{ and } k_z = \frac{n_z \pi}{a} \quad \text{Eq. 2-13}$$

where, a is the length of the volume along all three sides. The wave function is valid at regular intervals of π/a .

To find the density of these states, we need to first examine the unit cell and its volume. The unit cell V_{single} is the smallest K-space volume shape of single state and is required to hold a single electron, which can be repeatedly used to construct a lattice, for example in a diamond crystal. Examining the image above and knowing that the quantum states are separated by an interval of π/a , the unit cell, that is the K-space volume of single state cube in K-space, would be the volume $V_{\text{single}} = (\pi/a)^3$.

The density of states problem is a problem of finding the number of states in the interval of E and $E+dE$. In k-space, the interval is simply between k and $k+dk$. Because we are operating three dimensions and a sphere in k-space is considered with the k-space volume of $V_k = 4\pi k^3/3$, k represents the radius of a sphere in k-space and dk is the thickness of the sphere. Hence, a shell is created which encloses a certain amount of quantum states in an infinitesimal interval. We use the sphere because k is directly related to E , as well as all the points on the sphere have an equal energy. Since we want to find the density of states in an infinitesimal interval of energy, the shape used for the boundaries of the interval must represent equal energies.

We can find the volume by subtracting the volume inside the inner sphere from the volume inside the outer sphere (of radius $k + dk$). The result leaves a shell.

$$\begin{aligned}
V_{shell} &= \frac{4}{3}\pi(k + dk)^3 - \frac{4}{3}\pi(k)^3 \\
&= \frac{4}{3}\pi(k^3 + 3k^2dk + 3kdk^2 + dk^3 - k^3)
\end{aligned} \tag{Eq. 2-14}$$

Since dk^2 and dk^3 are much smaller values and have no real meanings, keeping terms only up to the order dk to yield:

$$V_{shell} = \frac{4}{3}\pi(3k^2dk) = 4\pi k^2 dk \tag{Eq. 2-15}$$

In the same way, the volume of the shell $V = 4\pi k^2 dk$ is essentially the surface area of the inner sphere (of radius k) multiplied by the thickness of the sphere (dk).

Even though the k-space image displays valid wave equations solutions for both positive and negative integers of k_x , k_y , and k_z , the wave function should only be valid for all positive values of k_x , k_y , and k_z . Therefore, the entire shell's volume is unnecessary; we really only need to consider an eighth of the entire volume (i.e. the upper right hand quadrant which satisfies $x > 0$, $y > 0$, and $z > 0$ collectively). The revised shell volume is then:

$$V_{shell} = \left(\frac{1}{8}\right)4\pi k^2 dk = \frac{1}{2}\pi k^2 dk \tag{Eq. 2-16}$$

The number of quantum states in an interval of dk is found by dividing the volume of the shell by the volume of a single state (i.e. the volume of the unit cell).

$$g(k)dk = \frac{V_{shell}}{V_{single}} = (2)\frac{\frac{1}{2}\pi k^2 dk}{\left(\frac{\pi}{a}\right)^3} = \frac{a^3}{\pi^2} k^2 dk \tag{Eq. 2-17}$$

Since we know the relation between k and E , we can find what we are searching: the density of states as a function of energy. Once again, by the relationship $k = \sqrt{2mE/\hbar^2}$ between k and E , we can get this:

$$dk = \frac{1}{2} \left(\frac{2m}{\hbar^2} \right) \left(\frac{2mE}{\hbar^2} \right)^{-\frac{1}{2}} dE$$

$$= \frac{m}{\hbar^2} \left(\frac{2mE}{\hbar^2} \right)^{-\frac{1}{2}} dE$$
Eq. 2-18

Substituting the results into the density of states equation will give the density of states in terms of energy:

$$g(E)dE = \frac{a^3}{\pi^2} k^2 dk = \frac{a^3}{\pi^2} * \left(\frac{2mE}{\hbar^2} \right) * \frac{m}{\hbar^2} \left(\frac{2mE}{\hbar^2} \right)^{-\frac{1}{2}} dE$$

$$= \frac{a^3}{\pi^2} \frac{2 \left(2^{-\frac{1}{2}} \right) m^2 \left(m^{-\frac{1}{2}} \right) E \left(E^{-\frac{1}{2}} \right)}{\hbar^4 \hbar^{-1}} dE$$

$$= \frac{a^3}{2\pi^2} \frac{2^2 \left(2^{-\frac{1}{2}} \right) m^{\frac{3}{2}}}{\hbar^3} \sqrt{E} dE$$

$$= \frac{a^3}{2\pi^2} \frac{(2m)^{\frac{3}{2}}}{\hbar^3} \sqrt{E} dE$$
Eq. 2-19

2.3.2 2D Density of State

Within the envelope function formalism, which was briefly discussed in Section 1.2.2, the wavefunction of such a QW is now typically separated into plane-wave states in the plane of the QW and an envelope function in the perpendicular direction.

In 2D, an electron is confined along one dimension but able to travel freely in the other two directions. In the image below, an electron would be confined in the z-direction but would travel freely in the XY plane:

$$\psi(x) = A \cos(kx) + B \sin(kx)$$
Eq. 2-20

Where $k = n\pi/a$. Additionally, a is the width of the barrier. For the cosine term in the wave function, n must be an odd integer, Furthermore, for the sine term, n must be an even integer. Therefore, the wave function is only valid for all integers greater than zero.

In the 3D density of states analysis, a spherical volume of width dk had to be used. However, in 2D, the problem of calculating becomes easier, because we only need to operate in two dimensions. Instead of using the volume of a shell, the area of a ring with width of dk is used. Analogous to the sphere in three dimensions, the circle is used because all points on the circle are an equal distance from the origin; therefore, the circle indicates equal values of energy. The radius becomes $k = \sqrt{k_x^2 + k_y^2}$. In the 2D case, the unit cell is simply a square with side length of π/a .

Following the same procedure which was used in the 3D situation, the area of the unit cell is $A_{cell} = (\pi/a)^2$. Next, we need to find the area of the ring and then divide by the area of the unit cell. The area of a circle is πr^2 where r is the radius. The area of the ring, then, is

$$A_{ring} = \pi(k + dk)^2 - \pi k^2 = 2\pi k dk \quad \text{Eq. 2-21}$$

However, only positive values of k should be considered. Therefore, we only need one-fourth of the entire area of the ring. The revised area is

$$A_{ring} = \frac{1}{4} 2\pi k dk = \frac{\pi}{2} k dk \quad \text{Eq. 2-22}$$

Dividing the ring area by the unit cell area, the density of states can be found.

$$g(k)dk = 2 \left(\frac{A_{ring}}{A_{cell}} \right) = (2) \frac{\frac{\pi}{2} k dk}{\left(\frac{\pi}{a} \right)^2} = \frac{a^2}{\pi} k dk$$
Eq. 2-23

Since we know the relation between k and E , we can find what we are searching: the density of states as a function of energy once again:

$$dk = \frac{1}{2} \left(\frac{2m}{\hbar^2} \right) \left(\frac{2mE}{\hbar^2} \right)^{-\frac{1}{2}} dE = \frac{m}{\hbar^2} \left(\frac{2mE}{\hbar^2} \right)^{-\frac{1}{2}} dE$$
Eq. 2-24

Substituting the results into the density of states equation will give the density of states in terms of energy:

$$g(E)dE = \frac{a^2}{\pi} \left(\frac{2mE}{\hbar^2} \right)^{\frac{1}{2}} \left[\frac{m}{\hbar^2} \left(\frac{2mE}{\hbar^2} \right)^{-\frac{1}{2}} \right] dE = \frac{a^2 m}{\pi \hbar^2} dE$$
Eq. 2-25

As a result, the DOS shows the \sqrt{E} behavior for 3D bulk and step-like (no E dependence) for 2D QW as shown in **Figure 2-4**.

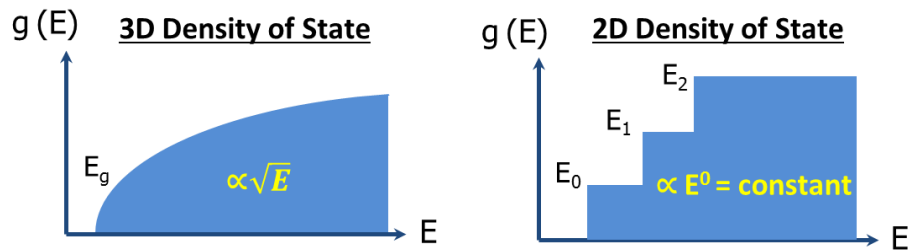


Figure 2-4: DOSs of 3D and 2D semiconductors.

Synthesize the content in Section 2.2 and Section 2.3, some of these features are illustrated synthetically in **Figure 2-5** [33], depicting the electrons in an idealized single QW with parabolic bands [33]. Note that the density of states n is step-like (bold line)

and thus quasi-two-dimensional. It just follows the contour of the density of states (normal line) and comes out the three wave functions.

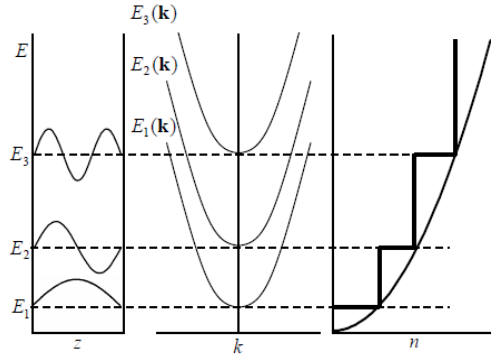


Figure 2-5: A schematic diagram illustrating the envelope functions, subbands and density of states of a typical square QW.

2.4 Spin Injection

As we all know, there are the equivalent of spin-up and spin down carriers independently as it is in equilibrium initially in a non-magnetic semiconductor sample. Over the last decade, there have been numerous demonstrations of spin injection into semiconductors, in particular, GaAs based spin-light-emitting diode devices. Spin injection can be achieved by the electrical injection through a ferromagnetic contact and the spin orientation through the circular polarization light in a QW. We know that the imaged transport and precession of spins injected into bulk n-GaAs had been successfully performed through an Fe contact by using the optical Kerr effect early in 2005 [34].

2.4.1 Electrical Generation

According to the electrical spin injection, the first way is that the sample should be connected to a magnetic electrode through a spin-dependent tunnel barrier between a ferromagnetic metal and a semiconductor. Then a net spin polarization can be

accumulated at the sample, while the current drives spin-polarized electrons from an electrode to the sample [35]. The voltage mainly happens to drop at the interface as the barrier impedance at the interface is enough high in the tunneling process. Then the current through the barrier is sufficiently small so that the two electrodes remain in equilibrium without the strong influence of the spin-dependent transport across the interface from the spin depended relative conductivities of the electrodes [14]. In this way, the higher and higher efficient electrical spin injection has been realized from metal to semiconductor in different kinds of materials [36, 37].

In addition to the application of tunnel barriers, the ferromagnetic semiconductor could also realize the spin injection in the ferromagnetic metal and semiconductor system [15]. Half-metallic ferromagnet, as the most efficient spin injector, has the pretty ideal spin polarization actually. However, their Curie temperatures are much lower than room temperature and the highest one is below ~ 170 K. Therefore, for spintronic device, the ferromagnetic semiconductors are not so practical.

2.4.2 Optical Initialization

In another method, optical pumping could initialize a higher non-equilibrium spin polarization by the way that the angular momentum of circularly polarized light is transferred to the spin orbital angular momentum of the carriers. Then the spin-orbit coupling polarizes the electron spins [38]. The detailed optical pumping method will be introduced here.

In this part, the wave functions are considered for the various bands for understanding the way electrons are excited from the valence band to the conduction band. The inter band optical excitations governed by the dipole matrix elements [39] as

$\mu_{vc} = e \langle v | \vec{r} | c \rangle$, where v represents the various valence band states, c is the conduction band state, e is the electron, r is the position operator.

The transitions only occur between states for which the spatial variation of the wave function is similar and near the Fermi energy; this leads to the selection rule $\Delta n = 0$ for the absorption. **Figure 2-6** displays the allowed optically interband transitions for circularly polarized light propagating in the growth axis of a SQW [40]. The incident σ^- polarized photon creates an exciton in the state $| -1 \rangle = | S_{z,e}: +1/2, J_{z,hh}: -3/2 \rangle$, and vice versa for σ^+ polarized light absorption. Here, $S_{z,e}$ and $J_{z,hh}$ designate the projections of the electron spin and hh angular momentum onto the z axis. The states labeled as $| J, J_z \rangle$ which presents the total angular momentum J , z-component of the spin angular momentum. The electron states in the conduction band are written as $| 1/2, \pm 1/2 \rangle$. The heavy-hole states are written as $| 3/2, \pm 3/2 \rangle$. Moreover, the light-hole states are written as: $| 3/2, \pm 1/2 \rangle$.

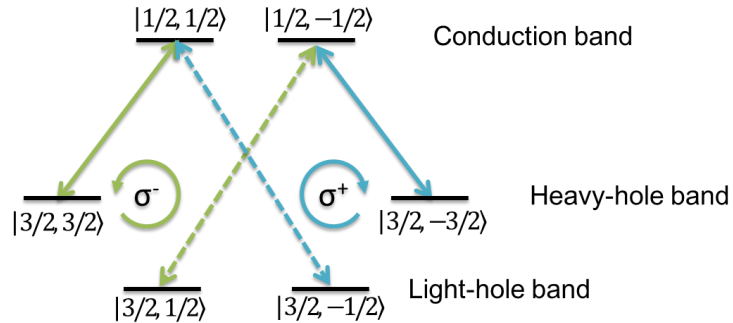


Figure 2-6: Optical selection rules for dipole coupling states in the valence and the conduction band for CdTe. The states labeled by $| J, J_z \rangle$ represents their total angular momentum and z-component of spin angular momentum. The coupling transitions with σ^+ and σ^- circular polarized lights are indicated by green and blue arrows, solid for e-hh and dotted for e-lh.

What is more, this method can be used in the Kerr or Faraday rotation spectroscopy to probe the spin dynamics selectively. In bulk semiconductors, the HH states ($S_z = \pm 3/2d$) are degenerate strongly with the LH states ($S_z = \pm 1/2$), whereas the light and heavy hole sub-bands are further split (Δc) by the quantum confinement and/or strain caused by mismatch of the QW and barrier lattice constants in a nanostructure, such as a QW or QD. Confinement effects lift the degeneracy [41]. The light hole sub-bands are spaced further apart due to their lighter mass. Consequently, there are actually two sets of steps for optical absorption. The heavy-hole-to-conduction set starts at a slightly lower energy and is more closely spaced than the light-hole-to-conduction set.

Anyway, the spin polarization can be generated by injecting the spin polarized current inside either electrically or optically in general currently.

2.5 Spins in the Bloch Sphere

The spin vector in two-level systems would be referred to many times for the time evolution operator later in this work. For the time evolution, Bloch ball is an excellent method of visualizing the electron spin vector [39, 42, 43].

In the case of the angular momentum, a lone electron is just a spin-1/2 particle. A general spin state for spin 1/2 electrons can be described using the following quantum-mechanical wave-function: $|\Psi\rangle = \alpha|\uparrow\rangle + \beta|\downarrow\rangle$, where $|\uparrow\rangle$ and $|\downarrow\rangle$ correspond to the up and down states of the spin. Furthermore, α and β are complex coefficients with $\alpha^2 + \beta^2 = 1$.

By the way, using the density matrix, the density matrix is given like this [44]:

$$\rho = \begin{pmatrix} \rho_{\uparrow\uparrow} & \rho_{\uparrow\downarrow} \\ \rho_{\downarrow\uparrow} & \rho_{\downarrow\downarrow} \end{pmatrix}, \text{ with } \rho_{\uparrow\downarrow}^* = \rho_{\downarrow\uparrow} \text{ in the z-basis. The density matrix elements should be}$$

referred to the special orientation of spin by determining the ensemble averages of the spin operators in each direction. Additionally, in the z-basis of states, it is convenient to write down the matrix forms of the operators as shown here:

$$\mathcal{S}_x = \frac{\hbar}{2} \begin{pmatrix} 0 & 1 \\ 1 & 0 \end{pmatrix}; \quad \mathcal{S}_y = \frac{\hbar}{2} \begin{pmatrix} 0 & -i \\ i & 0 \end{pmatrix}; \quad \mathcal{S}_z = \frac{\hbar}{2} \begin{pmatrix} 1 & 0 \\ 0 & -1 \end{pmatrix} \quad \text{Eq. 2-26}$$

the vector $\vec{\mathcal{S}} = (\mathcal{S}_x \ \mathcal{S}_y \ \mathcal{S}_z)$ is the spin operator for the electron spin 1/2. The ensemble average of an operator S is given by $[S] = \text{Tr}(\rho S)$, where Tr is the trace of a matrix. We acquired the following relationship by computing the ensemble averages of the spin operators:

$$\begin{aligned} [\mathcal{S}_x] &= \frac{\hbar}{2} (\rho_{\uparrow\downarrow} + \rho_{\downarrow\uparrow}) = \hbar \text{Re}(\rho_{\uparrow\downarrow}) \\ [\mathcal{S}_y] &= \frac{i\hbar}{2} (\rho_{\uparrow\downarrow} - \rho_{\downarrow\uparrow}) = -\hbar \text{Im}(\rho_{\uparrow\downarrow}) \\ [\mathcal{S}_z] &= \frac{\hbar}{2} (\rho_{\uparrow\uparrow} - \rho_{\downarrow\downarrow}) \end{aligned} \quad \text{Eq. 2-27}$$

The Bloch sphere represents the ensemble average of the spin in each dimension. Additionally, the normalized magnitude of the Bloch vector is unity, which is just the normalized unity of the density matrix in the following:

$$\begin{aligned} \langle x \rangle &= [\mathcal{S}_x] \frac{2}{\hbar} = 2 \text{Re}(\rho_{\uparrow\downarrow}) \\ \langle y \rangle &= [\mathcal{S}_y] \frac{2}{\hbar} = 2 \text{Im}(\rho_{\uparrow\downarrow}) \\ \langle z \rangle &= [\mathcal{S}_z] \frac{2}{\hbar} = \rho_{\uparrow\uparrow} - \rho_{\downarrow\downarrow} \end{aligned} \quad \text{Eq. 2-28}$$

Using the notion of the optical Bloch equations, the density matrix elements can be found as a function of time and related to the direction of the spin polarization. In our experiments, described in the next chapter, a magnetic field along the x -axis causes the electron spins to precess about the field. We then measure the z -projection of the electron

spin polarization. Visualizing these dynamics using the Bloch sphere is helpful, since we can imagine the Bloch vector precessing about the x -axis, as well as relate the z -axis projection of the Bloch vector to the measured signal.

Here, the spin state is represented as a vector (S_x, S_y, S_z) , where $(0, 0, \pm S_z)$ represents the eigenstates \uparrow and \downarrow . Furthermore, vectors with nonzero S_x and S_y represent coherent superposition of \uparrow and \downarrow .

Note that there are four degrees of freedom in the two complex coefficients α and β in **Eq. 2-11**. However, the normalization requirement removes one of these degrees of freedom, as well as another can be ignored as an overall phase. Thus there are only two degrees of freedom that we care about. So **Eq. 2-11** can be rewritten as:

$$|\Psi\rangle = \alpha|\uparrow\rangle + e^{i\phi}\sqrt{1-\alpha^2}|\downarrow\rangle = \cos\frac{\theta}{2}|\uparrow\rangle + e^{i\phi}\sin\frac{\theta}{2}|\downarrow\rangle. \quad \text{Eq. 2-29}$$

Note that all possible values in this equation can be mapped to the surface of the unit sphere (**Figure 2-7**), where θ and ϕ can be thought of as the polar and azimuthal angles defining a point on the Bloch sphere, respectively. In this geometrical model of a spin-1/2 particle, as the Bloch sphere, the poles of the sphere correspond to the two spin eigenstates $|\uparrow\rangle$ and $|\downarrow\rangle$. Points elsewhere on the surface of the sphere correspond to quantum coherent super-positions of these two eigenstates. $|\Psi\rangle$ can only exist at one point on the surface of the Bloch sphere at any given point in time, which we indicate in **Figure 2-7** with a blue arrow that originates at the center of the sphere [23].

In the Bloch sphere model, to “polarize” a spin means to purposefully set $|\Psi\rangle$ at one of the pole positions corresponding to $|\uparrow\rangle$ or $|\downarrow\rangle$. Once a spin has been polarized, it can often then be “rotated” to another point on the surface of the sphere through direct

and precise manipulation of the spin. The “coherence time” of a spin corresponds to the length of time that $|\psi\rangle$ will remain at one point on the sphere before being perturbed by its surrounding environment. Since the state can be mapped onto the surface of the sphere. So the projection of the polar angle on the z -axis gives the fraction of the wave function in the ground or excited state. Furthermore, the azimuthal angle corresponds to the relative phase difference between those two parts of the wave function.

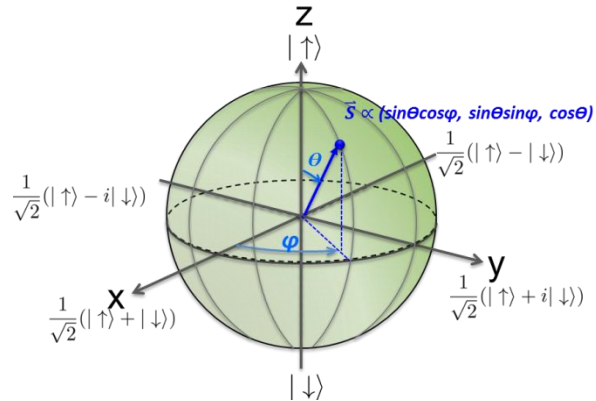


Figure 2-7: Bloch sphere. The “up” and “down” eigen-states are just the vectors pointing to the north and south poles of the Bloch sphere. Moreover, all rest other points on the sphere represent the quantum-coherent super positions of these two eigen-states [45, 46].

Mixed state appears inside the ball rather than spherical surface, i.e. its distance from the center of the ball is less than one. The center of sphere represents the most maximally mixed state.

The usefulness of this bloch ball can be seen by looking at the expectation values of the spin in the x , y , and z directions to predict the outcome of a measurement on this spin. For instance, if we were to make a classical measurement of the spin along the z -axis, the observed value would be the corresponding expectation value of S_z using the matrix forms of the spin operators given above:

$$\langle \hat{S}_z \rangle = \langle \Psi | S_z | \Psi \rangle = \frac{\hbar}{2} \cos \theta \quad \text{Eq. 2-30}$$

For the x -axis and y -axis, the observed values would be:

$$\langle \hat{S}_x \rangle = \frac{\hbar}{2} \cos \phi \sin \theta; \quad \langle \hat{S}_y \rangle = \frac{\hbar}{2} \sin \phi \sin \theta \quad \text{Eq. 2-31}$$

These expectation values are equivalent to the x , y , and z components of the Bloch vector, as shown in **Figure 2-7**. Therefore, it is correct in some sense to think of the spin as actually “pointing” along the vector on the Bloch sphere. This one-to-one correspondence between the quantum state and the intuitive vision of a classical angular momentum vector is apparently just a coincidence. For spin other than $1/2$, there is no such direct correspondence. But since here we are typically interested in electron spins, the Bloch sphere provides a useful and intuitive way of thinking about quantum spin states.

2.6 Spin Polarization Detection

In this dissertation, the time resolved magneto-optical method has to be used to initialize and detect spin polarizations. Early investigated, electrical current pulses have been used to research spin states [47]. However, there are several benefits of using optical techniques to study spin dynamics. For example, rather large spin polarizations might be injected easily. Likewise, optical photon is easy to be changed by energy and time. Moreover, the measurement can be carried out by focusing on a 1 mm spot size around. For now, once the spins have been initialized, there are several experimental optical techniques those have been put forward to directly investigate the spin dynamics as described below. Mostly, the spin evolution behavior was studied by time-resolved Kerr

microscopy (TRKM) method [48], time-resolved photoluminescence technique [49], time-resolved Faraday rotation (TRFR) [50] and TRKR measurements [51].

2.6.1 Polarized Photoluminescence

In the previous, it was described how spin is initialized by circularly polarized light due to optical selection rules. These selection rules not only control the absorption but also govern the inverse process of radiative recombination. That is, the certain light will be radiated with circular polarization determined by the spin states of electron and hole, whenever an electron and a hole recombine. Therefore, the spin polarization before recombining could be obtained by measuring the degree of circular polarization of this photoluminescence merely. The degree of circularly polarization P is defined as $P = (I^{\sigma+} - I^{\sigma-}) / (I^{\sigma+} + I^{\sigma-})$, where $I^{\sigma+}$ and $I^{\sigma-}$ are the intensities of right and left circularly polarized radiation [52]. While such a measurement of the polarized photoluminescence cannot give the information about the spin lifetime.

2.6.2 Hanle Effect

With the addition of an external transverse magnetic field, the depolarization measurement of the photoluminescence would become the Hanle effect method [53]. This technique has the greatest advantage of requiring the simple experimental setup. The spin lifetime could be acquired by the variable magnetic field transverse to the direction of the initialized spins with g-factor of the system using this technology [54]. As the spins precession relaxes and the amplitude of the spin along the initial direction decreases with magnetic field. However, if such a Hanle measurement is used alone, only the product of the spin lifetime and the g-factor is obtained. The other disadvantage of using polarized

photoluminescence is that merely the spin coherence at the time of recombination can be measured and the spin coherence persisting after recombination is not easy to be obtained.

All of these above experimental methods can be used to study spin states. However, the ultrafast nonlinear optical time-resolved pump-probe method addressed below is a rather precise way with less dependence on sample properties and provides more information with a higher signal/noise ratio.

2.6.3 Pump-probe Faraday (Kerr) Rotation Techniques

The Faraday (in a transmitted geometry) and Kerr effects (in a reflected geometry) could overcome the above shortcomings. Early in the 1990s, a lot of theoretical results in semiconductors were repeated by David Awschalom's group employing spatial and time-resolved pump-probe techniques. This technique makes one realize the direct detection of the spin lifetime as well as the sub-picosecond study of spin dynamics in bulk GaAs [10, 55]. Pump-probe techniques using short optical pulses or a streak camera may be used to capture temporal dynamics.

When a linearly polarized photon interacts with an electron spin, the Faraday effect results in a rotation of the photon's polarization. Take for example an initially vertically polarized photon that interacts with an electron spin which is either in the "spin up" or "spin down" state. Here, the basis for spin states is defined by the photon propagation direction. To illustrate this, consider a strong spin-photon interaction that rotates the photon polarization by +/- 45 degrees. A photon initially polarized at 45 degrees is in an equal superposition of the basis states, as shown in **Figure 2-7**. If the spin is in the "spin up" or "spin down" state, then the photon winds up in one of the double eigen-states, that is, the photon polarization will be rotated in the opposite direction. But

if the electron is in a superposition of their basis states "up" and "down", then the final state of the spin-photon system will be entangled by the Faraday effect. That is, initial photon state $|\gamma\rangle = |H\rangle + |V\rangle$ entangles with initial spin state $|\mathcal{S}\rangle = |\uparrow\rangle + |\downarrow\rangle$ by Faraday rotation interaction and then becomes the state:

$$|\gamma, \mathcal{S}\rangle = |H\rangle |\uparrow\rangle + |V\rangle |\downarrow\rangle \quad \text{Eq. 2-32}$$

In realistic systems, the angle through which the Faraday effect rotates polarization is quite small. For a small rotation angle, the degree of entanglement would be less than the ideal case shown **Figure 2-8**. Our study aims to detect and characterize this entanglement by double lock-in amplification ways to enhance it and achieve high sensitivity measurement which will be described in the next chapter.

The right and left circularly polarized lights perform different indexes of refraction in a birefringent material, which means the different polarizations as it passes through a material with a non-zero magnetization at different velocities and a phase difference turns up between right and left circularly polarized light. The linearly polarized light is composed of right and left circularly polarized light, whose phase delay comes out as a rotation of the polarization plane of the linearly polarized light as it propagates through a birefringent material. The Kerr effect illustrated in **Figure 2-8** is the same mechanism except being carried out in a reflection rather than a transmitted geometry.

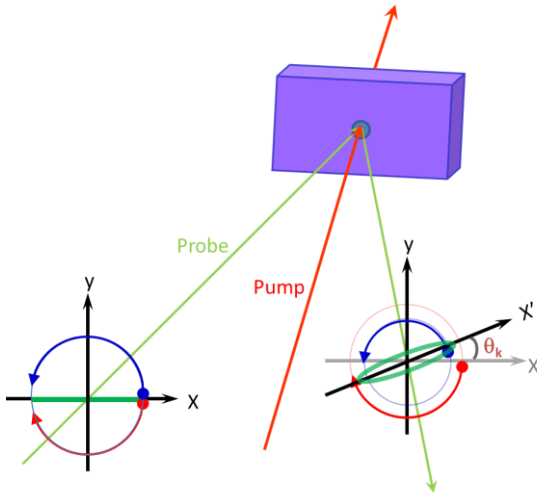


Figure 2-8: Schematic of the Kerr effect. The polarization axis of linearly polarized light is rotated upon reflection from a birefringent material. This rotation angle is proportional to the magnetization along the direction of the light, which in turn is proportional to the difference in the index of refraction for right and left circularly polarized light.

Birefringence can also be induced in materials by a net spin polarization current rather than magnetic fields. Because of the optical selection rules, there are essentially two absorption spectra, one for right and one for left circularly polarized light as illustrated in **Figure 4-14**. We can know that a difference in absorption leads to a difference in refractive indices for right and left circular polarizations. Therefore, the rotation angle of linearly polarization plane is proportional to the corresponding spin polarization.

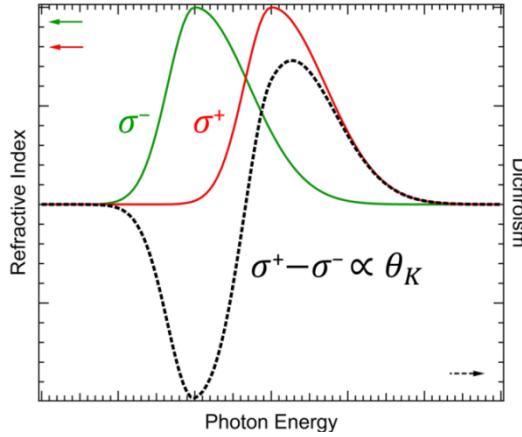


Figure 2-9: Spin-induced Kerr rotation. The refractive indices are shown as a function of photon energy for right and left circularly polarized light. The shift between the two polarizations is due to the different absorption by spin-dependent state-filling. The difference of the refractive index is proportional to the Kerr rotation angle [56].

The Faraday (Kerr) effect has been widely used as a sensitive and noninvasive probe of spins. For both effects, the rotation angle is determined by the difference of the dynamic dielectric response functions for left and right (σ^+ and σ^-) circularly polarized light. For this kind of effect, there are two optical beams to be needed, referred to as the pump and the probe, respectively. The pump must be circularly polarized to create a spin polarization according to the selection rules as described before. Moreover, the probe must be linearly polarized to observe the Faraday (Kerr) rotation. On the case that the pump and probe lasers are continuous wave, steady-state spin polarization information would be obtained, similar to the Hanle measurement described above. In this dissertation, the optical pulses are mainly used to study spin dynamics over time by this mechanism as stated in the next chapter.

2.7 Spin Relaxation

After the nonequilibrium transverse ensemble electron spins are injected into the material as stated above, spin relaxation and spin dephasing will happen. The spin relaxation time is also called longitudinal or spin-lattice time; and the spin dephasing time is sometimes called as the transverse or decoherence spin relaxation time for mobile electrons. The time constants T_1 and T_2 are labeled to describe the spin longitudinal relaxation and spin dephasing processes, respectively [57]. We will mainly briefly describe the spin dephasing mechanisms for the ensemble of electrons spins is excited by an ultrafast laser pulse in this dissertation, which is crucial for developing spintronics devices.

2.7.1 Longitudinal Time

Here, the longitudinal spin relaxation time (T_1) [58] should be mentioned a little. The time T_1 is the time for the longitudinal spin magnetization (along z direction) to reach equilibrium. The relaxation process requires energy transferring between the spin system and, for example, the lattice by phonons. It is the decay time from the upper energy level (for example, a spin-up state) into the lower (spin-down) state in the strong magnetic field applied parallel to spin direction. Equivalently, it is also the time of thermal equilibration of the spin population with the environment. At low temperatures, this decay process involves emission of energy into the environment (such as phonon). This relaxation is irreversible. There are mainly four types of spin relaxation mechanisms [1]: the D'yakonov-Perel's mechanism, the Elliott-Yafet mechanism, the Vir-Aronov-Pikus mechanism and the HFI mechanism. In bulk semiconductors and semiconductor QWs, the D'yakonov-Perel's mechanism is the main mechanism of electron spin

relaxation. The driving force for spin reorientation is the spin-orbit splitting of the conduction band states which acts as a tiny effective magnetic field for the intrinsic tendency of electron spins to precess with the Larmor precession frequency, dependent on the value and direction of the electron wave vector [59]. Scattering of the momentum of the electron randomizes the precession and, in the strong scattering limit, spin reorientation proceeds as a series of random fractional rotations [59].

In general, T_1 is the spin lattice relaxation time [58]. Equivalently it is the typical time of spin population in which the longitudinal magnetization reaches the thermal equilibrium with the lattice. In T_1 process, the energy that is reduced from the transition for the spin system needs to go somewhere, namely other repositories for thermal energy, such as translations, rotations and vibrations, collectively called the lattice. In addition, we know all the processes to cause T_1 relaxation also result in T_2 relaxation. When the system is anisotropic, $T_1 = T_2$. The equality of the two times is very convenient for comparing experiment and theory, since measurements usually yield T_2 , while it is often more convenient to calculate T_1 theoretically.

2.7.2 Transverse Time

By comparison, the time T_2 represent the transverse decoherence time of the precessing electron spin through the randomization of the phase between the two components of a superposition state [60]. This process randomizes the component of the spin state perpendicular to \mathbf{B} . This decoherence is a result of the loss of the phase relation between the two eigenstates, which requires neither any energy transfer nor a change in occupation. Although T_2 relaxation always accompanies T_1 relaxation, the occurring of T_2 relaxation sometimes has nothing to do with T_1 relaxation. For the following of this

dissertation, it therefore will be focused on experimental techniques to probe the transverse spin coherence time in a SQW.

In a SQW, a single electron spin is usually not accessible experimentally. Except the spin coherence definition refers to such a single electron spin, there is a whole ensemble of electron spins $\sim 10^{10}$ electrons per cubic centimeter is excited coherently. Only when all conduction electrons were identical and non-interacting, the transverse decay of net spin magnetization would reflect the intrinsic spin decoherence time of individual electrons.

Another process, known as spin dephasing, affects transverse spin lifetimes and is relevant in the measurement of ensembles of spins or in the time-averaged measurements of single spins. We know a spin will precess around the magnetic field with Larmor frequency of $g\mu_B B/h$, if it is initially perpendicular to the magnetic field. Dephasing arises due to the inhomogeneities in a system: spins at different positions or time precesses at different rates. The resultant scrambling of the average spin polarization causes the measured lifetime to be limited by the inhomogeneous transverse spin lifetime. Since we know two wave packets can interfere to form interference fringes, the action of some fluctuating environment just leads to dephasing. In addition, decoherence will also contribute to dephasing, although decoherence rate can be much less than an ensemble dephasing rate usually. Anyway, spin dephasing time is classically the time it takes for an ensemble of transverse electron spins, initially precessing in phase about the external field (in the Voigt configuration described at length in the next chapter) field, to lose their phase due to the spatial and temporal fluctuations of the precessing frequencies.

However, in addition to such homogeneous dephasing, there might be inhomogeneous effects such as local fluctuated magnetic fields or local variations in the electron g-factor. In such local inhomogeneous magnetic fields, different electron spins precess at different rates, which lead to an extra decay or dephasing of the net electron spin polarization. This could result in a spread of the relative spin orientations within the electron distribution, even when all spins are evolving coherently. In principle, this dephasing effect can be distinguished from decoherence, in case of dephasing remains possibly to recover the initial macroscopic spin magnetization as an example of the spin echo experiments. As the spin echo techniques in time-resolved optical measurements are rarely utilized, the usually measured transverse spin decay time is called as a transverse spin dephasing time T_2 , which is a lower bound to the actual transverse spin coherence time T_2 , unless the inhomogeneous effects can be ruled out. The decay of phase coherence does not involve a change in occupation or a change in the energy of the population [61].

In a word, inhomogeneous and homogeneous processes contribute to T_2 according to $1/T_2 = 1/T_2^h + 1/T_2^{inh}$ where, T_2^h and $1/T_2^{inh}$ are the homogeneous and the inhomogeneous spin relaxation rates, respectively. In general, $T_2 \leq T_2^h$, although for conduction electrons to a very good approximation $T_2 = T_2^h$.

2.7.2.1 *Homogeneous spin dephasing*

Generally, homogeneous spin dephasing [61] occurs in an array of scattering events, where the spin vector changes its direction and/or its magnitude by transferring its angular momentum to other scattering partners. The probability of such a kind of event to happen is the same for all spins with identical properties within a homogeneous spin

ensemble. The net change of spins losing their coherence dN/dt to the total number of spins $N(t)$ at time t is then $dN/dt = -1/T_2^h N(t)$ and $N(t) = N_0 \exp(-t/T_2^h)$, where N_0 is the number of spins at time $t = 0$. Thus, the homogeneous dephasing is mainly characterized by a simple exponential decay except the other time dependencies, one example of which is spin decay via nuclear HFI.

The origin of T_2^h comes from different mechanisms by which spins interact, for example the local or internal magnetic field at a dipole produced by neighboring dipoles or the spread in precession rates produced by the magnetic field that one nucleus produces at another. Classically it is the time that it takes for an ensemble of transverse spins initially precessing in phase to lose their phase with each other. The loss of the ensemble spin phase is irreversible. If the external field is inhomogeneous, one can consider the macroscopic magnetization of the sample in the z-y plane as the sum of smaller magnetization vectors each arising from a small volume experiencing a homogeneous field. Within a small volume with a homogeneous magnetic field, the intrinsic relaxation time which is characteristic of the magnetization decay is T_2^h and it is an irreversible process.

2.7.2.2 Inhomogeneous spin dephasing

The electron spin dephasing definitely happen if electrons are in an effective magnetic field, resulting from the lack of inversion symmetry, such as that in a QW. Furthermore, due to the inhomogeneity of the magnetic field, each of the small volume will precess with its own characteristic Larmor frequency. As an example, inhomogeneous dephasing caused by a spread Δg in the electron g-factors is given by $1/T_2^{inh} = 1/T_{\Delta g} + \Delta g \mu_B B / \sqrt{2}$. The term $\Delta g \mu_B B / \sqrt{2}$ is the field inhomogeneity This

reduction originates from an effect of the macroscopic averaging of individual spin precession with slightly different Larmor frequency via the small g distribution, which can be explained by the distribution of g due to the inhomogeneous fluctuation of well width and alloy composition of the barrier material for our sample. The phase loss due to the inhomogeneity of the magnetic field is reversible. As a result, the magnetization from each small volume of spin will get out of phase with each other. Due to the inhomogeneity of the magnetic field in the experiment, the ensemble effect of T_2 is usually dominating [61].

In conclusion, although a spin lifetime T^* is generally given by $1/T^* = 1/T_1 + 1/T_2$ with lifetime T_1 and transverse spin-relaxation time T_2 for ensemble spins. In the case of RESP in this dissertation, there is not any transferring energy, such as transitions, rotations and vibration. T_1 is almost infinity and we can ignore S_{\parallel} component, Therefore $T^* = T_2$. In many cases, a single symbol τ_s is used for spin relaxation and dephasing, as well as called indiscriminately as either of these terms [61]. For spintronics applications, longer spin relaxation time τ_s is desired as most times when the spin lives longer, it implies better performance and functionality of the device. There have been numerous researches to explore the spin relaxation time of semiconductors. The longest spin relaxation time found in bulk GaAs is about hundreds of ns.

2.8 References

- [1] M. I. Dyakonov. Spin Physics in Semiconductors[B]. Berlin: Springer; 2008.
- [2] P. C. s. m. Lauterbur. Image Formation by Induced Local Interactions - Examples Employing Nuclear Magnetic-Resonance[J]. Nature 1973; **242**: 190-191.
- [3] K. s. m. Wuthrich. The way to NMR structures of proteins[J]. Nat Struct Mol Biol 2001; **8**: 923-925.
- [4] D. D. Awschalom, M. E. s. m. Flatte. Challenges for semiconductor spintronics[J]. Nat Phys 2007; **3**: 153-159.
- [5] C. Chappert, A. Fert, F. N. s. m. Van Dau. The emergence of spin electronics in data storage[J]. Nat Mater 2007; **6**: 813-823.
- [6] J. M. Kikkawa, I. P. Smorchkova, N. Samarth, D. D. Awschalom. Room-temperature spin memory in two-dimensional electron gases[J]. Science 1997; **277**: 1284-1287.
- [7] E. Brun, R. J. Mahler, H. Mahon, W. L. Pierce. Electrically Induced Nuclear Quadrupole Spin Transitions in a Gaas Single Crystal[J]. Physical Review 1963; **129**: 1965.
- [8] G. Lampel. Nuclear Dynamic Polarization by Optical Electronic Saturation and Optical Pumping in Semiconductors[J]. Phys. Rev. Lett. 1968; **20**: 491-493.
- [9] M. N. Baibich, J. M. Broto, A. Fert, F. N. Vandau, F. Petroff, P. Eitenne, et al. Giant Magnetoresistance of (001)Fe/(001) Cr Magnetic Superlattices[J]. Phys. Rev. Lett. 1988; **61**: 2472-2475.
- [10] J. M. Kikkawa, D. D. Awschalom. Lateral drag of spin coherence in gallium arsenide[J]. Nature 1999; **397**: 139-141.
- [11] P. Palinginis, H. Wang. Coherent Raman scattering from electron spin coherence in GaAs quantum wells[J]. J Magn Magn Mater 2004; **272**: 1919-1920.
- [12] H. Kosaka. Photon-to-electron quantum information transfer[J]. Journal of Applied Physics 2011; **109**: 105414.
- [13] E. J. Gansen, A. L. Smirl. Ultrafast polarization modulation induced by the "virtual excitation" of spin-polarized excitons in quantum wells: Application to all-optical switching[J]. J. Appl. Phys. 2004; **95**: 3907-3915.

- [14] S. A. Wolf, D. D. Awschalom, R. A. Buhrman, J. M. Daughton, S. von Molnar, M. L. Roukes, et al. Spintronics: A spin-based electronics vision for the future[J]. *Science* 2001; **294**: 1488-1495.
- [15] R. Fiederling, M. Keim, G. Reuscher, W. Ossau, G. Schmidt, A. Waag, et al. Injection and detection of a spin-polarized current in a light-emitting diode[J]. *Nature* 1999; **402**: 787-790.
- [16] M. Oestreich. Material science - Injecting spin into electronics[J]. *Nature* 1999; **402**: 735-737.
- [17] Y. Ohno, D. K. Young, B. Beschoten, F. Matsukura, H. Ohno, D. D. Awschalom. Electrical spin injection in a ferromagnetic semiconductor heterostructure[J]. *Nature* 1999; **402**: 790-792.
- [18] M. P. Walser, C. Reichl, W. Wegscheider, G. Salis. Direct mapping of the formation of a persistent spin helix[J]. *Nat Phys* 2012; **8**: 757-762.
- [19] <http://www.iue.tuwien.ac.at/phd/ungersboeck/node41.html>.
- [20] S. Chadov, X. Qi, J. Kübler, G. H. Fecher, C. Felser, S. C. Zhang. Tunable multifunctional topological insulators in ternary Heusler compounds[J]. *Nat Mater* 2010; **9**: 541-545.
- [21] http://en.wikipedia.org/wiki/K%C2%B7p_perturbation_theory.
- [22] P. J. Mohr, B. N. Taylor, D. B. Newell. CODATA Recommended Values of the Fundamental Physical Constants: 2010a[J]. *Journal of Physical and Chemical Reference Data* 2012; **41**: 043109.
- [23] J. Singh. Electronic and Optoelectronic Properties of Semiconductor Structures[B]. Cambridge University Press; 2007.
- [24] M. A. Parker. Solid State and Quantum Theory for Optoelectronics[B]. CRC Press; 2009.
- [25] C. Hamaguchi. Basic Semiconductor Physics[B]. Springer; 2001.
- [26] W. A. Harrison. Electronic Structure and the Properties of Solids: The Physics of the Chemical Bond[B]. Dover Publications; 2012.
- [27] B. Kuhnheinrich, W. Ossau, T. Litz, A. Waag, G. Landwehr. Determination of the Band-Offset in Semimagnetic Cdte Cd_{1-X}Mn_XTe Quantum-Wells a Comparison of 2 Methods[J]. *Journal of Applied Physics* 1994; **75**: 8046-8052.

- [28] J. C. Hall, J. C. Dunlap, T. Friedmann, F. Giannelli. Advances in Genetics[B]. Elsevier Science; 1999.
- [29] P. Harrison. Quantum Wells, Wires and Dots: Theoretical and Computational Physics of Semiconductor Nanostructures[B]. Wiley; 2011.
- [30] L. Jacak, P. Hawrylak, A. Wójs. Quantum Dots[B]. Springer; 1998.
- [31] M. L. Cohen, J. R. Chelikowsky. Electronic structure and optical properties of semiconductors[B]. Springer-Verlag; 1989.
- [32] H. C. Gupta. Solid State Physics[B]. Vikas Publishing House Pvt Limited; 2001.
- [33] J. H. Davies. The Physics of Low-dimensional Semiconductors: An Introduction[B]. Cambridge University Press; 1998.
- [34] S. A. Crooker, M. Furis, X. Lou, C. Adelmann, D. L. Smith, C. J. Palmstrom, et al. Imaging spin transport in lateral ferromagnet/semiconductor structures[J]. *Science* 2005; **309**: 2191-2195.
- [35] E. I. Rashba. Theory of electrical spin injection: Tunnel contacts as a solution of the conductivity mismatch problem[J]. *Phys. Rev. B* 2000; **62**: R16267-R16270.
- [36] A. T. Hanbicki, B. T. Jonker, G. Itskos, G. Kioseoglou, A. Petrou. Efficient electrical spin injection from a magnetic metal/tunnel barrier contact into a semiconductor[J]. *Applied Physics Letters* 2002; **80**: 1240-1242.
- [37] C. Adelmann, X. Lou, J. Strand, C. J. Palmstrom, P. A. Crowell. Spin injection and relaxation in ferromagnet-semiconductor heterostructures[J]. *Phys. Rev. B* 2005; **71**: 121301
- [38] A. Katsuki, K. Akiyama, Y. Ikegami, S. Terokubota. Spin-Orbit Coupling-Induced Electron-Spin Polarization Observed in Photosensitized Electron-Transfer Reactions between Xantbene Dyes and P-Quinones[J]. *Journal of the American Chemical Society* 1994; **116**: 12065-12066.
- [39] B. A. Joyce, N. P. D. Division, N. A. T. O. P. D. Division, B. A. C. Growth. Quantum Dots: Fundamentals, Applications, and Frontiers: Proceedings of the NATO ARW on Quantum Dots: Fundamentals, Applications and Frontiers, Crete, Greece 20 - 24 July 2003[B]. Springer; 2006.

- [40] H. Wang, S. O?Leary. Electromagnetically induced transparency from electron spin coherences in semiconductor quantum wells [Invited][J]. *J. Opt. Soc. Am. B* 2012; **29**: A6-A16.
- [41] D. F. Cesar, M. D. Teodoro, H. Tsuzuki, V. Lopez-Richard, G. E. Marques, J. P. Rino, et al. Contrasting LH-HH subband splitting of strained quantum wells grown along [001] and [113] directions[J]. *Phys. Rev. B* 2010; **81**: 233301.
- [42] S. Bandyopadhyay, M. Cahay. Introduction to Spintronics[B]. CRC Press; 2008.
- [43] Y. B. Band, Y. Avishai. Quantum Mechanics with Applications to Nanotechnology and Information Science[B]. Elsevier Science; 2013.
- [44] J. J. Sakurai, J. Napolitano. Modern quantum mechanics[B]. 2nd ed. Boston: Addison-Wesley; 2011.
- [45] M. A. Nielsen, I. L. Chuang. Quantum Computation and Quantum Information: 10th Anniversary Edition[B]. Cambridge University Press; 2010.
- [46] M. J. Padgett, J. Courtial. Poincaré-sphere equivalent for light beams containing orbital angular momentum[J]. *Optics Letters* 1999; **24**: 430-432.
- [47] J. Kim, J. Puls, Y. S. Chen, G. Bacher, F. Henneberger. Electron-nuclear spin control in charged semiconductor quantum dots by electrical currents through micro-coils[J]. *Appl Phys Lett* 2010; **96**: 151908.
- [48] S. Matsuzaka, Y. Ohno, H. Ohno. Detection of local electron and nuclear spin dynamics by time-resolved Kerr microscopy[J]. *Physica E: Low-dimensional Systems and Nanostructures* 2010; **42**: 2702-2706.
- [49] T. Ito, W. Shichi, Y. Nishioka, M. Ichida, H. Gotoh, H. Kamada, et al. Dependence of electron spin g-factor on magnetic field in quantum wells[J]. *Journal of Luminescence* 2008; **128**: 865-867.
- [50] B. Li, P. Coles, J. A. Reimer, P. Dawson, C. A. Meriles. Optical pumping of nuclear spin magnetization in GaAs/AlAs quantum wells of variable electron density[J]. *Solid State Commun.* 2010; **150**: 450-453.
- [51] M. Ono, S. Matsuzaka, Y. Ohno, H. Ohno. Gate Voltage Control of Nuclear Spin Relaxation in GaAs Quantum Well[J]. *J. Supercond. Nov. Magn.* 2010; **23**: 131-133.
- [52] F. Meier, B. P. Zakharchenya. Optical orientation[B]. North-Holland; 1984.

- [53] R. R. Parsons. Band-to-Band Optical Pumping in Solids and Polarized Photoluminescence[J]. Phys. Rev. Lett. 1969; **23**: 1152-1154.
- [54] A. S. Bracker, E. A. Stinaff, D. Gammon, M. E. Ware, J. G. Tischler, A. Shabaev, et al. Optical pumping of the electronic and nuclear spin of single charge-tunable quantum dots[J]. Phys. Rev. Lett. 2005; **94**: 047402
- [55] J. M. Kikkawa, D. D. Awschalom. Resonant spin amplification in n-type GaAs[J]. Phys. Rev. Lett. 1998; **80**: 4313-4316.
- [56] P. S. Pershan. Magneto-Optical Effects[J]. Journal of Applied Physics 1967; **38**: 1482-&.
- [57] M. Gallart, S. Cronenberger, C. Brimont, B. Honerlage, P. Gilliot. Exciton-spin dephasing and relaxation due to symmetry breaking in two-band bulk semiconductors[J]. Phys. Rev. B 2008; **77**: 155212.
- [58] P. Michler. Single Semiconductor Quantum Dots[B]. Springer Berlin Heidelberg; 2009.
- [59] M. M. Glazov, E. L. Ivchenko. Effect of electron-electron interaction on spin relaxation of charge carriers in semiconductors[J]. Journal of Experimental and Theoretical Physics 2004; **99**: 1279-1290.
- [60] A. M. Tyryshkin, S. A. Lyon, A. V. Astashkin, A. M. Raitsimring. Electron spin relaxation times of phosphorus donors in silicon[J]. Phys. Rev. B 2003; **68**: 193207.
- [61] I. Zutic, J. Fabian, S. Das Sarma. Spintronics: Fundamentals and applications[J]. Reviews of Modern Physics 2004; **76**: 323-410.

CHAPTER 3

EXPERIMENTAL SAMPLE AND METHOD

3.1 CdTe QW Sample

In this dissertation, the used sample is a lightly n-doped semiconductor CdTe/Cd_{0.85}Mg_{0.15}Te SQW grown by the molecular-beam epitaxy (MBE) technology. Of course, CdTe is one of the typically attractive semiconductor compounds. It is well known that semiconductors are commonly covalently bonded substances. Moreover, they are a special type of materials with the narrow band-gaps of several electron-volts. Thus, their properties are in-between those of insulators and conductors. Therefore, this CdTe SQW owns the double characteristics of semiconductor and the quantum size nanostructure. However, to build up a specifically and fully microscopic model for RESP dynamics in this SQW, detailed understanding of the basis of sample's crystal nanostructure, confinements and carrier features might be required.

3.1.1 MBE Preparation

The epitaxial growth of this CdTe sample here was accomplished by the MBE process, which is usually carried out in an ultra-high vacuum environment through the chemical reaction of one after one thermal molecular beams on the crystal surface of a substrate [1]. The ultra-high vacuum environment is essential to minimize mechanical impurity in the deposited layers from the residual background. Additionally, it is sometimes provided by the liquid-nitrogen-cooled cryo-panels. Molecular beams

generated by thermal effusion cells produce a single crystal layer through interacting on a heated crystal substrate. Each cell layer contains one of the constituent elements or compounds. The desired molecular beam is evaporated to flux at the picked temperature, so that the vapor pressures can be obtained to be enough high to generate thermal energy molecular beams by the composition's free evaporation and films.

This growth process is highly controllable via the reality of inserting mechanical stops or shutters between each cell and the substrate. In addition, the epitaxial films of the expected chemical components and crystal orientation can be acquired through the properly operation and suitable instruments between each cell and the substrate and picking an appropriate substrate temperature. The highly precisely controlling in the beam flux of the corresponding composition makes the realization of the growth of very monolayers thick layer.

3.1.2 Crystal Structure

CdTe semiconductors crystallize in zinc-blende structure composed of two interpenetrating face-centered cubic (FCC) lattices. Each of the atomic species of Cd and Te forms a FCC lattice, which is shifted relative to the other by one fourth of the main cube diagonal ($a_0/4, a_0/4, a_0/4$) along the diagonal of the unit cell, where a_0 is called the lattice constant or lattice parameter and is a measure of the size of the unit cell, as shown in **Figure 3-1** (a). In this structure of II-VI binary compound, each Cd atom shares four valence electrons with its nearest neighbors formed from four atoms of Te, placed at the four vertices of a regular tetrahedron, and vice versa, as displayed in **Figure 3-1** (b). Therefore, an elementary cell of the zinc-blende lattice contains one atom of each species. In each unit cell, there are 8 outer electrons which contribute to the chemical bonds

formed between the closest atoms. The wave functions of other inner electrons close to lattice nuclei cannot contribute to the transport or to the near band-gap optical properties.

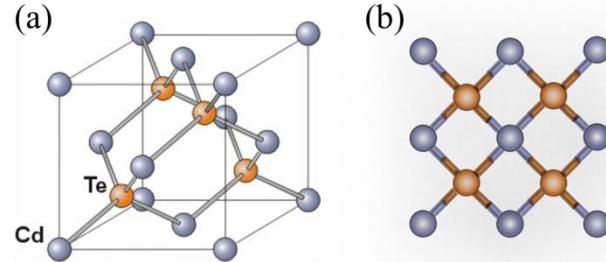


Figure 3-1: (a) Unit cell of a CdTe crystal; (b) 2-D representation of CdTe crystal: Cd and Te alternate through the lattice on their individual FCC sub-lattices.

This CdTe SQW was particularly adequate for bound excitons studies. Because the Coulomb interaction in II-VI semiconductors is typically twice as large as the one in III-V compounds [2]. Also because, due to the electronic confinement, the trion binding energy is expected to be an order of magnitude larger than in bulk materials [3], even larger than III-V compounds. In addition, it has a direct band gap located at the center of the Brillouin zone. These properties make it favorably suited for optical studies. Additionally, a CdTe SQW sample has the properties of well-resolved, strong trion absorption resonance, weak nuclear field, which is demonstrated in the below.

3.1.3 CdTe SQW and Confinement Effects

In detail, the sample of a CdTe/Cd_{0.85}Mg_{0.15}Te SQW is high quality naturally-doped on a (100)-GaAs substrate. Additionally, one atomic mono layer (ML) of CdTe is $\sim 3.242 \text{ \AA}$ (lattice constant: 6.483 \AA). Therefore, our sample consisting of 30 ML of CdTe has the well width of about 10 nm as diagrammed in **Figure 3-2 (b)**. What is more, the tunneling of resident electrons can be negligible. The sample used in this study is not

intentional doping, but the impurities are working as a dopant derived from the formation process technically. The excess electrons (resident electrons) with quite small density residing in the potential well form a background of an electron spin ensemble.

The valence band structure can be largely affected by the uniaxial strain, in particular [4]. Unfortunately, the subtle strain and dislocations on the valence bands are not observed directly in this studied sample. Moreover, in comparison to the electrons in a bulk system, the electrons confined in a SQW could have significantly different electronic properties. First of all, the reduction in spatial dimensionality breaks a number of symmetries present in bulk causing changes in the band structures. As the explanation in the previous chapter, the confinement along one dimension results in quantized energy levels and envelope functions characteristic of a single QW along one direction, while the other directions are characterized by the continuous energy dispersion of the bulk. The main confinement energy band as ideal simple steps in potential energy for the typical square CdTe QW is shown in **Figure 3-2** (a). In the band structure, a sub-band emerges centered around each QW energy level as a quasi-two-dimensional density of states, as presented before.

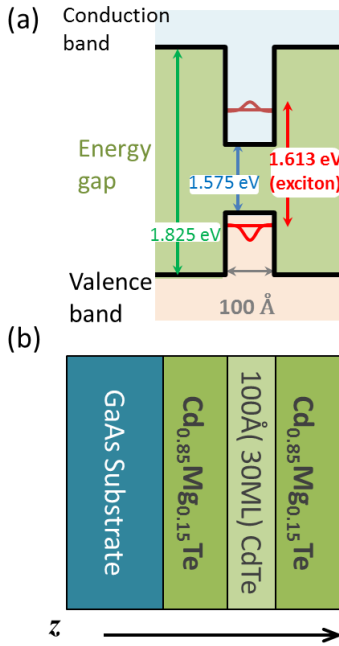


Figure 3-2: (a) The confinement energy bands for the QW sample used in our research. (b) The sample structure consisting of 10 nm CdTe well and Cd_{0.85}Mg_{0.15}Te barriers.

3.2 Carriers in the SQW Sample

3.2.1 Selection Rule of Heavy Hole and Light Hole in a SQW

As we mentioned above, there are two kinds of holes that are relevant in the SQW here, corresponding to the heavy hole and light hole bands. Since these holes have different masses, there are double sets of hole subbands with different energy spacing. The light hole subbands are spaced further apart due to their lighter mass in the confinement condition. Thus, the heavy-hole-to-conduction set is more closely spaced than the light-hole-to-conduction set.

In the way of a waveguide with light propagating along the quantum well layers, there are two distinct optical polarization directions: one with the optical electric vector perpendicular to the quantum well layers; and the other with the optical electric vector

parallel to the quantum well layers [5, 6]. The former case of transverse vector is substantially different by that the optical electric vector is always parallel to the quantum well planes (perpendicular to the direction of propagation) for a plane wave. For this transverse vector, the heavy-hole-to-conduction transitions are forbidden, because of microscopic selection rules associated with the unit cell wave functions. Then all the absorption strength goes over to the light-hole-to-conduction transitions. Hence, there is now only one set of steps in the absorption with such a simple model. This kind of selection rule is a consequence of defining a definite symmetry axis in the material. In this case, it is just the growth direction of the QW layers. The loss of the heavy hole transitions does happen not merely in QWs. The exact same selection rule phenomenon would also happen only if a uniaxial stress is supplied to a bulk semiconductor. There are more heavy holes than light holes in thermal equilibrium. Hence, the gain associated with heavy holes is larger.

The latter case of parallel vector is essentially identical to the situation for light propagating perpendicular to the layers, where the optical electric vector is always in the plane of the QWs [7]. When we look at the optical absorption for light propagating perpendicular to the quantum well layers, the heavy hole set is commonly dominant. In this dissertation, we focused on transitions between the heavy-hole band and the conduction band in a SQW.

3.2.2 Resident Electrons Density in a SQW

We have a great deal of interest in the formation processes of RESP and its initial spin dynamics in quantum nanostructures for potential applications of the spin degree of freedom in the future semiconductor electro-optic devices and quantum information

processing [8-12]. These future applications could benefit from a long spin coherence that is not limited by energy relaxation process such as recombination with holes. Considering the different density of resident 2D electrons n_e , three different situations could take place in experiments on the coherent spin dynamics in QWs under the resonant optical excitation. For undoped samples (**Figure 3-3 (a)**, $n_e = 0$), spin oriented excitons are photo-generated. In this case the coherent spin dynamics of either an exciton or an electron in the exciton merely can be lived during the short exciton lifetime.

For a high density two-dimensional electron gas (2DEG) ($n_e a_B^2 > 1$, where a_B is the exciton Bohr radius) as displayed in **Figure 3-3 (c)**, exciton formation is suppressed because of the state-filling and screening effects. After photo-generation, the hole loses its spin and energy quickly and recombines with an electron from the 2DEG. However, the spin oriented electron, photo-generated at the Fermi level, has infinite lifetime, which is rather important for allowing one to study its long-lived spin coherence and spin relaxation. As a result, a circularly polarized photon can change the spin polarization of the 2DEG by $S = \pm 1/2$ [13].

In the case of diluted resident electrons ($n_e a_B^2 \ll 1$) as shown in **Figure 3-3 (b)**, the mechanism for generation of electron spin coherence is not so obvious. The lowest in energy optical transition corresponds to a negatively charged trion consisting of two electrons and one hole [14]. The ground state is a singlet trion with antiparallel orientation of the electron spins by the resonant excitation. Then the contributed polarization for RESP becomes complicated due to the trions dynamics. In the simplest way, this state does not contribute directly to the spin polarization, if the hole undergoes fast simple decoherence.

However, generation of electron spin coherence has been observed experimentally under resonant excitation of trions, both for QWs [15] and QDs [16]. There are two equivalent approaches to explain this generation, which are detailed described in the previous work [13]. The first one suggests that a coherent superposition of electron and trion states is excited by a circular polarized light pulse when the system is subject to an external magnetic field [15, 16]. The second one is based on considering the resident electrons which are involved in the trion formation: under circular polarized excitation electrons with a specific spin orientation will be taken from the 2D resident electrons resemble and, consequently, spin polarization with an opposite sign is induced [13, 17].

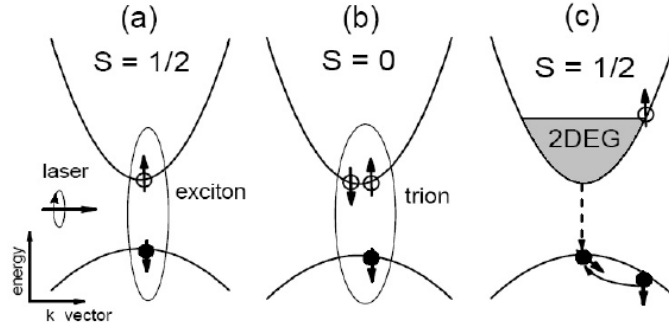


Figure 3-3: Schematic presentation of generation of carrier spin coherence by circular polarized laser pulses. The three cases differ with respect to the density of the 2DEG in the QW: (a) Empty well, only photo-generated carriers are present, which become bound to form excitons; (b) Low density of diluted resident electrons, trions with a singlet ground state are formed by a photo-generated exciton and a background electron. The interaction of the trion with the 2DEG is negligible; (c) Dense 2DEG with a Fermi energy exceeding the exciton binding energy. Bound complexes such as excitons and trions are suppressed [13].

3.2.3 Photoluminescence (PL) Measurement

The photoluminescence (PL) of the CdTe SQW sample as a function of photon energy measured under the cw-excitation at 1.650 eV and at 10 K is shown in **Figure 3-4**. The PL spectra can be fitted by the sum of two Lorentzian functions. **Figure 3-4**

illustrates the two observed optical transitions, which are clearly separated by the trion binding energy of 2.3 meV. From all the external conditions dependences of PL, referring to the previous measurements in our group, a higher peak is observed at a photon energy of $h\nu = 1.6110$ eV, which is attributed to the recombination from the negatively-charged trion (T) state. Moreover, due to the neutral heavy-hole excitons (X^0) transition, a lower peak appears (1.6133 eV) higher in energy. The assignments of the observed peaks are consistent with the reported measurement [13] on similar structure. In this QW sample, it was not found any evidence of a positively charged exciton. Using circularly polarized excitation, spin polarized electrons and heavy holes can be pumped due to the optical selection rules as explained in more detail in Section 2.4. For the purposes of discussion, spin polarization parallel to the σ^- optically injected electron spin polarization will be referred to as “spin-up”, and the opposite spin as “spin-down”. The injected RESP is determined by switching the helicity of the pump from σ^- to σ^+ .

The confinement along the growth direction in a SQW reduces the degrees of freedom of electrons and holes. Then the binding energy of exciton in a SQW is greater than in 3-dimensional bulk semiconductors. Therefore, there is a clearly defined spectral resonance standing off the band edge due to the higher exciton binding energy. In particular, this trion binding energy (~ 2.3 meV) for that CdTe SQW is much larger than that in a GaAs QW (~ 1.6 meV) [18].

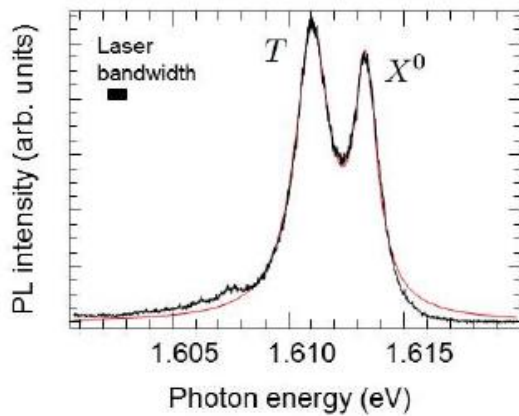


Figure 3-4: PL spectrum excited at 1.65 eV at 10 K in the studied CdTe/(CdMg)Te SQW. Negative trion (T) and neutral exciton (X^0) are clearly separated. Excitation bandwidth is also indicated by a bar.

3.2.4 Neutral Exciton

A basically neutral exciton (X^0) mentioned above consists of an electron in the conduction band and a hole in the valence band result from band edge optical excitations in semiconductors, like a Hydrogen-like bound state, as shown in **Figure 3-5** (b). Thus, the electron-hole interaction of X^0 can be allowed to be simulated by the effective mass of its electrons and holes in the same way of studying a Hydrogen atom using the Schrödinger equation like what **Figure 3-5** (a) shows. However, the coulomb attraction between electrons and holes is reduced by the electric field screening due to a large dielectric constant in semiconductors unlike a hydrogen atom. Additionally, the smaller effective masses of electron and hole also lead to a weaker binding energy than that in the hydrogen atom.

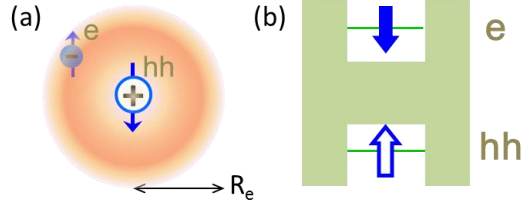


Figure 3-5: (a) Diagram of an exciton where an electron-heavy hole pair forms an e-hh particle like a hydrogen atom; (b) An exciton in the Band diagram. A electron and a hole are bound by the Coulomb attraction into excitons with a hydrogen-like spectrum.

3.2.5 Trion

A trion is a three-particle complex composed of two electrons and one hole (generally expressed as X^-) or two holes and one electron (generally expressed as X^+), which modulates the band level of exciton transition mentioned above. In this dissertation, there exists negatively-charged trion alone (labeled T in the following). From the PL information above, it is simple to directly couple the spin states of the electrons in the background to trion states by tuning a laser to the trion resonance. The properties of a charged exciton are possible to be estimated in the same way of modeling the Helium atom, as displayed in **Figure 3-6** (a). Besides, **Figure 3-6** (b) shows that the electrons are in the conduction band and the hole exists in the valence band. The stability of trions was firstly predicted by Lampert [19]. The first experimental observation of a trion signature was successfully carried out by Kheng et al. in a CdTe QW [20]. Since this first experimental observation, trions have been clearly identified in QWs for several semiconductor compounds, such as GaAs [21] and ZnSe [22]. It is easy to note that the radius of the trion is much larger than that of the exciton as a result of the relatively weak

binding energy. This energy is required to separate the trion into a neutral exciton and an unbound electron.

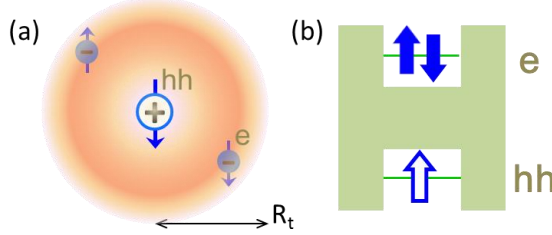


Figure 3-6: (a) The trion which is made up of two electrons and a single heavy hole; (b) A trion in the Band diagram. Electrons and hole are bound by the Coulomb attraction into trions with a Helium-like particle.

To estimate the binding energy of a negatively charged trion, there are a lot of sophisticated ways to obtain rather accurate estimates for the binding energy, which typically involve more complex trial wave functions [23]. All the previous theoretical analysis of trion binding energy proves that the binding energy of trions increases with the confinement. For example, it increases from about 10% of the exciton binding energy in bulk semiconductors to about 50% in the QW [24]. The simplest relation used to estimate the binding energy of trions for the QWs with a limited thickness is shown here [24]:

$$E_B^T \approx \frac{R_y}{3\sqrt{L/a_B}} \quad \text{Eq. 3-1}$$

where a_B is the exciton Bohr radius $a_B = \hbar^2 \varepsilon / m^* e^2$ (~ 68.8 Å for CdTe) [25], L is the well width (100 Å for our CdTe SQW sample); R_y is the effective Rydberg energy [26]; $R_y = m^* e^4 / 2\hbar^2 \varepsilon^2 \sim 7.7$ meV by the effective reduced mass mentioned in Chapter 2, as well as the dielectric constant of the semiconductor is $\varepsilon = 9.4$ for CdTe [27]. In our

system, the calculated binding energy from the above **Eq. 3-1** is ~ 2.1 meV. However, we experimentally observed a spectral resonance of trion formation with ~ 2.3 meV below the exciton resonance, as seen in **Figure 3-4**. Therefore the binding of an exciton to a charged electron for trion formation is active. Hence, we also know that there must be some excess electrons present to form a negatively charged trion.

Since the two electrons in the trion combine into a spin-singlet state, the polarization of trion is determined by the hole-spin. The analysis for the Kerr rotation signals in next chapter indicates that the heavy hole undergoes a spin-flip before recombination in most cases for our experiments. One reference set forth that hole-spin-flips could occur either during energy relaxation in the nano-sized InP islands [28].

3.3 Ultra-short Pulse

In this dissertation, our laser system consists of an oscillator pumped by a Coherent Verdi 7.5 W continuous wave (CW) laser and MIRA900 D Coherent employing a picosecond mode-locked Ti: sapphire as a gain medium. All the ultrafast optical ultrafast optical pulse lasers are split by a single laser beam used with ~ 2 ps pulse width for its full width at half maximum (FWHM) and with a continuous pulse repetition rate of near ~ 76 MHz. In this case, a pulse with a low power density of about 10 mW/cm² would create about 10^8 excitons/cm² learned from the later reference [29].

The time width of the light pulse is very important because that the transient spins dynamics' investigations require ultrafast optical pulses. However, determining the duration of ultra-short pulses is a tough task, because there are no electronic detectors that can directly measure on a picosecond timescale. In this dissertation, the pulses are characterized by the intensity autocorrelation using the Second Harmonic Generation

(SHG; also called frequency doubling), which is a nonlinear optical phenomenon of the electrical polarization about photons interacting with a special crystal with the second-order nonlinearity. The double incident lights with the same frequency ω are recombined to form new photons with twice the energy. Therefore, twice the frequency ($\omega_N = 2\omega$) and half the wavelength of the initial photons in the time domain due to the large electromagnetic light field as a kind of sum frequency generation.

In the SHG measurement, the incoming pulse requiring high peak power is split into two beams by a beam splitter (BS) and then the both beams overlap spatially and temporally in a SHG nonlinear-optical crystal, while measuring the crossing correlated SHG spectrum, as shown in **Figure 3-7**.

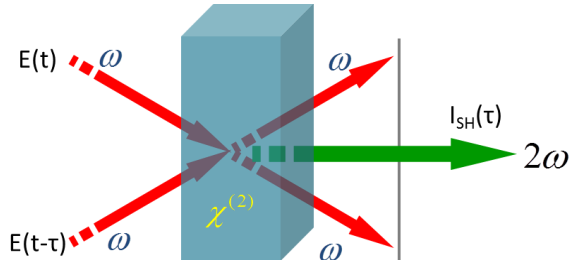


Figure 3-7: Optical diagram of an auto-correlator. The input pulse is split into two parts, one of which is sent into a delay stage. Besides, they are recombined onto a nonlinear crystal for a second-harmonic generation. Scanning the time-delay of the two parts gives the SHG intensity as a function of delay time, which corresponds to the time-domain profile of the input light.

One of two beams in **Figure 3-7** is variably delayed with respect to the other by a delay line. The both beams are recombined in the SHG crystal and the output is measured. A SHG crystal produces an electrical field from the electric fields of the two beams, at twice the frequency of the original pulse. An intensity trace $I_{sig}^{SHG}(\tau)$ of the autocorrelated SHG electric field is proportional to the product of the intensities of the two pulses:

$$I_{sig}^{SHG}(\tau) \propto I(t)I(t-\tau) \quad \text{Eq. 3-2}$$

where $I(t)$ is the pulse intensity and τ is the delay between the two split pulses. The SHG intensity $G_0^{(2)}(\tau)$ measurement of the time-resolved intensity autocorrelation produces the time integral over the overlapped time (Because there is no second harmonic intensity if the pulses do not overlap in time domain):

$$G_0^{(2)}(\tau) \equiv \int_{-\infty}^{\infty} I(t)I(t-\tau)dt \quad \text{Eq. 3-3}$$

Thus, the intensity of the second harmonic signal, generated by mixing of the two fundamental fields, depends on the temporal overlap of the pulses. As a result, the autocorrelation signal can be measured as a physical distance, while the pulse duration is not measurable directly. The pulse duration can be calculated from the autocorrelation signal. In **Figure 3-8** (a), the intensity autocorrelation trace of a perfect Gaussian pulse is shown with this following function form:

$$G_0^{(2)}(\tau) = Be^{-\left(\frac{\tau\sqrt{4\ln 2}}{\Delta\tau_G}\right)^2} \quad \text{Eq. 3-4}$$

Where, τ is true time shift of one of the pulse, that is, the measuring time shift of autocorrelation signal on oscilloscope; $\Delta\tau_G$ is the FWHM pulse duration of autocorrelation signal; B is the coefficient. Besides, the width of the autocorrelation can be related to the width of the original pulses. To analyze such data, the intensity $I(t) \propto |E(t)|^2$ about the complex electric field $E(t)$ of the original ultra-short pulse shape is assumed here:

$$I(t) = Ae^{-\left(\frac{t\sqrt{4\ln 2}}{\tau_p}\right)^2} \quad \text{Eq. 3-5}$$

where, τ_p is FWHM pulse duration of original pulse; t is pulse time; A is the coefficient.

Then, the autocorrelation intensity about the convolution of the original light pulses will be:

$$\begin{aligned}
 G_0^{(2)}(\tau) &\equiv \int_{-\infty}^{\infty} I(t)I(t-\tau)dt \\
 &= A^2 \int_{-\infty}^{+\infty} e^{-\left(\frac{t\sqrt{41n2}}{\tau_p}\right)^2} e^{-\left(\frac{(t-\tau)\sqrt{41n2}}{\tau_p}\right)^2} dt \\
 &= \frac{\tau_p A^2 \sqrt{\pi}}{2\sqrt{2\ln 2}} e^{\left(\frac{\tau}{\tau_p/\sqrt{2\ln 2}}\right)^2}
 \end{aligned} \tag{Eq. 3-6}$$

As a result, $\tau_p = \Delta\tau_G/\sqrt{2}$ is obtained by comparing **Eq. 3-5** and the solution of **Eq. 3-6**. Therefore, the shape of the original ultra-short pulse with the FWHM = 1.96 ps is acquired as shown in **Figure 3-8 (b)**.

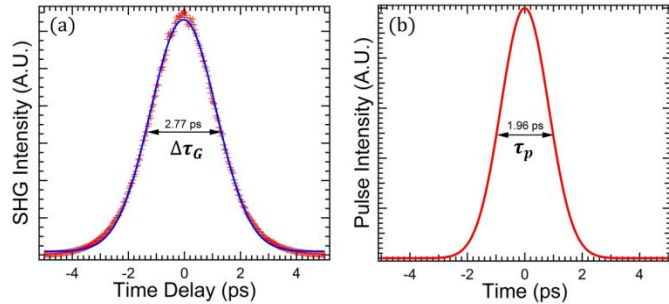


Figure 3-8: The calculated picosecond pulse of 1.96 ps (b) and its SHG autocorrelation trace (a). The SHG trace is fitted to a Gaussian curve (blue curve) with its FWHM = 2.77 ps.

A pulse in the time domain corresponds to a bandwidth in the frequency domain:

$\Delta\nu_L \approx 1/\tau_p$, where $\Delta\nu_L = 5.102 \times 10^{11} \text{s}^{-1}$ is the laser bandwidth of frequency.

Therefore, the laser medium has provided gain over a quite broad spectral bandwidth to

obtain this ultra-short pulse. Therefore, the shorter light pulse width gets, the wider spectral width becomes.

3.4 Precession under Magnetic Field

As mentioned above, in Voigt configuration, the optic axis is normal to the plane of the QW sample and the optic axis in the growth direction is defined as the z -axis. In addition, a magnetic field is applied transverse to the z -axis of optic axis, namely in the plane of the QW. The Hamiltonian for a magnetic moment M in a uniform magnetic field \mathbf{B} is: $H = -M \cdot B$. For a free electron in the field, the degeneracy of the energy levels for spin-up and spin-down is lifted in a magnetic field. Its magnetic moment is $\vec{\mu} = -g\mu_B \vec{S}$, where, $\mu_B = e\hbar/2m_e \sim 5.788 \times 10^{-5}$ eV/T ~ 14 GHz/T is the Bohr magneton; a vector \vec{S} is the spin moment; g is the g-factor (gyromagnetic ratio), which is ~ 2.002 for free electrons in vacuum. However, it is much smaller for the confined electrons in the QWs due to the modified band energy and spin-orbit energy. In this analysis, the interaction Hamiltonian only includes the energy of an electron magnetic moment in an external field and neglects the additional spin interactions such as the exchange or hyperfine couplings. If the orbital degrees of freedom are left out and the Zeeman Hamiltonian of the energy associated with electron's spin as a magnetic dipole moment in the magnetic field will be:

$$H_\mu = -\vec{\mu} \cdot \vec{B} = H_s = \frac{g\mu_B}{\hbar} \vec{S} \cdot \vec{B} = \frac{g\mu_B}{\hbar} BS_x, \quad \text{Eq. 3-7}$$

The spin magnetic moment is in its lowest energy state when it points along the applied external field. For the conduction band, the electrons are not affected by the effects of

spin-orbit coupling. Therefore, the conduction band electron spin vectors are aligned parallel or antiparallel to the magnetic field lightly, as a result of the Zeeman effects.

In this dissertation, we always consider a magnetic field applied along the x axis as an illustration. Besides, we have taken \vec{z} as the direction of light propagation direction. Thus, the energy eigenstates of the electrons are defined by the magnetic field, which is perpendicular to the optic axis z . Besides, the eigenstates of S_z are $|\uparrow\rangle$ and $|\downarrow\rangle$ with eigenvalues of $+\hbar/2$ and $-\hbar/2$ with angular momentum, respectively. These are also the eigenstates of H_s , with energy eigenvalues of $+(\frac{1}{2})g\mu_B B_x$ and $-(\frac{1}{2})g\mu_B B_x$, respectively, split by the Zeeman energy, as shown in the **Figure 3-9** (a). Spins are stationary when spin states are parallel to B_x . While spin states are perpendicular to B_x , like in Voigt configuration, the eigenstates of S_z and S_y evolve with the precession frequency about magnetic field in time, as displayed in the **Figure 3-9** (b). A state at time origin, $t = 0$, with spin-up $|\uparrow\rangle_z$ along the z -axis can thus be represented as a superposition of $|\uparrow\rangle_x$ and $|\downarrow\rangle_x$:

$$|\Psi(0)\rangle = |+S_z\rangle = \frac{1}{\sqrt{2}}(|+S_x\rangle + |-S_x\rangle) \quad \text{Eq. 3-8}$$

Besides, the time evolution is given by:

$$\begin{aligned} |\Psi(t)\rangle &= \exp(-i\hat{H}_s t / \hbar) |+S_z\rangle \\ &= \frac{1}{\sqrt{2}} \left[\exp\left(-\frac{1}{2}ig\mu_B B t / \hbar\right) |+S_x\rangle + \exp\left(+\frac{1}{2}ig\mu_B B t / \hbar\right) |-S_x\rangle \right] \end{aligned} \quad \text{Eq. 3-9}$$

Then, the expectation value for spin along the z -axis is:

$$\langle \hat{S}_z \rangle = \langle \Psi(t) | \hat{S}_z | \Psi(t) \rangle = \frac{1}{2} \cos(g\mu_B B^* t / \hbar) \quad \text{Eq. 3-10}$$

The precession of the spins is revealed for z-component as it is usually well-described by an exponentially decaying cosine. Similarly, along the y-axis is:

$$\langle \hat{S}_y \rangle = \langle \Psi(t) | \hat{S}_y | \Psi(t) \rangle = \frac{1}{2} \sin(g\mu_B B^* t / \hbar) \quad \text{Eq. 3-11}$$

where, the angular spin precession frequency is $\omega_L = (g\mu_B/\hbar)B_x$.

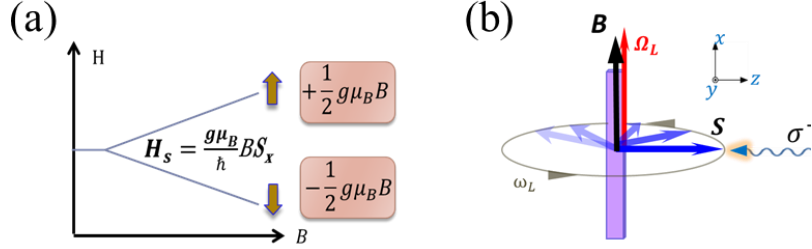


Figure 3-9: (a) Zeeman effect in the non-magnetic QW under external magnetic field. Electron energy in the conduction band versus the magnetic field (B_x); (b) The spin vector is precessing over time about B_x .

The hole-spins do not precess because of a heavy-hole effective g-factor of zero resulting from that the heavy and light hole states are split in our sample. What is more, the growth direction of a SQW becomes a preferred quantization axis for heavy-hole spins due to the quantum confinement of hetero-structure. This results in the heavy-hole spins being constrained to growth axis of the QW [30].

3.5 Experimental Fundamental Setup

The overview of the experimental setup is shown in **Figure 3-10**. The effects of phonons should be frozen out for lengthening the lifetime of spins and studying spin dynamics readily, or else it would accelerate the spin decoherence and broaden optical transitions. To achieve this, we have used the cryostat to cool down sample temperatures

near 10 K. Our cryostat is equipped with a liquid-Helium cooled system with double magnets (EMD-6LS) that can be used up to 800 mT around.

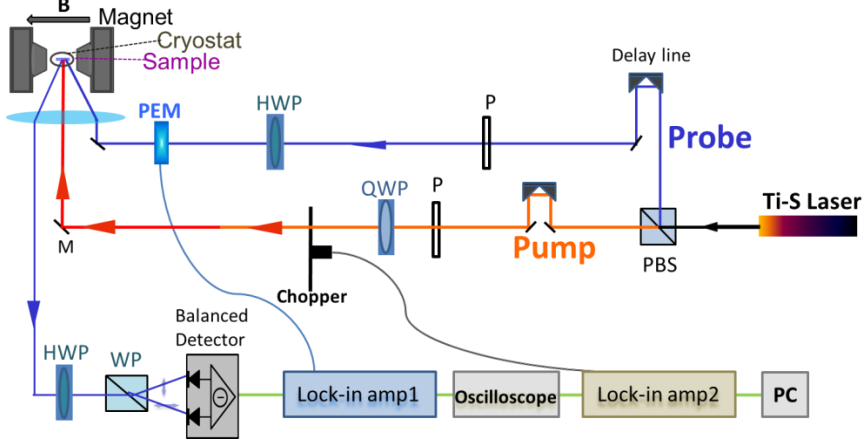


Figure 3-10: A schematic of a time-resolved Kerr rotation setup. PBS refers to polarized beam splitter, P refers to polarizer and M refers to mirror. Other detailed illustrations are described in the text.

As the schematic described, the magnetic field is applied perpendicular to the direction of the optically injected spins for the Voigt geometry case. A convex lens with a focal distance of 15 cm is used for focusing laser beams to overlapping $\sim 100 \mu\text{m}$ diameter spots on the sample. In fact, the probe pulse focused on the sample has a typically small beam diameter of $30 \mu\text{m}$, while the pump (or control, in the next chapter) pulse has a focused beam diameter of roughly $100 \mu\text{m}$. The control of electron spins is highly dependent on the intensity of the excitation pulse. Therefore, the probe spot size must be significantly smaller than the pump in order to interact with as uniform an intensity profile as possible. Based on a reported diffusion constant of the negative trions $D \sim 10 \text{ cm}^2/\text{s}$ at 10 K studied via transient grating experiments [31] and another reported diffusion speed [32], we assume reasonably that the excited carriers seem to be localized

in the probed spot during the RESP decay time (~ 3 ns). Therefore, the carrier diffusion was not taken into account in this study.

At first, the output of the laser is linear. Therefore, the pump path sends the laser through a placed quarter wave plate (QWP) and a chopper before the lens. The QWP is set here for transferring the pulse's helicity from the linearly polarized state after passing through a linear polarizer to circular polarization. Thus, a circularly polarized pump pulse excites spin polarized electrons into the conduction band at time $t = 0$. The linearly polarized probe light monitors the electron spin polarization in the propagation direction of the optical pulse in all our experiments. Then, the computer controlled delay line alters the length of the optical path of the probe pulse precisely by retro-reflecting from a mechanical delay stage, thus providing precise control of the relative arrival time (as long as 3.3 ns, the maximum range of the stage) of the probe pulse with respect to the pump pulse while still maintaining the same beam path. Besides, this stage has a minimum step size of 1 μm , which corresponds to a delay time step size of 20/3 fs. Thus, spin dynamics could be studied by sweeping the delay time between the pump and the probe. At a later time, $t = \Delta t$, the linearly polarized probe pulse arrives at the sample surface and rotates its polarization axis by an angle, Θ_K , from the reflection of sample, proportional to the component of the spin along the pulse propagation direction.

Moreover, during the pulses path, the variable ND (neutral density) filters with the ideal wavelength dependence tune the power of the passed pulses. Through these filters, the constituent wavelength components of the laser pulses are attenuated proportionately. The intensity of the pulses is measured at a particular wavelength by a

photo-detector. In this dissertation, a typical excitation intensity of the probe light is ~ 0.5 mW. Moreover, the pulse power for pump is in the range of $1 \sim 15$ mW.

It is necessary to achieve a large signal to noise ratio, since the change for probe in reflection and over time evolution of RESP can be much smaller than the fluctuation of the probe laser intensity. Hence, lock-in detection techniques must be used in this work. For the most experiments carried out in this dissertation, a cascaded double lock-in amplification technique is employed. The intensity of the pump beam is modulated with a mechanical chopper (STANFORD RESEARCH SYSTEMS, INC; MODEL SR540 CHOPPER CONTROLLER) at a low frequency (120 Hz). The probe pulse is modulated at a high frequency (100 kHz), when passing a Photo-elastic Modulator (PEM; HINDS INSTRUMENTS, I/CF50, 50 kHz, 170 nm ~ 1 μm) after passing through a half wave plate (HWP) with 22.5° and before it is incident upon the sample. After reflecting off from the sample, the probe beam is set to pass through a pinhole to reduce pump scattering. And another HWP is used to rotate the linear polarization, such that a Wollaston prism (WP) splits the probe pulse into two linearly polarized light pulses orthogonal to each other with equal intensity. The two orthogonal beams are then focused onto two photo diodes on the balanced detector (New Focus, Mode 2307) which measures the intensity of the beams. First, the output difference signal is sent to a lock-in amplifier (Stanford Research Systems, Model SR844) being referenced to the double frequency of PEM with a sensitivity of 30 mV or 100 μV , a slope filter of 6 or 12 db/Octave and a time constant of 1 ms. The “Fast X” output of this lock-in is sent to a second lock-in amplifier (Signal Recovery, Model 7265) with the reference frequency of chopper and a time constant of 500 ms after passing an oscilloscope. The first lock-in

amplifier isolates the signal due to probe pulse. The second lock-in amplifier further isolates the signal due to pump pulse and amplifies the signals generated by spin-injection only and input into the computer. The change of the probe polarization is detected as a small intensity difference between the two diodes. This small difference is measured by subtracting the two generated currents of the photodiodes.

In this chapter, the transient pump-probe experiments were mainly introduced. The laser systems and exciton transitions were also discussed for the experiments. Furthermore, the magnetic and cryogenic system used was briefly described. A third control pulse and tilted experimental setups are described in Chapter 4 and 5, respectively.

3.6 References

- [1] X. M. Lu. Study on Growth and Scaling Properties of InAlAs/AlGaAs Quantum Dots[D]: Hokkaido University; 2013.
- [2] G. Finkelstein, V. Umansky, I. Bar-Joseph, V. Ciulin, S. Haacke, J. D. Ganiere, et al. Charged exciton dynamics in GaAs quantum wells[J]. Phys. Rev. B 1998; **58**: 12637-12640.
- [3] M. Munsch, R. Schlich. The Rodriguez Triple Junction (Indian-Ocean) - Structure and Evolution for the Past One Million Years[J]. Mar Geophys Res 1989; **11**: 1-14.
- [4] V. K. Kalevich, E. L. Ivchenko, A. Y. Shiryaev, M. M. Afanasiev, A. Y. Egorov, M. Ikezawa, et al. The sign of electron g-factor in GaAs_{1-x}N_x measured by using the Hanle effect[J]. Semiconductor Science and Technology 2008; **23**: 114008.
- [5] G. L. Oppo, S. M. Barnett, E. Riis, M. Wilkinson. Quantum Dynamics of Simple Systems[B]. Taylor & Francis; 1997.
- [6] E. Burstein, C. Weisbuch, N. A. T. O. S. A. Division. Confined Electrons and Photons: New Physics and Applications[B]. Springer; 1995.
- [7] A. Miller, K. R. Welford, B. Daino. Nonlinear Optical Materials and Devices for Applications in Information Technology[B]. Springer; 1995.
- [8] M. M. Glazov. Coherent spin dynamics of electrons and excitons in nanostructures (a review)[J]. Phys. Solid State 2012; **54**: 1-27.
- [9] P. A. Dowben, N. Wu, C. Binek. When measured spin polarization is not spin polarization[J]. Journal of Physics-Condensed Matter 2011; **23**: 171001.
- [10] M. I. Dyakonov. Spin Physics in Semiconductors[B]. Berlin: Springer; 2008.
- [11] W. H. Lau, M. E. Flatte. Tunability of electron spin coherence in III-V quantum wells[J]. Journal of Applied Physics 2002; **91**: 8682-8684.
- [12] D. D. Awschalom, D. Loss, N. Samarth. Semiconductor Spintronics and Quantum Computation[B]. Berlin: Springer; 2002.
- [13] E. A. Zhukov, D. R. Yakovlev, M. M. Glazov, E. L. Ivchenko, G. Karczewski, et al. Spin coherence of a two-dimensional electron gas induced by resonant

- excitation of trions and excitons in CdTe/(Cd,Mg)Te quantum wells[J]. Phys. Rev. B 2007; **76**: 205310.
- [14] G. V. Astakhov, V. P. Kochereshko, D. R. Yakovlev, W. Ossau, J. Nurnberger, W. Faschinger, et al. Optical method for the determination of carrier density in modulation-doped quantum wells[J]. Phys. Rev. B 2002; **65**: 115310.
- [15] T. A. Kennedy, A. Shabaev, M. Scheibner, A. L. Efros, A. S. Bracker, D. Gammon. Optical initialization and dynamics of spin in a remotely doped quantum well[J]. Phys. Rev. B 2006; **73**: 045307.
- [16] A. Greilich, R. Oulton, E. A. Zhukov, I. A. Yugova, D. R. Yakovlev, M. Bayer, et al. Optical control of spin coherence in singly charged (In,Ga)As/GaAs quantum dots[J]. Phys. Rev. Lett. 2006; **96**: 227401.
- [17] E. A. Zhukov, D. R. Yakovlev, M. Bayer, G. Karezewski, T. Wojtowicz, J. Kossut. Spin coherence of two-dimensional electron gas in CdTe/(Cd,Mg)Te quantum wells[J]. Physica Status Solidi B-Basic Solid State Physics 2006; **243**: 878-881.
- [18] S. O'Leary, H. Wang, J. P. Prineas. Coherent Zeeman resonance from electron spin coherence in a mixed-type GaAs/AlAs quantum well[J]. Optics Letters 2007; **32**: 569-571.
- [19] M. A. Lampert. Mobile and Immobile Effective-Mass-Particle Complexes in Nonmetallic Solids[J]. Phys. Rev. Lett. 1958; **1**: 450-453.
- [20] K. Kheng, R. T. Cox, Y. M. Daubigne, F. Bassani, K. Saminadayar, S. Tatarenko. Observation of Negatively Charged Excitons X- in Semiconductor Quantum-Wells[J]. Phys. Rev. Lett. 1993; **71**: 1752-1755.
- [21] G. Finkelstein, H. Shtrikman, I. BarJoseph. Optical spectroscopy of neutral and charged excitons in GaAs/AlGaAs quantum wells in high magnetic fields[J]. Surface Science 1996; **361**: 357-362.
- [22] G. V. Astakhov, D. R. Yakovlev, V. P. Kochereshko, W. Ossau, J. Nurnberger, W. Faschinger, et al. Charged excitons in ZnSe-based quantum wells[J]. Phys. Rev. B 1999; **60**: R8485-R8488.
- [23] R. A. Sergeev, R. A. Suris. Ground-state energy of X- and X+ trions in a two-dimensional quantum well at an arbitrary mass ratio[J]. Physics of the Solid State 2001; **43**: 746-751.

- [24] R. A. Sergeev, R. A. Suris, G. V. Astakhov, W. Ossau, D. R. Yakovlev. Universal estimation of X- trion binding energy in semiconductor quantum wells[J]. European Physical Journal B 2005; **47**: 541-547.
- [25] H. Haug, A. P. Jauho. Quantum Kinetics in Transport and Optics of Semiconductors[B]. Springer; 2010.
- [26] C. F. Klingshirn. Semiconductor Optics[B]. Springer; 2012.
- [27] M. Gloeckler, A. L. Fahrenbruch, J. R. Sites. Numerical modeling of CIGS and CdTe solar cells: setting the baseline. Photovoltaic Energy Conversion: Proceedings of 3rd World Conference. 2003. p. 491-494.
- [28] R. I. Dzhioev, B. P. Zakharchenya, V. L. Korenev, P. E. Pak, D. A. Vinokurov, O. V. Kovalenkov, et al. Optical orientation of donor-bound excitons in nanosized InP/InGaP islands[J]. Physics of the Solid State 1998; **40**: 1587-1593.
- [29] V. Ciulin, P. Kossacki, J. D. Ganiere, S. Haacke, B. Deveaud, A. Moradi, et al. Radiative lifetime of negative trions in GaAs and CdTe quantum wells[J]. Physica Status Solidi a-Applied Research 2000; **178**: 495-499.
- [30] S. A. Crooker, D. D. Awschalom, J. J. Baumberg, F. Flack, N. Samarth. Optical spin resonance and transverse spin relaxation in magnetic semiconductor quantum wells[J]. Phys. Rev. B 1997; **56**: 7574-7588.
- [31] M. T. Portella-Oberli, V. Ciulin, S. Haacke, J. D. Ganiere, P. Kossacki, M. Kutrowski, et al. Diffusion, localization, and dephasing of trions and excitons in CdTe quantum wells[J]. Phys. Rev. B 2002; **66**: 155305.
- [32] F. Pulizzi, D. Sanvitto, P. C. M. Christianen, A. J. Shields, S. N. Holmes, M. Y. Simmons, et al. Optical imaging of trion diffusion and drift in GaAs quantum wells[J]. Phys. Rev. B 2003; **68**: 205304.

CHAPTER 4

INITIAL PHASE SHIFT (IPS) OF RESP

4.1 Introduction

Importantly, the generation of RESP by the resonant absorbing of the circularly polarized pulse has been elementary proved to be decided by the instantaneous formation of trions and exciton states in the semiconductor nanostructures [1]. In addition, the excited state of negatively charged trion in a singly charged QW is one of the most useful states for quantum optical RESP studies. This state can provide many prototypical quantum optical systems, such as two-level systems based on the underground resident electron ensemble useful for the coherent control applications. What is more, the resident electron spin ensemble is of great significance as mentioned before. Therefore, a tremendous amount of research effort has been put forth to better understand the interplay among resident electrons, trions [2-5], relative excitons and with their environments, such as tunable lasers [6], QW barriers [7] and nuclear spins [8], as well as to have a correct scenario of the exciton evolution that allows for better controlling the electron spins [1, 9]. However, it is still difficult to capture the exact transient snapshots of ultrafast carrier spin transforming process during the RESP generation. In addition, the many-body effects that result from electron-electron interactions, exciton-exciton interactions make this study more complicated. Therefore, the theoretical status and the physical

interpretation of all initial phases in the RESP transient signals have not been fully established.

In our study, the careful analysis of the TRKR signals as compared to the theoretical fittings around time origin ($t = 0$) reveals an appealing phenomenon: the negative IPS by which one looks "backward" in time-domain towards zero delay as shown later. Although the positive and zero IPSs have been reported in CdTe QWs [10]. So far, we observed the negative IPS in a CdTe SQW. In this chapter, the IPS in a temporal evolution of RESP was wholly investigated. The details of trions, excitons and RESP formation analysis, ensemble electrons spin precession, as well as excitation intensity, external magnetic field and photon energy dependences of IPS are also presented in the below.

4.1 IPS Phenomenon

A typical TRKR signal (red solid line) and the fitting curve (green solid line) of its RESP precession in a CdTe QW sample at $B_x = 146$ mT excited by a σ^- pulse with a low power $P_{pump} = 1$ mW is shown in **Figure 4-1**. The negative trions are excited resonantly by the narrower spectral pump pulse compared to the trion spectrum. Ruling out of a small component of the natural exciton and the trion with a short lifetime, over the delay time trace of $t = 500 \sim 3000$ ps, the typical experimental TRKR signal mainly reflecting RESP dynamical precession alone can be fitted generally by the following single exponential function:

$$S(t) = A^e \exp\left(-\frac{t}{\tau_s^e}\right) \cos(\omega_L t + \Phi) \quad \text{Eq. 4-1}$$

where the coefficients A^e is the amplitude of RESP, τ_s^e is the corresponding transverse spin-relaxation time, ω_L is the electron Larmor frequency; ϕ is the IPS of RESP precession, respectively. As shown in **Figure 4-1**, the extend curve of extrapolating back to zero time delay for the fitting of this TRKR signal can show that the time delay of RESP plays out a little retarded temporal shift ϕ/ω_L to the time origin as indicated by the inset of **Figure 4-1**. It is self-evident that the initial phase ϕ of the residual electron polarization oscillation emits a slightly negative IPS against the time origin. In this way, the corresponding IPS and amplitude have been acquired and shown for all the following results in this dissertation.

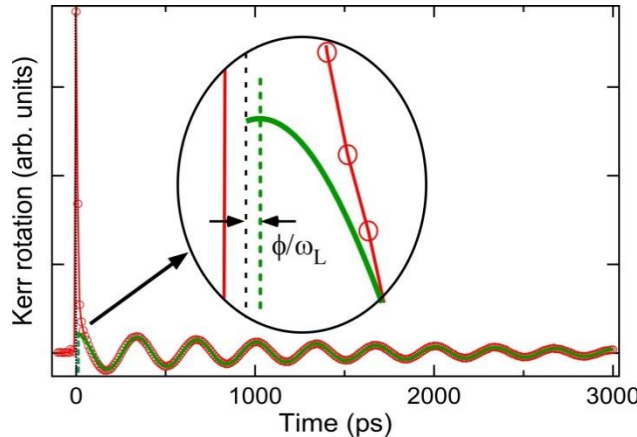


Figure 4-1: A typical TRKR signal ($B_x = 146$ mT and 10 K) and the fitting of RESP precession component (green solid line). Inset: the negative IPS ϕ of RESP is shown by a backward temporal shift ϕ/ω_L ($P_{pump} = 1$ mW).

The spins of double electrons in a trion are in a singlet state and therefore, do not precess under the magnetic field as the resident electrons do, due to the splitting energy as explained in Chapter 2. The returning electrons after the trion recombination lead to different spin orientations, which could induce a phase difference of a TRKR signal, as Zhukov et. al demonstrated [11]. Based on the previous workers' experience, a schematic

of the common RESP dynamics is depicted in **Figure 4-2**. The figure is depicted under the condition that the trion recombination time is great smaller than the precession period: $\tau_r^T < \omega_L$. In the presence of background resident electrons, before optical excitation (stage I), there is not a little RESP. Moreover, the individual electron spins rotate around the applied magnetic field \mathbf{B}_x . At the time origin ($t = 0$, stage II), optical excitation (σ^- excitation in the **Figure 4-2**) at the trion resonance can generate an e-hh pair ($\uparrow\downarrow$) selectively, which captures one electron with an opposite spin (\downarrow) from the resident electron ensemble and forms a negative trion ($\downarrow\uparrow\downarrow$). At this moment, the resident electron ensemble loses the spin balance and a nonzero net RESP comes out (stage III). The return of electron after trion recombination can change RESP. Neglecting the spin relaxation of the hole in the trion here, an electron with the same spin (\downarrow) as that captured at $t = 0$ is returned to the resident electron ensemble after the original trion recombination. The final spin state of resident electrons with induced polarization is shown (stage IV). The microscopic picture of the above RESP generation with a heavy hole relaxation behavior is given by Kennedy et. al [12].

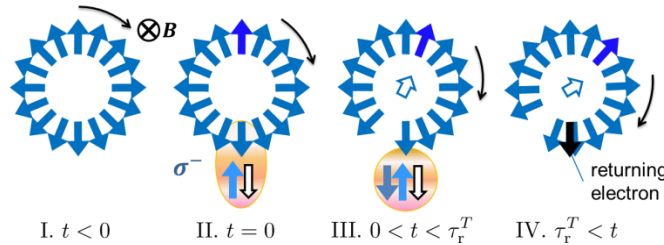


Figure 4-2: Schematic of the RESP dynamics, where the interplay between resident electrons and optically excited negative trion is illustrated. (I) The electron spins with the non-polarized initial state are precessing around the magnetic field \mathbf{B}_x . (II) The e-hh ($+1/2, -3/2$) pair generated by a σ^- excitation captures an electron with $-1/2$ to form a negative trion and makes the net polarization in the resident electron ensemble. (III) Trion does not precess in the magnetic field, but its hole spin may flip during the trion recombination time (τ_r^T). (IV) The electron spin left behind by the trion recombination returns back to the ensemble of resident electrons. Moreover, it

changes the net RESP and the initial phase.

The past study reported a positive IPS in a TRKR signal of a CdTe SQW [11]. However, in this dissertation, the negative IPS always comes out as shown in **Figure 4-1**. The critical point here is that the trions spin dynamics play crucial roles on the sign of IPS. In addition, the IPS could also be induced by the conversion of natural excitons. Further detailed analysis and interpretation will be stated in the following sections.

4.2 Theoretical IPS of RESP from Trion Dynamics

Before going to the experimental results, the possible trion dynamics and the resident electron ensemble spin coherence evolutions modulated by the theoretical equations will be itemized in the section. The ionization of trions into excitons is not considered for the time being.

Assume a σ^+ polarized pulse at $t = 0$ with a spin -1/2 electron will generate a spin -3/2 trion ($T_{\downarrow}, \uparrow\downarrow\downarrow$) with a concentration $N^{T_{\uparrow}}(0)$, leaving behind a spin +1/2 electron in the resident electrons community. The densities of spin -3/2 trions ($T_{\downarrow}, \uparrow\downarrow\downarrow$) and spin +3/2 trions ($T_{\uparrow}, \uparrow\downarrow\uparrow\uparrow$) are $N^{T_{\downarrow}}(t)$, $N^{T_{\uparrow}}(t)$, which are just the densities of trions polarized parallel ($m = -3/2$) and antiparallel ($m = +3/2$) to the light propagation direction. Here, their holes spin dependent relaxation time and the trion recombination time are written as τ_s^T , τ_r^T . The total trion population density $N^T(t)$ evolves with trion recombination as:

$$\begin{aligned} N^T(t) &= N^{T_{\uparrow}}(t) + N^{T_{\downarrow}}(t) \\ &= N^T(0)\exp(-t/\tau_r^T) \\ &= 2N^0\exp(-t/\tau_r^T) \end{aligned} \quad \text{Eq. 4-2}$$

Sometimes, the degree of trion polarization is shown like this:

$$P(t) = [N^{T_{\downarrow}}(t) - N^{T_{\uparrow}}(t)] / [N^{T_{\downarrow}}(t) + N^{T_{\uparrow}}(t)] \quad \text{Eq. 4-3}$$

In this way, the spin polarization is equal to 100% (-100%) at the moment of σ^- (σ^+) photo-excitation, because this system is non-polarization before any optical excitation.

Nevertheless, the spin polarization is a badly ambiguous scientific idiom and as such, is rarely well defined. A given experimental methodology may allow us to quantify a spin polarization but only in its particular context. In general, the spin polarization is defined as the half of the density difference between spin + and - carriers.

In this dissertation, since we mainly calculate the electron spin polarization, the trion polarization is denoted by the trion spin polarized population (half the density difference between the spin T_{\uparrow} (+3/2) and T_{\downarrow} (-3/2) trions). Here, the trion polarization sign is decided by heavy hole spins. Therefore, the trion spin polarization is

$$S^T(t) = S^{T_{\downarrow}}(t) + S^{T_{\uparrow}}(t) \equiv (N^{T_{\downarrow}}(t) - N^{T_{\uparrow}}(t)) / 2 \text{ as a whole. Additionally, the corresponding}$$

polarization: $S^{T_{\downarrow}}(t) = N^{T_{\downarrow}}(t) / 2$, $S^{T_{\uparrow}}(t) = -N^{T_{\uparrow}}(t) / 2$. At the moment of a σ^- photo-

excitation, the T_{\downarrow} trion density is supposed as $2N_0$, then $S^T(0) = (N^{T_{\downarrow}}(0) - 0) / 2 = N_0$, due

to its non-polarization before optical excitation.

Since the ground level of the electrons are occupied by spin \downarrow and spin \uparrow , assuming that resident electron density of the electrons community is n^e . Moreover, the resident electrons \uparrow spins and \downarrow spins are considered to exist by $n^e / 2$. When T_{\downarrow} is formed by the σ^- optical excitation, the residual electrons \downarrow spins are reduced by $N^{T_{\downarrow}}(0)$ ($2N_0$).

Then the firstly polarized RESP density of the remaining electron ensemble spins is formed by $\{n^e / 2 - (n^e / 2 - 2N_0)\} / 2 = N_0$. Because the trion density $2N_0$ cannot exceed $n^e / 2$, this RESP maximum is $n^e / 4$. For the anti-symmetric carriers, the polarization of

one of the spin -3/2 trion ($T_{\downarrow\uparrow\downarrow\downarrow}$) and spin +3/2 trion ($T_{\uparrow\uparrow\downarrow\downarrow}$) should include a minus sign with respect to the other in the front of density. In this case, the initial conditions of the spin evolutions are shown as below:

$$\begin{aligned} S^e(t=0) &= (0, 0, N_0) \\ S^{T_{\downarrow}}(t=0) &= (0, 0, N_0) \\ S^{T_{\uparrow}}(t=0) &= (0, 0, 0) \end{aligned} \quad \text{Eq. 4-4}$$

As mentioned before, the resident electrons precess with the Larmor frequency $\omega_L = (\omega_L, 0, 0)$ on the y - z plane around x axis magnetic field, so S_x^e is ignored here. Then the rate equations of RESP under the external magnetic field are shown by **Eq. 4-5** and **Eq. 4-6**:

$$\frac{dS_y^e}{dt} = -\omega_L S_z^e - \frac{S_y^e}{\tau_s^e} \quad \text{Eq. 4-5}$$

$$\frac{dS_z^e}{dt} = \omega_L S_y^e - \frac{S_z^e}{\tau_s^e} + \frac{-S^T}{\tau_r^T} \quad \text{Eq. 4-6}$$

While, learned from Section 4.1 above (on page 80), the coherent RESP is modified by the hole spin relaxation of trion and the trion recombination. Although the details of the trion dynamics have been revealed acceptably in the previous studies [11, 13], the dynamics around time origin is still unclear. Therefore, there would be several kinds of trion dynamical models need to be considered soon afterwards in this dissertation.

4.2.1 Model A1

For the first model, it is supposed that the holes spin relaxation time is negligible due to that the most of the spin relaxation mechanisms should be suppressed [14] in some particular QWs and a long spin coherence time for holes can be conceived except the recombination consuming, that is $\tau_s^T \infty, 1/\tau_s^T = 0$. Then, if there are not any other

relaxations of hole-spin inversions ($1/\tau_{sh}^T = 0$), or any decomposition ($1/\tau_{sd}^T = 0$) for trion complex, the trion decay rate will be simplified into the recombination rate:

$\frac{1}{\tau^T} = \frac{1}{\tau_r^T} + \frac{1}{\tau_{sh}^T} + \frac{1}{\tau_{sd}^T} \approx \frac{1}{\tau_r^T}$ in this system. The integral formation dynamical process of RESP would only be composed of P1 and P2 processes, as shown in **Figure 4-3**.

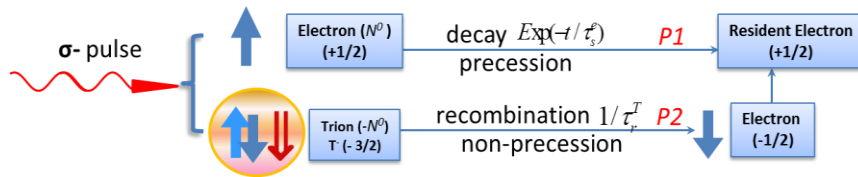


Figure 4-3: RESP building up from trions' formation and recombination. The detailed analysis is referred in the text.

The rate equation about trions evolution is displayed in **Eq. 4-7**,

$$\frac{dS_z^{T_\downarrow}}{dt} = -\frac{S_z^{T_\downarrow}}{\tau_r^T} \quad \text{Eq. 4-7}$$

Then, its solution $S_z^{T_\downarrow}(t) = S_z^{T_\downarrow}(0) * \exp(-\frac{t}{\tau_r^T}) = N_0 \exp(-\frac{t}{\tau_r^T})$ is put into the calculations of **Eq. 4-5** and **Eq. 4-6**. The integrated results for RESP are then acquired in **Eq. 4-8**, so the total spin polarization of all carriers $S(t)$ is calculated by **Eq. 4-9**:

$$\begin{aligned} S_z^e(t) &= S_{p1}^e(t) + S_{p2}^e(t) \\ &= N_0 \left[\left(1 - \frac{1}{1 + (\omega_L \tau_r^T)^2} \right) \cos(\omega_L t) \right. \\ &\quad \left. + \frac{-\omega_L \tau_r^T}{1 + (\omega_L \tau_r^T)^2} \sin(\omega_L t) \right] \exp(-t / \tau_s^e) \\ &\quad + N_0 \frac{1}{1 + (\omega_L \tau_r^T)^2} \exp(-\frac{t}{\tau_r^T}) \end{aligned} \quad \text{Eq. 4-8}$$

$$S(t) = S_z^e(t) + S_z^{T_\downarrow}(t) + S_z^{T_\uparrow}(t) \quad \text{Eq. 4-9}$$

From **Eq. 4-8**, the IPS Φ and the amplitude P are obtained as following:

$$\Phi_{\text{AI}} = \arcsin \frac{1}{\omega_L \tau_r^T} \quad \text{Eq. 4-10}$$

$$P_{\text{AI}} = N_0 \sqrt{\left(1 + \frac{-1}{1 + (\omega_L \tau_r^T)^2}\right)^2 + \left(\frac{-\omega_L \tau_r^T}{1 + (\omega_L \tau_r^T)^2}\right)^2} \quad \text{Eq. 4-11}$$

According to **Eq. 4-10**, the dependences of calculated IPSs on Larmor frequency ($\omega_L = 0 \sim 0.1 \text{ rad/ps}$) and recombination time ($\tau_r^T = 10 \sim 85 \text{ ps}$) are shown in **Figure 4-4**, respectively. Obviously, this system must generate positive IPSs ($0 \sim 1.5$ radian) under any condition.

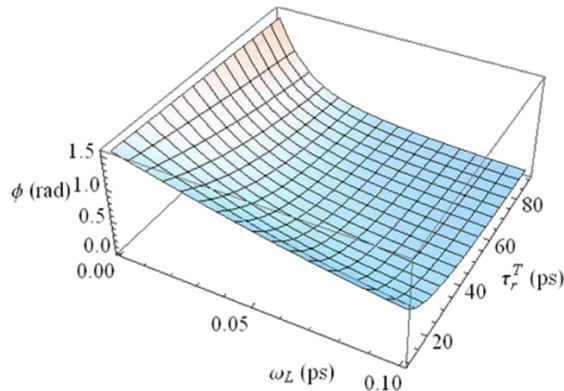


Figure 4-4: The dependence of calculated IPSs on Larmor frequency $\omega_L = 0 \sim 0.1 \text{ rad/ps}$ and recombination time $\tau_r^T = 10 \sim 85 \text{ ps}$ for Model AI system.

4.2.2 Model AII

Based on the usual trion dynamics with the rather obvious hole spin relaxation rate $1/\tau_s^T$ and the same trion recombination rate $1/\tau_r^T$, then the total lifetime of trion τ^T

can be indicated by this correlation: $\frac{1}{\tau_s^T} + \frac{1}{\tau_r^T} = \frac{1}{\tau^T}$, as described in the Section 4.1 above.

Its schema for RESP generation is illustrated in **Figure 4-5**, which is depicted for a σ^- polarized and weak intensity excitation condition. The model contains three processes (P1; P2; P3) to generate the RESP: an e-hh pair ($\uparrow\downarrow$) is created via a photon absorption at $t = 0$ and captures $-1/2$ (\downarrow) electron from the resident electron reservoir to form a $-3/2$ trion ($T_{\downarrow}; \uparrow\downarrow\downarrow$). This capturing is equivalent to leaving behind $+1/2$ (\uparrow) electron in the resident electron reservoir. Therefore, the first partition of RESP can be generated as stated before. This process of RESP generation is P1 in **Figure 4-5**. The process P2 is through T_{\downarrow} recombination. P3 is through T_{\uparrow} recombination after the hole spin-flip from T_{\downarrow} and therefore the spin of the returning electron is opposite to that in P2.

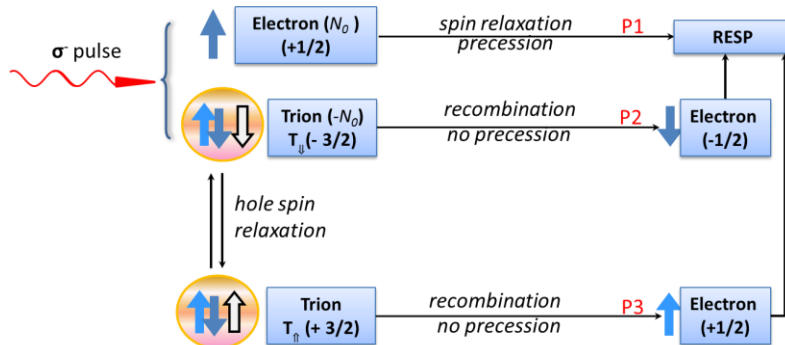


Figure 4-5: Schematic AII of modeling RESP generation.

Considering the above dynamics, the rate equations will be:

$$\begin{aligned}\frac{dS^{T_{\downarrow}}}{dt} &= -\frac{S^{T_{\downarrow}}}{\tau_r^T} - \frac{S^{T_{\downarrow}}}{2\tau_s^T} + \frac{(-S^{T_{\uparrow}})}{2\tau_s^T} \\ \frac{d(-S^{T_{\uparrow}})}{dt} &= -\frac{(-S^{T_{\uparrow}})}{\tau_r^T} + \frac{S^{T_{\downarrow}}}{2\tau_s^T} - \frac{(-S^{T_{\uparrow}})}{2\tau_s^T}\end{aligned}\quad \text{Eq. 4-12}$$

Assuming the initial conditions in **Eq. 4-4**, the following analytical solutions displayed in **Eq. 4-13** can be deduced from **Eq. 4-12**:

$$S^{T_{\downarrow}} = \frac{1}{2} N_0 \left[\exp\left(-\frac{t}{\tau_r^T}\right) + \exp\left(-\frac{t}{\tau_r^T} - \frac{t}{\tau_s^T}\right) \right]$$

$$S^{T_{\uparrow}} = \frac{1}{2} N_0 \left[-\exp\left(-\frac{t}{\tau_r^T}\right) + \exp\left(-\frac{t}{\tau_r^T} - \frac{t}{\tau_s^T}\right) \right]$$

Eq. 4-13

Taking **Eq. 4-13** into **Eq. 4-5** and **Eq. 4-6**, the acquired RESP is shown here:

$$S_z^e(t) = S_{p1}^e(t) + S_{p2}^e(t) + S_{p3}^e(t)$$

$$= [A \cos(\omega_L t) + B \sin(\omega_L t)] \exp\left(-\frac{t}{\tau_s^e}\right)$$

$$+ D \exp\left(-\frac{t}{\tau_s^T} - \frac{t}{\tau_r^T}\right)$$

Eq. 4-14

$$A = N_0 \tau_r^T \begin{cases} \tau_r^T (\tau_s^e)^2 + \\ \tau_s^T \tau_s^e (\tau_s^e - 2\tau_r^T) + \\ (\tau_s^T)^2 (\tau_r^T - \tau_s^e +) \end{cases}$$

$$B = -N_0 (\tau_s^T)^2 \tau_r^T (\tau_s^e)^2 \omega_L \begin{cases} (\tau_r^T)^2 (\tau_s^e)^2 + 2\tau_s^T \tau_r^T \tau_s^e (-\tau_r^T + \tau_s^e) + \\ (\tau_s^T)^2 \left\{ (\tau_s^e)^2 + (\tau_r^T)^2 (1 + \omega_L^2 (\tau_s^e)^2) - 2\tau_r^T \tau_s^e \right\} \end{cases}$$

Eq. 4-15

$$D = N_0 \tau_s^T \tau_s^e \begin{cases} \tau_r^T \tau_s^e + \\ \tau_s^T (\tau_s^e - \tau_r^T) \end{cases}$$

$$\begin{cases} (\tau_r^T)^2 (\tau_s^e)^2 + 2\tau_s^T \tau_r^T \tau_s^e (-\tau_r^T + \tau_s^e) + \\ (\tau_s^T)^2 \left\{ (\tau_s^e)^2 + (\tau_r^T)^2 (1 + \omega_L^2 (\tau_s^e)^2) - 2\tau_r^T \tau_s^e \right\} \end{cases}$$

Eq. 4-16

$$D = N_0 \tau_s^T \tau_s^e \begin{cases} \tau_r^T \tau_s^e + \\ \tau_s^T (\tau_s^e - \tau_r^T) \end{cases}$$

$$\begin{cases} (\tau_r^T)^2 (\tau_s^e)^2 + 2\tau_s^T \tau_r^T \tau_s^e (-\tau_r^T + \tau_s^e) + \\ (\tau_s^T)^2 \left\{ (\tau_s^e)^2 + (\tau_r^T)^2 (1 + \omega_L^2 (\tau_s^e)^2) - 2\tau_r^T \tau_s^e \right\} \end{cases}$$

Eq. 4-17

Finally, the IPS ϕ and the RESP amplitude P are obtained as follows:

$$\Phi = \arctan(-B/A) > 0 \quad \text{Eq. 4-18}$$

$$P = \sqrt{A^2 + B^2} \quad \text{Eq. 4-19}$$

By using of **Eq. 4-18**, the Larmor frequency and recombination time dependences for calculated IPSs, under the condition of $\tau_r^T = 0 \sim 110 \text{ ps}$, $\tau_s^T = 0 \sim 100 \text{ ps}$, $\omega = 0.0188 \text{ rad/ps}$, are shown in **Figure 4-6**. These dynamical model also always deduce positive IPS (1 ~ 0 radian), or almost zero IPS on the condition of fast hole spin relaxation time: $\tau_s^T \ll \tau_r^T$. Under this ultimate condition of extremely fast holes spin relaxation, the RESP can rarely be affected by trions' behaviors.

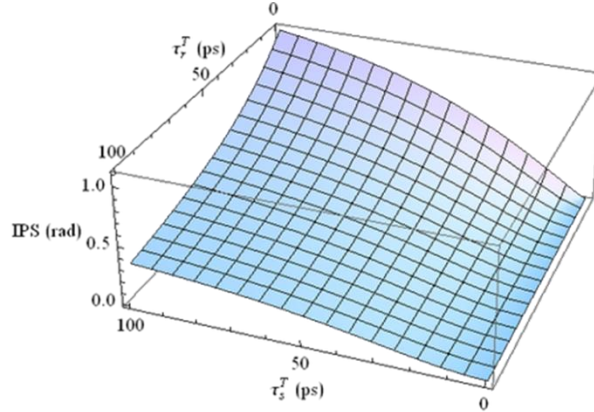


Figure 4-6: The dependences of theoretical IPSs on the relaxation time $\tau_s^T = 0 \sim 100 \text{ ps}$ and the recombination time $\tau_r^T = 0 \sim 110 \text{ ps}$ with the Larmor frequency $\omega_L = 0.0188 \text{ rad/ps}$ for Model AII system.

According to **Eq. 4-18**, the calculated IPSs are positive and have a serial of minimal values at the certain values of Larmor frequencies, as indicated in **Figure 4-7 (a)**, which agrees well with the reported results [11]. Additionally, the RESP amplitude goes up with the increasing frequency deduced in the calculations of **Eq. 4-19** as shown in **Figure 4-7 (b)**.

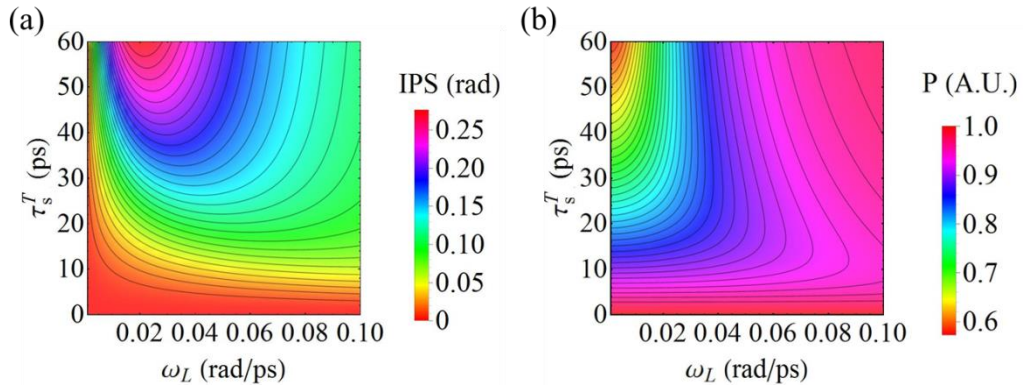


Figure 4-7: Calculated IPSs (a) and RESP amplitudes (b) depending on Larmor frequency for Model AII system under the condition of $\tau_s^T = 0 \sim 60$ ps, $\omega_L = 0.001 \sim 0.10$ rad/ps.

4.2.3 Model AIII

To give significant insight into the IPS mechanism and to analyze our experimental results quantitatively, we put forth another theoretical model for the spin dynamics of RESP, based on the analysis of experimental data and theoretical simulations, as shown in the following **Figure 4-8**, which is depicted for a σ -polarized and weak intensity excitation condition. In **Figure 4-8**, the model AIII likewise contains three processes (P1; P2; P3) to generate the RESP, where the excitation at the trion resonance is assumed in this case and the excitation of the neutral excitons is excluded for the simplicity. Note that the P1 process here is same as that in Model AII, the e-hh pairs ($\uparrow\downarrow$) are created by the absorption of the circularly-polarized photons at $t = 0$ and capture -1/2 (\downarrow) electrons from the resident electron ensemble to form -3/2 trions (T_{\downarrow} ; $\uparrow\downarrow\downarrow$) with a concentration $N_{T_{\downarrow}}(0)$. This capturing is equivalent to leaving behind electrons with +1/2 (\uparrow) with the same concentration in the resident electron ensemble. Therefore, the first partition of RESP can generate. The RESP generation process P2 (P3)

occurs via the recombination of T_{\downarrow} (T_{\uparrow}). The difference here is that P3 becomes large majority in the electrons' return process, to explain the negative IPS. While the electron spin-flip in a trion ground state is forbidden by Pauli's exclusion principle, the unpaired hole can flip its spin. In this system, therefore there is an irreversible hole spin flip performance with the time constant of τ_{sh}^T for the original trions T_{\downarrow} after generation. This hole-spin relaxation process is asymmetric between T_{\downarrow} and T_{\uparrow} . The assumption should be tested by the comparison between the experimental and calculated results. In addition, other hole spin relaxation time can be neglected, due to that most of the spin relaxation mechanisms should be suppressed [14] and a long spin coherence time for holes can be conceived except the recombination consuming. Then we assume that spin-polarized trion populations of T_{\uparrow} and T_{\downarrow} evolve as:

$$S^{T_{\downarrow}} = N_0 e^{-\left(\frac{t}{\tau_r^T} + \frac{t}{\tau_{sh}^T}\right)} \quad \text{Eq. 4-20}$$

$$S^{T_{\uparrow}} = N_0 (e^{-\frac{t}{\tau_r^T} - \frac{t}{\tau_{sh}^T}} - e^{-\frac{t}{\tau_r^T}}) = S^{T_{\downarrow}} - N_0 e^{-\frac{t}{\tau_r^T}} \quad \text{Eq. 4-21}$$

$$S^T(t) = S^{T_{\downarrow}}(t) + S^{T_{\uparrow}}(t) = N_0 (2e^{-\left(\frac{t}{\tau_r^T} + \frac{t}{\tau_{sh}^T}\right)} - e^{-\frac{t}{\tau_r^T}}) \quad \text{Eq. 4-22}$$

where $S^{T_{\downarrow}}$; $S^{T_{\uparrow}}$ is the returning RESP from T_{\downarrow} ; T_{\uparrow} trion recombination via P2(P3).

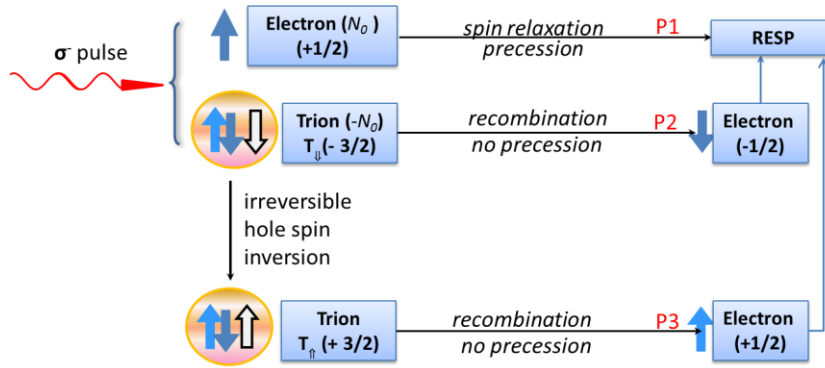


Figure 4-8: Schematic AIII for modeling RESP generation.

The spin polarization of the resident electrons ensemble generated upon trion formation at $t = 0$ will precess around the magnetic field, with the projection in the QW growth direction:

$$S_{p1}^e(t) = N_0 \cos(\omega_L t) \exp\left(-\frac{t}{\tau_s^e}\right) \quad \text{Eq. 4-23}$$

Assuming the above initial conditions, similar to **Eq. 4-5** and **Eq. 4-6**, the RESPs generating process from T_\downarrow and T_\uparrow evolution will be displayed in the following integral equations. The return electrons spin polarization generated by trion T_\downarrow recombination during $/t', t'+dt'/$ is $dS_{p2}^e(t') = (-S^{T_\downarrow}(t')/\tau_r^T)dt'$. The return electrons spin polarization from trion T_\downarrow recombination at t :

$$S_{p2}^e(t) = \int_0^t \frac{-S^{T_\downarrow}(t')}{\tau_r^T} \cos\{\omega_L(t-t')\} \exp\left(-\frac{t-t'}{\tau_s^e}\right) dt' \quad \text{Eq. 4-24}$$

The returning electrons spin polarization generated by trion T_\uparrow recombination during $/t', t'+dt'/$ is $dS_{p3}^e(t') = (-S^{T_\uparrow}(t')/\tau_r^T)dt'$. Then the return electrons spin polarization from trion T_\uparrow recombination at t :

$$S_{p3}^e(t) = \int_0^t \frac{-S^{T\uparrow}(t')}{\tau_r^T} \cos\{\omega_L(t-t')\} \exp(-\frac{t-t'}{\tau_s^e}) dt' \quad \text{Eq. 4-25}$$

The following RESP $S^e(t)$ obtained from solving **Eq. 4-24** and **Eq. 4-25** including the asymmetric hole spin flip is shown here:

$$\begin{aligned} S^e(t) &= N^0 [A \cos(\omega_L t) + B \sin(\omega_L t)] \exp(-\frac{t}{\tau_s^e}) \\ &\quad + C \exp(-\frac{t}{\tau_r^T}) + D \exp(-\frac{t}{\tau_r^T} - \frac{t}{\tau_{sh}^T}) \end{aligned} \quad \text{Eq. 4-26}$$

$$A = N^0 \left[\frac{\omega_L \tau_r^T}{1 + (\omega_L \tau_r^T)^2} - \frac{2\omega_L \tau_r^T (\tau_{sh}^T)^2}{(\tau_r^T + \tau_{sh}^T)^2 + (\omega_L \tau_{sh}^T \tau_r^T)^2} \right] \quad \text{Eq. 4-27}$$

$$B = N^0 \left[1 + \frac{1}{1 + (\omega_L \tau_r^T)^2} - \frac{2\tau_{sh}^T (\tau_r^T + \tau_{sh}^T)}{(\tau_r^T + \tau_{sh}^T)^2 + (\omega_L \tau_{sh}^T \tau_r^T)^2} \right] \quad \text{Eq. 4-28}$$

$$C = -\frac{N^0}{1 + (\tau_r^T \omega_L)^2}; \quad D = \frac{2N^0 \tau_{sh}^T (\tau_r^T + \tau_{sh}^T)}{(\tau_r^T + \tau_{sh}^T)^2 + (\omega_L \tau_{sh}^T \tau_r^T)^2} \quad \text{Eq. 4-29}$$

In the derivation of the coefficients A, B, C, D in **Eq. 4-27**, **Eq. 4-28** and **Eq. 4-29**, we ignored the higher-order correction term of $(1/\tau_s^e)^{n \geq 1}$ and only the zero power term of RESP transverse decay rate has been considered, since the electron spin relaxation time is much longer than the trion's time constants ($\tau_s^e \gg \tau_r^T \succ \tau_{sh}^T$) and plays a negligible role in the results. Finally, the IPS ϕ and the RESP amplitude P are obtained by means of **Eq. 4-18** and **Eq. 4-19**. Then the detailed calculated results will be discussed together with experimental data in Section 4.5 and 4.6.

4.3 Theoretical IPS from Exciton Transformation Dynamics

4.3.1 Model BI

In a lightly n-doped QW, the excitonic transition is still an inevitable interband optical property at low temperatures. Despite the importance of exciton transition on

RESP, little work has been done on the interactions between excitons and RESP in lightly n-doped QWs [15], owing to too many interactions of carriers. Especially excited in the resonant with exciton, there are pretty many electron–hole pairs in the carriers which dominate the spin dynamics. In the previous PL study, the neutral exitons might decay to the negatively charged trions and RESP [16]. Here, we just make a simplified IPS interpretation for neutral exciton resonant transition under the limited conditions.

Before the conversion of excitons to trions, there is a much faster exchange interaction in this CdTe SQW deduced from our experimental TRKR results. Through the experimental analysis, the calculation model BI for the exciton carriers spin dynamics has been put forth here.

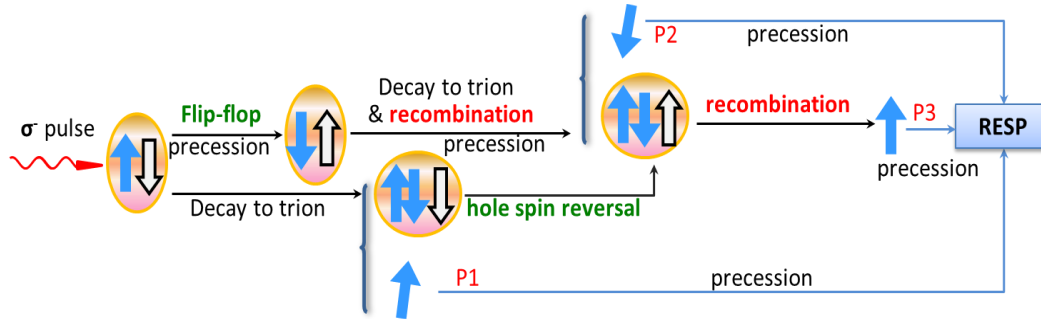


Figure 4-9: Schematic BI of modeling RESP generation based on the neutral excitons conversion. Also the schematic diagram displays the corresponding evolution of excitons based on the TRKR data in **Figure 4-22** later.

After creating the polarized excitons by a circularly polarized pulse, their holes and electrons could lose original spin orientation in a few picoseconds (10^{-12}). In this case, the precession motion and the exchange interaction occur at the same time. The electrons spins splitting in the excitons would be decided by the Zeeman splitting energy and electron-hole exchange energy δ , that is, $\hbar\omega = \sqrt{(g_e\mu_B B)^2 + \delta^2}$. At a low magnetic

field and under the quick exchange behavior, we suppose $\hbar\omega \sim \delta$ for excitons in order to conveniently run the equation available. At the same time, both -1 and +1 excitons can form triions during the transformation time τ_b , as well as contribute to the RESP by adding the spin polarization of spin +1/2 and -1/2 electrons, respectively. The corresponding rate equations by ruling out of the excitations precession in a short time for BI would be like this as shown in **Eq. 4-30**.

$$\begin{aligned}\frac{dS_e^{X_{\downarrow}}}{dt} &= -\frac{S_e^{X_{\downarrow}}}{\tau_s^X} - \frac{S_e^{X_{\downarrow}}}{\tau_r^X} - \frac{S_e^{X_{\downarrow}}}{\tau_b} \\ \frac{dS_h^{X_{\downarrow}}}{dt} &= -\frac{S_h^{X_{\downarrow}}}{\tau_s^X} - \frac{S_h^{X_{\downarrow}}}{\tau_r^X} - \frac{S_h^{X_{\downarrow}}}{\tau_b} \\ \frac{d(-S_e^{X_{\uparrow}})}{dt} &= \frac{S_e^{X_{\downarrow}}}{\tau_s^X} - \frac{(-S_e^{X_{\uparrow}})}{\tau_r^X} - \frac{(-S_e^{X_{\uparrow}})}{\tau_b} \\ \frac{d(-S_h^{X_{\uparrow}})}{dt} &= \frac{S_h^{X_{\downarrow}}}{\tau_s^X} - \frac{(-S_h^{X_{\uparrow}})}{\tau_r^X} - \frac{(-S_h^{X_{\uparrow}})}{\tau_b}\end{aligned}$$

Eq. 4-30

$$\begin{aligned}\frac{dS^{T_{\downarrow}}}{dt} &= -\frac{S^{T_{\downarrow}}}{\tau_r^T} - \frac{S^{T_{\downarrow}}}{\tau_{sh}^T} + \frac{S_h^{X_{\downarrow}}}{\tau_b} \\ \frac{d(-S^{T_{\uparrow}})}{dt} &= -\frac{(-S^{T_{\uparrow}})}{\tau_r^T} + \frac{S^{T_{\downarrow}}}{\tau_{sh}^T} + \frac{S_h^{X_{\uparrow}}}{\tau_b}\end{aligned}$$

$$\begin{aligned}\frac{dS_y^e}{dt} &= -\omega_L S_z^e - \frac{S_y^e}{\tau_S^e} \\ \frac{dS_z^e}{dt} &= \omega_L S_y^e - \frac{S_z^e}{\tau_S^e} + \frac{-S^{T_{\downarrow}}}{\tau_r^T} + \frac{-S^{T_{\uparrow}}}{\tau_r^T} + \frac{S_e^{X_{\downarrow}}}{\tau_b} + \frac{S_e^{X_{\uparrow}}}{\tau_b}\end{aligned}$$

where, the initial conditions of these rate equations about spin evolution are shown as below:

$$\begin{aligned}
S^e(t=0) &= (0, 0, 0) \\
S^{T_\downarrow}(t=0) &= (0, 0, 0) \\
S^{T_\uparrow}(t=0) &= (0, 0, 0) \\
S^{X_\downarrow}(t=0) &= (0, 0, N_0) \\
S^{X_\uparrow}(t=0) &= (0, 0, 0)
\end{aligned} \tag{Eq. 4-31}$$

As a result, the exciton would produce a rather large negative IPS up to half a Pi in the limiting case theoretically.

4.3.2 Model BII

The prior exciton dynamical model BI we put forward applies to the current actual experimental results well. However, the common model BII with simple relaxation and conversion has been put forth here just for comparison.

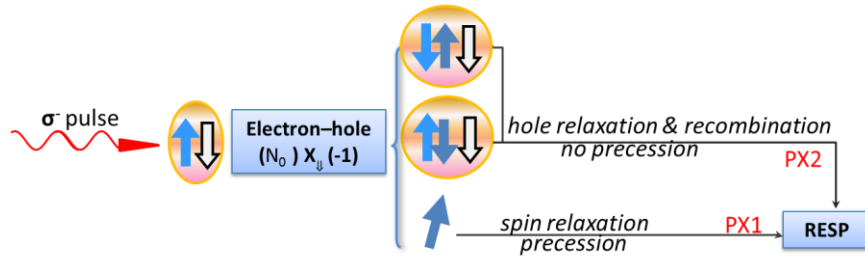


Figure 4-10: Schematic BII of modeling the common conversion of neutral excitons to trions and RESP.

In the usual case, the spin interactions between excitons and the resident electron-spin ensemble are proposed to just be through the transformation of exciton states. As a result, the IPS is only decided by the trion spin dynamics.

What is more, the situation of excitons and trions are excited at the same time should be mentioned here. The spin interplay between excitons, trions and electrons under exciton resonant excitation can be analyzed by the combination of model AII of trion spin dynamics in **Figure 4-5** and model BII of exciton spin dynamics in **Figure**

4-10. Under the very same magnetic field, the RESP will precess in phase with the electrons spins of excitons. The hole spin orientation in the excitons does not matter in the spin polarization of the resident electron ensemble, because it is the spin coherence of the electron in the exciton that is passed to the resident electron ensemble. Then a coherent spin transfers from exciton to the resident electron ensemble. During the secondary trions formation via the conversion of excitons, the hole spin orientation in the excitons will be out of way in the electron spin polarization, due to that the spin coherence of the electrons in the excitons is just passed to the RESP. The overall precessional spin polarization includes the RESP and the electron polarization in electron-hole pairs. The global IPS could be modified by all the trions recombination alone. While, the conversion process of excitons has not anything to do with IPS, to some extent.

4.4 Three Pulses Experiments

Even the negative IPS always happened in the experimental results, just as we mentioned before, we still want to further confirm the negative IPS in this QW, for ruling out the possible technique or human errors. Besides the general TRKR experiments as stated in Chapter 3 have been performed, a three pulses experiment has been performed with a second pump, named control here, retarded by a certain time. Since the change of the negative IPS definitely originates from the subsequently generated RESP component, and vice versa, for example, due to the trion recombination, the use of the controllable extra RESP component is beneficial. Thus, the more precise measurement of the intrinsic IPS can be expected.

4.4.1 Experimental Setup

In the event that a third pulse is required either for the state preparation or for the control of electron spins, the experimental setup is changed slightly from that in **Figure 3-10**. The three-pulse schematic diagram is shown in **Figure 4-11** with the third beam labeled as control. The control beam path passes the pulse through the other QWP and the chopper just as the pump does. The control and probe both have delay stages to set the relative arrival times of the pulses with respect to pump. Again, the probe pulse is sent to the spectrometer, where the signal is then measured through the double lock-in detections as mentioned before.

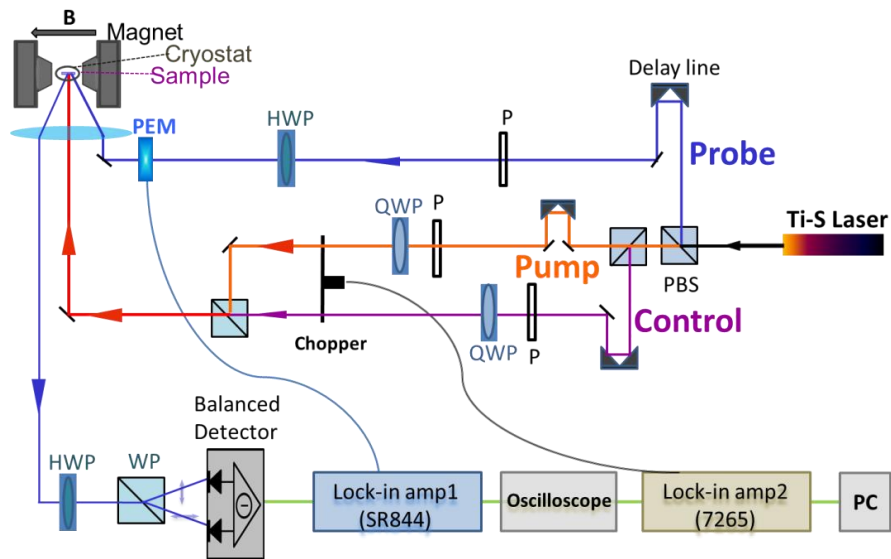


Figure 4-11: A schematic of a three pulses TRKR setup. All the detailed illustrations are same as that in **Section 3.5**.

4.4.2 Dependence of IPSSs on Control Power

In this measurement, the controllable extra RESP component is produced by the other circularly polarized control pulse. **Figure 4-12** shows the TRKR signals excited by σ^- pump with (a) σ^- and (b) σ^+ control pulses that were denoted by σ^-/σ^- and σ^-/σ^+ ,

respectively, under $B_x = 136$ mT and 10 K. The control pulse was retarded by $\pi/2$ (around 90 ps) and was varied from 0.5 mW to 10 mW for both cases. For the constant RESP generated by the first pump pulse, the control pulse produces the extra RESP with the relative phase $\pi/2$ for σ^- and $3\pi/2$ for σ^+ . The relative phase shift ϕ of the combined total RESP can be varied by changing the control power as indicated in the insets of **Figure 4-12** (a) and (b). The $|\phi|$ is expected to shift down with decreasing the extra RESP component and to converge to the intrinsic IPS produced by the first pump pulse in the limit of the zero control power.

The ϕ of the RESP precessions are plotted in **Figure 4-12** (c). The ϕ was obtained from the fitting over the range of 500 ~ 3000 ps. As shown in **Figure 4-12** (c), each absolute phase shift $|\Phi_-|$ for σ^-/σ^- signal is much larger than that $|\Phi_+|$ of σ^-/σ^+ curve under the same power of the control pulse, whose mean symmetry centerline is far away from zero level. The $|\Phi_-|$ and $|\Phi_+|$ change and converge to the same nonzero phase shift (- 0.38 rad) at $P_{control} = 0$ μ W consistently, corresponding to the phase shift of the original signal excited by the single pump pulse and also similar to the IPS (-0.35 rad) in **Figure 4-12** (b). In addition, as seen from the curves of $|\Phi_-|$ and $|\Phi_+|$, they are not strictly mirror-symmetric about the horizontal dashed line of $\phi = -0.38$. This is due to the existence of the intrinsic IPS caused by the first pump pulse excitation as well as the varying intrinsic IPSs and the slightly different relative phases of RESP component induced by the control pulses.

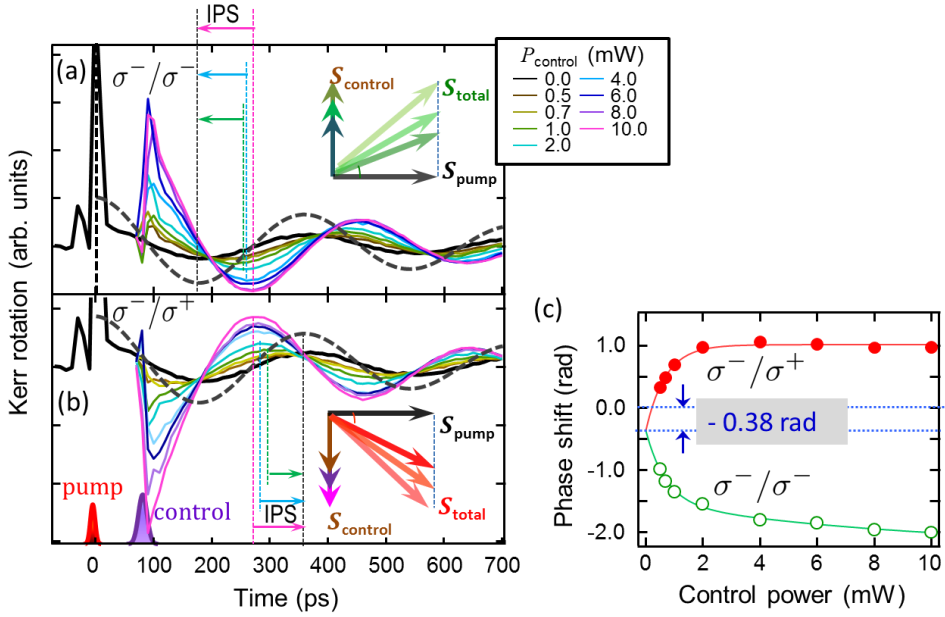


Figure 4-12: TRKR signals obtained by both σ^- pumps of 10 mW and (a) σ^- or (b) σ^+ controls with different excitation power and the delay by $\pi/2$ (136 mT, 10 K). The dark dashed signal is a $IPS = 0$ curve as the reference. (c) The corresponding phase shifts from the fitting of the signals (a) (green) and (b) (red). Both the phase shifts almost converge to -0.38 rad in the limit of zero control power.

4.5 Dependence of IPSs on Excitation Power

For a deeper insight into the interplay between the dynamical evolution of trions and the resultant IPS of RESP, the TRKR signals under $B_x = 146$ mT (precession period $2\pi/\omega_L = 333$ ps) were measured as a function of the pump power over the range of 1~10 mW as shown in **Figure 4-13** (a). **Figure 4-13** (b) summarizes the IPS values of these TRKR signals in **Figure 4-13** (a). For all the pump powers, the negative IPS was observed and the absolute value mainly increases and then saturates with the increasing pump power. The maximum negative IPS of ~ -0.35 rad was obtained at the pump power of $P_{pump} \sim 8$ mW. By using **Eq. 4-18**, **Eq. 4-19** and **Eq. 4-26**, IPS is calculated as functions of τ_{sh}^T and τ_r^T under the experimentally used $B_x = 146$ mT (**Figure 4-13** (c)). It

is that the negative IPS is obtained in the region of $\tau_{sh}^T \leq \tau_r^T$ and IPS comes to zero when τ_{sh}^T approaches to τ_r^T . **Figure 4-13** (d) is a slice of the 2D plot at $\tau_r^T = 85$ ps, which was practically obtained from the independent time-resolved PL measurements. If the relation between the pump power (trion density) and the hole spin relaxation time is known, the data in **Figure 4-13** (b) and (d) can compare directly, but the saturation point on the IPS is a better choice in the evaluation of τ_{sh}^T at the present stage. Obviously, the maximum negative IPS is ~ -0.39 rad at $\tau_{sh}^T \sim 15$ ps in the calculate result at $B_x = 146$ mT and agrees well with the experimentally obtained result of -0.35 rad.

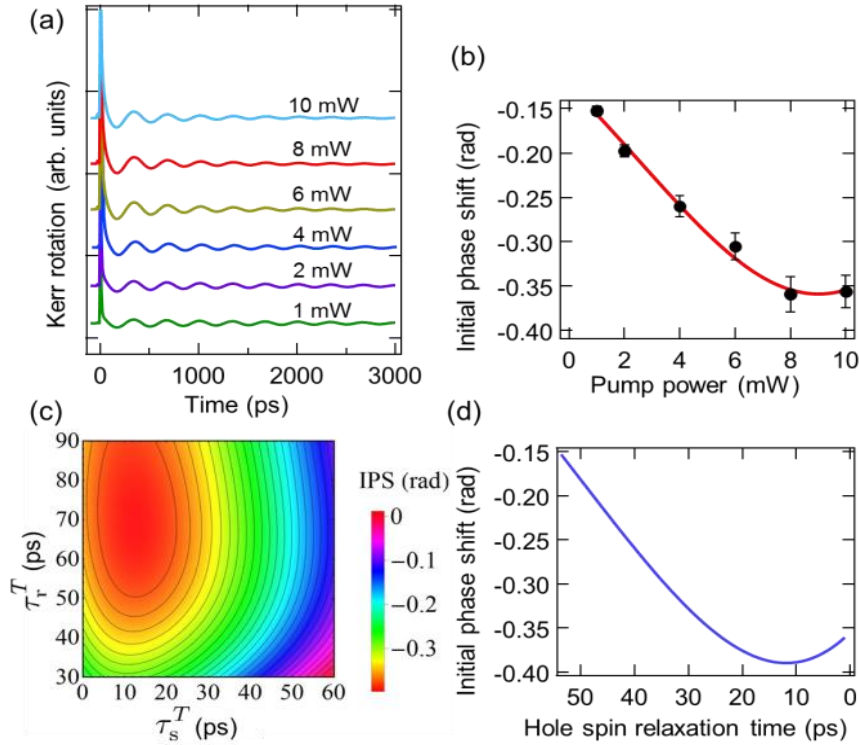


Figure 4-13: (a) TRKR signals as a function of pump power (146 mT, 10 K). (b) Experimental IPSs (symbols) of RESP with varying pump power (the solid line is a guide for eyes). (c) The calculated IPS contour plot as functions of the recombination time τ_r^T and the hole spin relaxation time τ_{sh}^T . (d) The theoretical IPS as a function of τ_{sh}^T , which is a slice of (c) at $\tau_r^T = 85$ ps.

The fitting for the RESP component over the time range: $t = 500\sim3000$ ps indicates that τ_S^e decreases from 1800 ps to 800 ps with increasing the pump power, as shown in **Figure 4-14**. The possible reasons for the reduction of τ_S^e , as the pump power increases, are the stronger electron spin-spin interaction in the bigger spin density, and phonon scattering due to the increase of the heating of resident electrons by optical excitation. Because, for the resident ensemble spins, the intrinsic tendency of electron spins to precess in the effective magnetic field as a result of spin-orbital interaction. Whereas, the electron spin lifetime is still too long to affect their IPS.

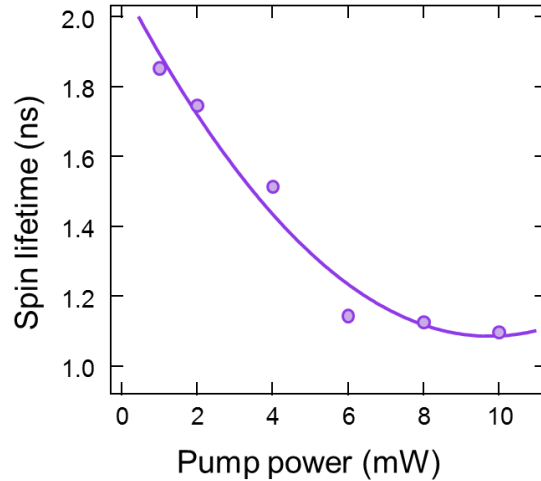


Figure 4-14: Experimental spin lifetimes (symbols) of RESP with varying pump power (the solid line is a guide for eyes), from the fittings of the TRKR signals.

4.6 Dependence of IPSs on Magnetic Field

In this section, a set of TRKR curves has been detected under the various magnetic fields B_x up to ~ 720 mT and $P_{pump} = 8$ mW in **Figure 4-15** (a). The used B_x corresponds to $\omega_L = 0.45 \sim 9.24 \times 10^{-2}$ rad/ps (period $1390 \sim 68$ ps). The RESP components were fitted over the time range of $t = 500\sim3000$ ps. Obviously, the RESP

decays faster with increasing B_x (τ_S^e changes from 1185 ps to 500 ps). This reduction of τ_S^e is attributed to the averaging effect of a macroscopic number of spins having the inhomogeneity of g-factor due to the fluctuation of well width and alloy composition of the barrier material. The similar dephasing effect was reported in the later listed references [17, 18].

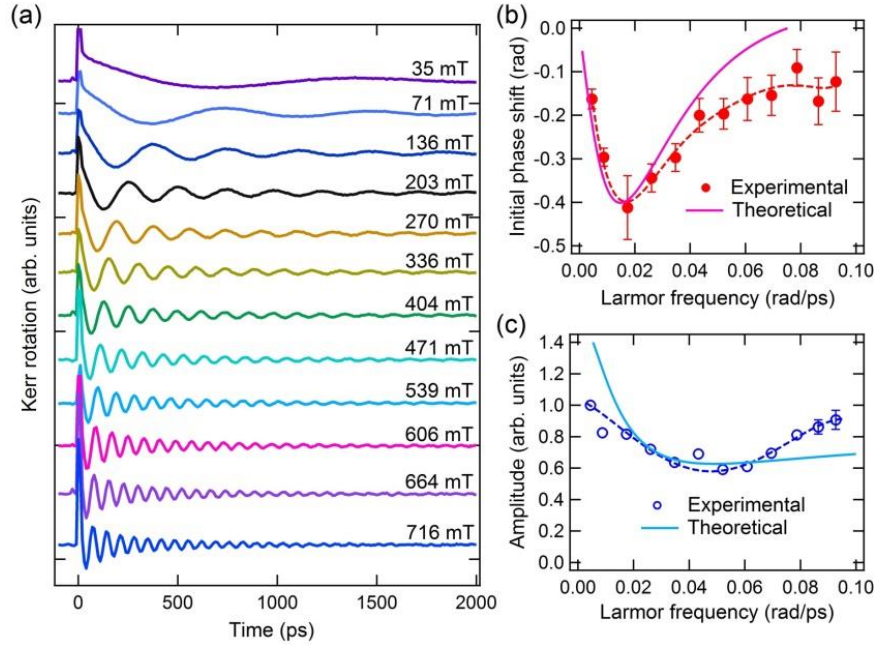


Figure 4-15: (a) The dependence of the TRKR signals on B_x in the range of 35~716 mT at $P_{pump} = 8$ mW. (b) The corresponding IPS (solid circles), as well as the simulated IPS denoted by a solid line. (c) The corresponding relative amplitude (open circles) and the calculated amplitude denoted by a solid line. The calculated IPS and amplitude are plotted as a function of Larmor frequency under $\tau_{sh}^T = 15$ ps and $\tau_r^T = 85$ ps. The dashed lines in (b) and (c) are the guides for eyes.

From these TRKR signals, the dependence of the IPS on Larmor frequency is plotted by the solid circles in **Figure 4-15** (b). The absolute value of the negative IPS firstly increases only in the small Larmor frequency range ($\omega_L \leq 2 \times 10^{-2}$ rad/ps, $B_x \leq 200$ mT) and then decreases with increasing ω_L . What is more, their RESP amplitude decreases at first and then goes up gradually with increasing ω_L as indicated by **Figure**

4-15 (c). The IPS and amplitude of Kerr rotation in dependence on ω_L from the model calculation were also shown by a solid line in the respective figures. For the model calculation, we took the values of $\tau_r^T = 85$ ps and $\tau_{sh}^T = 15$ ps as mentioned above. Theoretical IPS reproduces well the experimental results in small ω_L region and deviates a little to smaller values in large ω_L region. In addition, the variation trend of theoretical amplitude displays a similarity with that of experimental results. Although the deviation in large ω_L region in both figures becomes larger and larger with the increasing Larmor frequency by the same tiny time error, the overall trend of the ω_L -dependences of IPS and amplitude of RESP was found to be applicable to explain the experimental results.

4.7 Dependence of IPSs on Excitation Photon Energy

In this dissertation, we also performed the TRKR measurements when the photon energy of the pump pulse was scanned from 1.6035 eV (lower than the resonant exciton-state transition) to 1.6164 eV (higher than the resonant exciton-state transition). The sample was always excited resonantly by the narrower spectral pump pulse of picosecond mode compared to the trion spectrum, neutral exciton spectrum, as well as obviously the binding energy. Thus, we could analyze the situation of trion and exciton dynamics separately. In addition, beyond the allowed range, the Kerr signals were too weak or too short to acquire the accurate initial phase under the excitation energy below this minimal photon energy or above the maximal one. Even the photon energy of probe was also changed exactly just as with pump, we suppose the precessional traces with a rather long transverse decay time belong to the RESP dynamics.

4.7.1 Photon Energy Dependence under the Invariant Power

Some of the TRKR signals generated by the varying wavelength pulses (773.0 nm \sim 767.1 nm; 1.6509 eV \sim 1.6164 eV) with the same pump pulse power under the applied magnetic field of $B_x \approx 190$ mT are exhibited in **Figure 4-16**. From these curves, we can clearly see that the strength, spin transverse decay rate, as well as the initial phase of RESP in the Kerr rotation signals are changing with the different photon energy. Especially, for higher photon energy, the Kerr signals display some unusual time-resolved curves near the time origin. We will discuss this question further below in the next section.

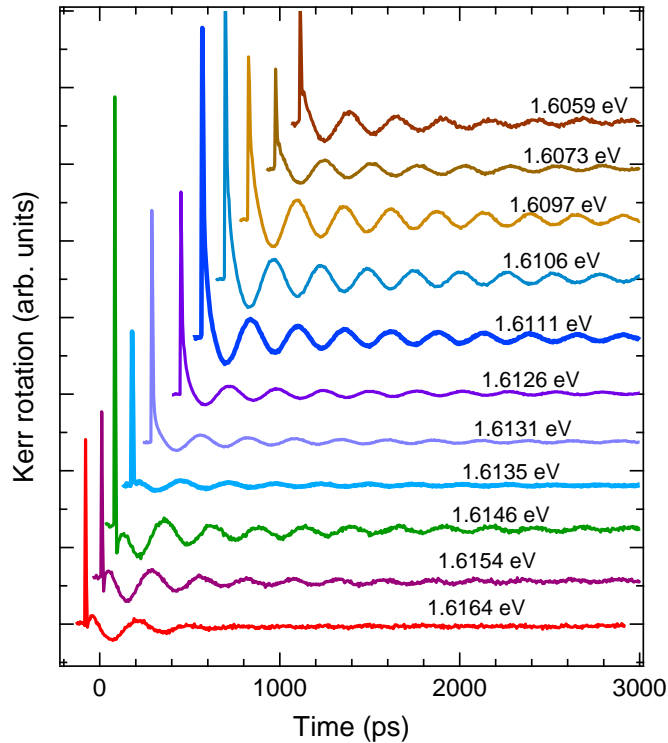


Figure 4-16: TRKR signals for the different pulse photon energy under $B_x = 190$ mT.

In order to analyze the RESP composition in the available precessional information, the TRKR signals displayed in **Figure 4-16** has been fitted over the time

range of $t = 300\sim3000$ ps. Then their relative amplitudes and SDTs of the RESP through different excitation photon energy from 1.6041 eV to 1.6164 eV are shown in **Figure 4-17**. The amplitude is changing nonlinearly irregularly decrease with the increase of pulse photon energy, which is most likely due to the different transition rate of different carriers and optical excitation under the varying wavelength and the varying photon numbers with the same pump power by passing the variable neutral density filter. Since this variable neutral density filter ideally has frequency dependence, and one photon energy is different for each wavelength component. Thus, the constituent components with different wavelength of the laser pulses are attenuated proportionately. As long as we adjust the variable neutral density filter to set a constant pulse power for the pump, the corresponding macroscopic photon numbers would reduce with the photon frequency increases for one laser pulse. What is more, the SDT curve clearly indicates that the lifetime of RESP has a variation of direct proportion with the RESP density by ruling out the light heating effect under the same power. The RESP lifetime does not decreases with the increasing RESP. This result is different with that in **Figure 4-14**. Therefore, we can suppose that the different exciton as a particle performs the same action for the spin decay.

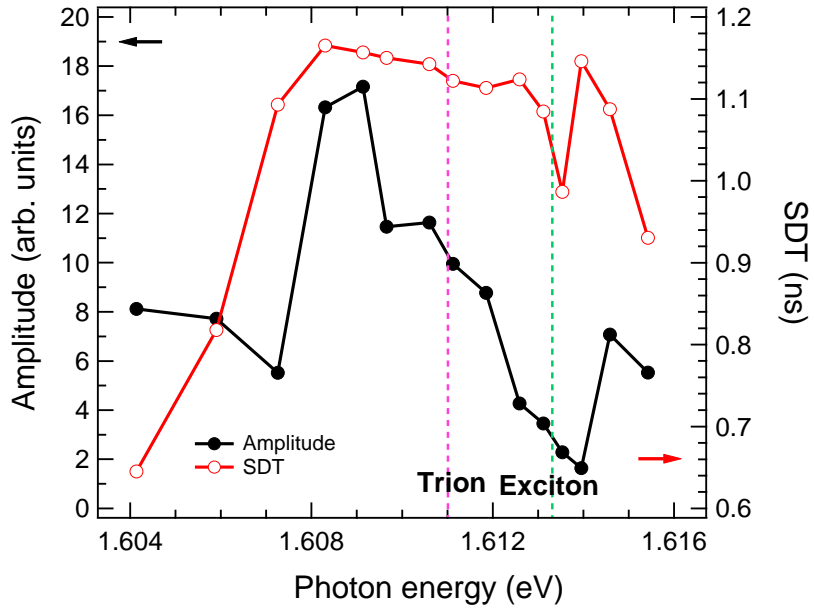


Figure 4-17: The relative amplitude (black symbols) and the SDT (red line) curves of RESP as a function of pulse photon energy from the TRKR signals with the same pump power 3 mW. The pink and green vertical dashed lines are used to mark the resonant transition energy of trion and neutral exciton, respectively.

Figure 4-18 summarizes the IPSs of the RESP through fitting the TRKR signals under the varying excitation photon energy from 1.6041 eV to 1.6164 eV displayed in **Figure 4-16** over the time range of $t = 300\text{--}3000$ ps. Seen from the blue trend line of IPS in **Figure 4-18**, the absolute value of the IPS slightly decreases at first and then suddenly goes up with the increasing pulse photon energy. However, the absolute value of the negative initial phase for RESP as the weak precessional signal with a long transverse decay time quickly starts to raise with the photon energy increases from 1.6131 eV (768.7 nm) to 1.6164 eV (767.1 nm) after just passing over the neutral exciton resonance. In a lesser extent of photon energy (0.0023 eV), the excitons might be excited and decay to some negative trions and create a part of RESP. Of course, only the transforming process itself from excitons to trions could not induce any large initial phase shift. Thus we

concluded that the excitons perform some unusual spin dynamics, just indicated by the TRKR curves shown in **Figure 4-16**.

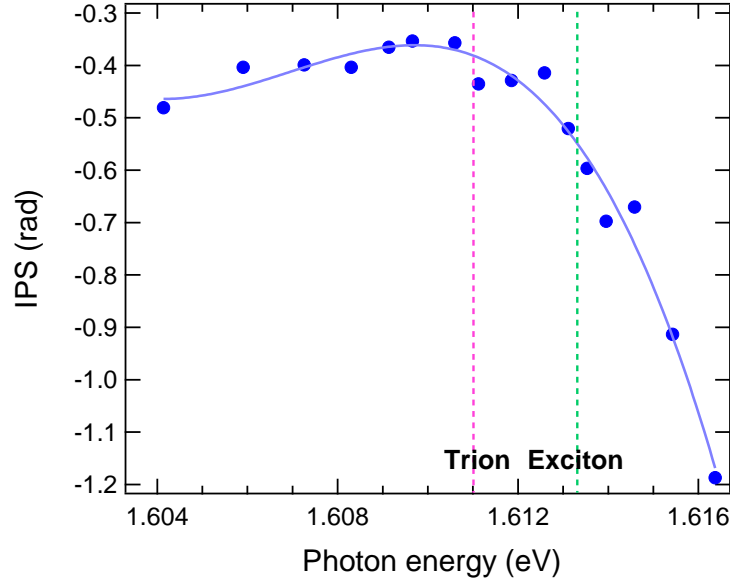


Figure 4-18: The photon energy dependence of IPSs (circular blue symbols). The pink and green dashed lines are used to mark the resonant transition energies of neutral trion and exciton, respectively.

4.7.2 Energy Dependence with the Equal Amount of Photons

To illustrate further the relationship between pump energy (wavelength) and ISP, the variable neutral density filter was fixed at the state of 8 mW for trion resonant photon energy of 1.6110 eV. Furthermore, the pulse photon energy of pump would be changed freely with the varying central photon energy. Therefore, the power of the pulses could be changed when they pass the same area of the filter with different wavelength, but there was not any reduction of photons. In addition, the impact of pulse power was negated. Then the relative amplitudes and SDTs of the RESP through under different excitation photon energies from 1.6035 eV to 1.6154 eV are shown in **Figure 4-19**. Clearly, the relative amplitude and SDT synchronously increase firstly and then go down quickly as

the pulse photon energy increases. Besides, they reach the maximum values around the point of trion resonant transition. Moreover, it is clear that the SDT of RESP is in direct proportion to the corresponding amplitude intensity as we have explained above.

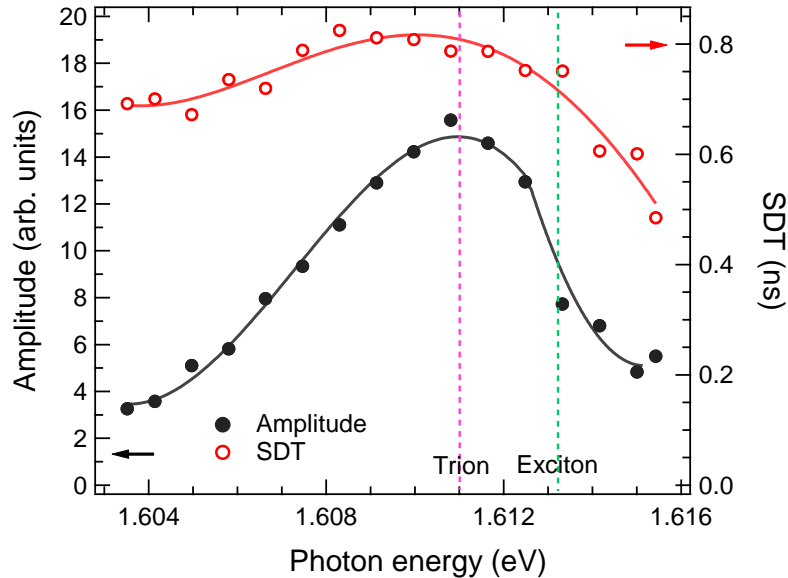


Figure 4-19: The relative amplitudes (black symbols) and the SDTs (red circles) of RESP as a function of pulse photon energy for the TRKR signals excited by the pump with almost the equal amounts of photons. The pink and green vertical dashed lines are used to mark the resonant transition energy of neutral trion and exciton, respectively.

The corresponding IPSs of the RESP through fitting the TRKR signals under the varying excitation photon energy from 1.6035 eV to 1.6154 eV are shown in **Figure 4-20**. According to these results, the negative initial phase is almost constant for the pulse photon energy in the range of 1.6035 eV ~ 1.6127 eV (772.6 nm ~ 768.9 nm) around the trion resonance (at 1.6110 eV; 769.7 nm), other things being equal. Therefore, the trions and resident electron spin polarization can be excited within a large spectrum range (0.0077 eV) of the excited photon energy, which has a negligible effect on the negative IPS. In addition, the significant role played by e-h pairs on IPS can be confirmed again.

Consequently, one possibility of inducing the larger IPS is that e-h pairs could decay to the secondary trions later by taking a transformation time τ_b , which creates the secondary remaining RESP after the exchange interaction of e-h pairs. The transformation from excitons to trions also has been proved by the photoluminescence and photoluminescence excitation experiments [4].

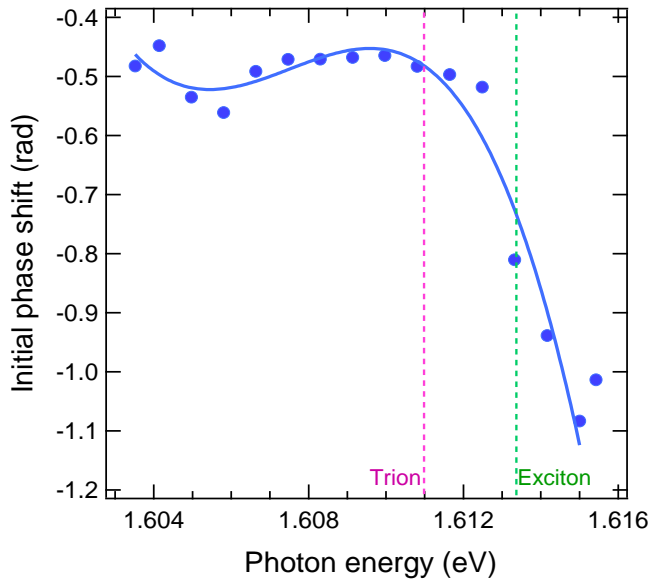


Figure 4-20: The photon energy dependence of IPSs (blue dots). The blue line is a guideline for eyes. The pink and green dashed lines are used to mark the resonant transition energy of the trion and neutral exciton, respectively.

4.8 Signal Components during Carriers Evolution

Finally, through all above theory analysis and data experiments, we have proved from the TRKR signals' components that we get the trion and the e-h pairs spin dynamics and demonstrate the evolutionary models we have put forward in this dissertation.

4.8.1 Kerr Signal Components at Trion Resonance

A typical Kerr rotation signal obtained by the pump ($P_{pump} = 10$ mW) at trion resonant transition under $B_x = 331$ mT and 10 K is exhibited by the red plot in **Figure**

4-21 (a). Since a negative trion consists of two spin-paired electrons (singlet state) and a hole, the total g-factor in x-direction is zero in a QW, Therefore, the negative trion decay was seen as the heavy hole spin dynamics due to trions' rapid recombination and hole spin flip without a spin-precessional motion caused by the magnetic field as mentioned above. Therefore, there are only two constituents of non-precessional hole spin with a short survival time and the precessional trace of RESP with a long coherence time included into this TRKR signal.

What is more, the hole spin of trion plays out a nonlinear variation according to the equation of $S^T(t) = N_0(2e^{-(\frac{t}{\tau_r^T} + \frac{t}{\tau_{sh}^T})} - e^{-\frac{t}{\tau_r^T}})$. Thus, the experimental TRKR signal has been fitted generally by the single exponential function in **Eq. 4-32** to time traces at the delay time range of $t = 300 \sim 3000$ ps in order to exclude the trion component affection. Except the initial phase ϕ of the RESP oscillation analyzed above, the lengthened green curve of extrapolating back the fitting for the RESP precessional signal $A^e \exp(-t/\tau_s^e) \cos(\omega_L t + \phi)$ (a blue solid curve) to zero time delay cannot wholly cover the oscillation composition of the measuring original Kerr signal as indicated especially by the first wave trough from the original signal downdraft as indicated by **Figure 4-21** (a). In fact, we could go further ahead and find that the first trough of wave combines the reverse hole spin constituent caused by the flip-stop of hole spin, just as displayed by the simulated transients of the heavy hole spin polarization of the trions (yellow curve) with $\tau_s^e = 1299$ ps, $\omega = 0.0428$ rad/ps in **Figure 4-21** (b). The RESP spin precession is shown to the first rise due to trion formation and the second reinforcement from the trion recombination later. Then it decay according to the electron spin dephasing from the simulated RESP traces denoted by the blue curve in **Figure 4-21**

(b). The overall spin polarization, plotted by the red curve in **Figure 4-21** (b), represents well the measured transient Kerr rotation signal for trion excitation shown in **Figure 4-21** (a). In a word, the simulated plots agree with the actually experimental Kerr data quite well.

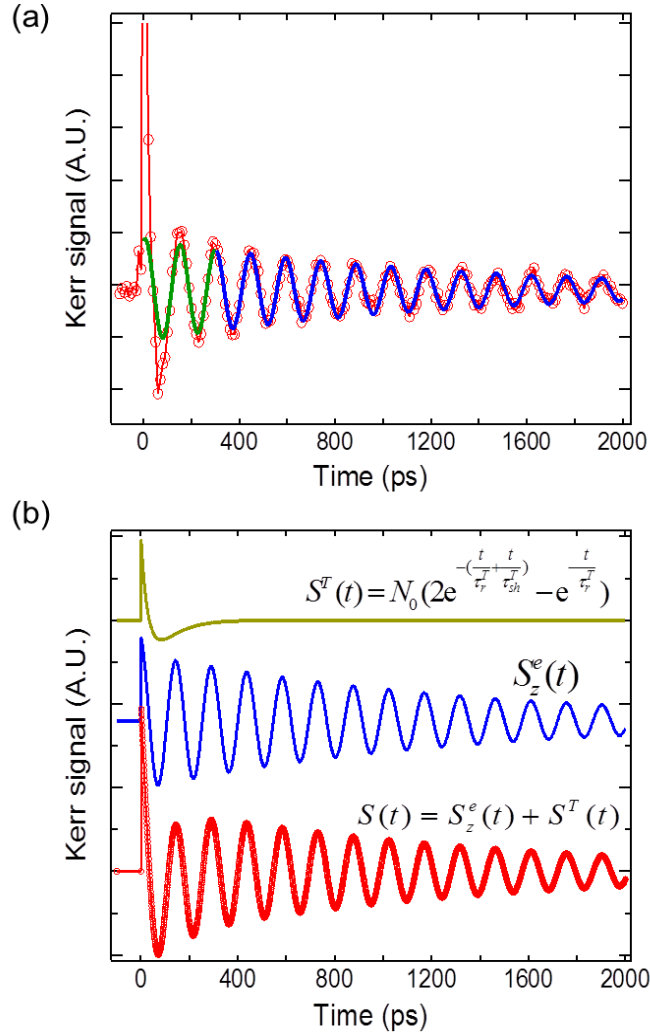


Figure 4-21: (a) A general TRKR signal ($P_{\text{pump}} = 10$ mW; $B_x = 331$ mT and 10 K) denoted by the red symbols; the fitting of RESP precessional component (blue solid line) and the extend curve (green solid line) of extrapolating back to zero time delay for the fitting curve. (b) The simulated components of the heavy hole spin polarization of the trions (yellow curve), the z-component of RESP (blue plot), separately, and the combination of the two components (red line).

4.8.2 Conversion of Excitons

As the above analysis of the uncommon Kerr signals for the higher pulse energy than the neutral exciton resonant transition shown in **Figure 4-16** and the corresponding larger IPSs indicated by **Figure 4-18**, there might be a different exciton evolution for the e-h pairs being produced in a bound state. First of all, the trions transformed from excitons are likely to come out, as seen from the long lifetime of the weak RESP signal. However, these processes are more complicated and are not enough thoroughly studied for possible tens of hypothetical situations and models. Furthermore, the simple transformation of exciton cannot produce such a larger negative IPS.

After a deeper insight into a typical Kerr rotation signal obtained by the high energy excitation of 1.6146 eV as shown in **Figure 4-22**, there is a first fast downward decay in the TRKR signal during the original time of 0 ps ~ 10 ps. More particularly, it goes down to below the zero level largely from the positive spin polarization in less than 10 ps, which identifies that both the hole spin and electron spin have to reverse themselves at the same time rather than usual relaxation behaviors. Concretely speaking, most of the whole neutral excitons happen to flip just after excitation, as described by the first step in **Figure 4-9**. Following that, the secondary excitons after flip-flop for holes and electrons start the recombination relaxation. Meanwhile, some of them will lose some energy by scattering and convert to the negative trions by combining with an electron with the opposite spin from the resident electron ensemble. Then it creates a RESP denoted by the process P1. This conversion cannot be detected by the TRKR technique directly unfortunately, since the total spin polarization always remains as a constant just during the process. Then, the e-h pairs recombination and the trion recombination both

make the Kerr signals raise again. In addition, during the e-h pairs' relaxation, some of them also convert into the other negative trions to create the RESP of P2, just as another reported result [19]. Finally, the RESP of P3 has been left after the trion recombination. In a word, we have demonstrated the evolved mechanism of e-h pairs with the flip-flop interaction for the both bound electron spin and hole spin combined the theoretical simulation of model BI.

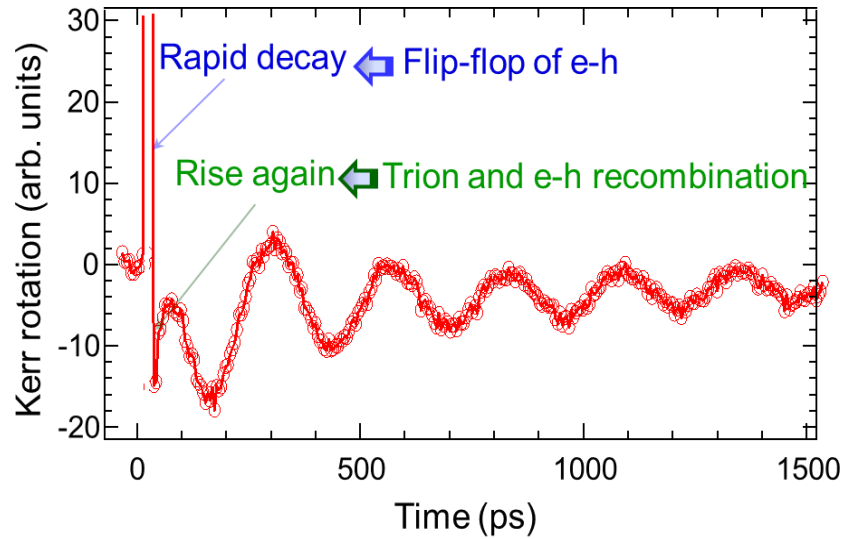


Figure 4-22: An example of the TRKR signal excited under the photon energy of 1.6146 eV above the neutral exciton resonant energy.

Of course, the process of e-h pairs also takes an action for the initial phase-shift, mainly due to the composition of P2 (\downarrow), as displayed in **Figure 4-9**. Moreover, a little portion of the negative phase shift is caused by the delayed P3 like the situation of trion resonant excitation discussed previously, since the g-factor of heavy holes are almost zero and they always induced the returned spin as a net spin up or spin down of z-component, never as the superposition. We know the composition P1 of RESP

immediately starts to precess after light excitation, thus P1 could not contribute any phase shift.

The TRKR signals acquired from the experiments between the trion and exciton resonant excitation (from 1.6110 eV to 1.6133 eV) might contain the above double spin dynamics, as well as the intermediate values of negative IPSs. Although only the $n = 1$, $n_z = 1$ heavy hole exciton transition is studied in this work, the probe beyond neutral exciton transition might monitor the spin from e-lh excitons generated by pump with the same photon energy, since we know the probe pulse might detect different signals when the detection photon energy passes through a resonance. In this case, all the carriers' spins would become the opposite spin polarizations depicted in **Figure 4-9** by neglecting the possible hh-lh mixing.

4.9 Summary

In all, a negative IPS phenomenon has been successfully demonstrated via systematically investigating the precessional traces of RESP involving the trion and exciton spin dynamics in a CdTe SQW with a rather low density of resident electrons by a pump-probe setting. In addition, the negative IPS was identified as a result of the intrinsic spin polarization dynamics, especially confirmed by a more proof of the double pump excitation experiments, as discussed above. Through the interpretation of a trion formation process in the experimental and theoretical model analysis, we found the investigation of negative IPSs in TRKR signals, which give the important clues about the generation processes of RESP. The experimental and theoretical studies involving the interplay between the trions, excitons and RESP with the IPS play crucial roles in the dynamical process study of RESP.

In addition, we found that the magnitude of IPS can be controlled by the external parameters such as the excitation power and the strength of external magnetic field. Furthermore, the results of theoretical simulation agree well with the experimental factors for the overall trends of IPSs: the absolute value of the negative IPS mainly increases with the excitation power. Furthermore, it changes with the Larmor frequency nonlinearly. Additionally, the experimentally obtained tendency of the RESP amplitude except for a little drift under a higher magnetic field could be explained properly with the calculations.

Most interestingly, through the interpretation of the nonzero IPSs in the RESP precessions, the trion and exciton spin dynamical process and the RESP formation can be determined in the calculation as well as in the experiments, where the briskly asymmetric hole spin flip scattering accounts for the negative initial phase. Moreover, the exchange interaction in the excitons results in an even larger negative IPS. For such a scenario, the negative IPS can come out as far as there is a one-way fast hole spin-flip within one order of around tens of picoseconds from T^{\downarrow} to T^{\uparrow} alone under σ^- polarized excitation, vice versa for σ^+ excitation, especially shorter than their recombination time. In result, the theoretical models of the trions, excitons and RESP formation and evolution processes have been confirmed in this precise and satisfactory way. Moreover, the modeling of RESP is a great help for analyzing the experimental data and obtaining some physical information that cannot be acquired via experimental methods.

4.10 References

- [1] J. Tribollet, F. Bernardot, M. Menant, G. Karczewski, C. Testelin, M. Chamarro. Interplay of spin dynamics of trions and two-dimensional electron gas in a n-doped CdTe single quantum well[J]. Phys. Rev. B 2003; **68**: 235316.
- [2] S. L. Lu, H. Noshio, A. Tackeuchi, L. F. Bian, J. R. Dong, Z. C. Niu. Spin-Polarized Localized Exciton Photoluminescence Dynamics in GaInNAs Quantum Wells[J]. Jpn. J. Appl. Phys. 2009; **48**: 100206.
- [3] R. T. Harley, M. A. Brand, A. Malinowski, O. Z. Karimov, P. A. Marsden, A. J. Shields, et al. Ultrafast spin evolution in high-mobility 2DEGs[J]. Physica E: Low-dimensional Systems and Nanostructures 2003; **17**: 324-328.
- [4] Z. Chen, R. Bratschitsch, S. G. Carter, S. T. Cundiff, D. R. Yakovlev, G. Karczewski, et al. Electron spin polarization through interactions between excitons, trions, and the two-dimensional electron gas[J]. Phys. Rev. B 2007; **75**: 115320.
- [5] W. Ossau, D. R. Yakovlev, C. Y. Hu, V. P. Kochereshko, G. V. Astakhov, R. A. Suris, et al. Exciton-electron interaction in quantum wells with a two dimensional electron gas of low density[J]. Physics of the Solid State 1999; **41**: 751-756.
- [6] P. Palinginis, H. Wang. Coherent Raman scattering from electron spin coherence in GaAs quantum wells[J]. J Magn Magn Mater 2004; **272**: 1919-1920.
- [7] W. Shichi, T. Ito, M. Ichida, H. Gotoh, H. Kamada, H. Ando. Dependence of Electron g-Factor on Barrier Aluminum Content in GaAs/AlGaAs Quantum Wells[J]. Jpn. J. Appl. Phys. 2009; **48**: 063002.
- [8] G. Salis, D. T. Fuchs, J. M. Kikkawa, D. D. Awschalom, Y. Ohno, H. Ohno. Optical manipulation of nuclear spin by a two-dimensional electron gas[J]. Phys. Rev. Lett. 2001; **86**: 2677-2680.
- [9] E. Vanelle, D. Brinkmann, P. Gilliot, M. Paillard, X. Marie, T. Amand, et al. A detailed study of the dynamics of charged excitons in CdTe/CdMgZnTe quantum wells[J]. J. Cryst. Growth Journal of Crystal Growth 2000; **214–215**: 827-831.

- [10] S. A. Crooker, D. D. Awschalom, J. J. Baumberg, F. Flack, N. Samarth. Optical spin resonance and transverse spin relaxation in magnetic semiconductor quantum wells[J]. Phys. Rev. B 1997; **56**: 7574-7588.
- [11] E. A. Zhukov, D. R. Yakovlev, M. Bayer, M. M. Glazov, E. L. Ivchenko, G. Karczewski, et al. Spin coherence of a two-dimensional electron gas induced by resonant excitation of trions and excitons in CdTe/(Cd,Mg)Te quantum wells[J]. Phys. Rev. B 2007; **76**: 205310.
- [12] T. A. Kennedy, A. Shabaev, M. Scheibner, A. L. Efros, A. S. Bracker, D. Gammon. Optical initialization and dynamics of spin in a remotely doped quantum well[J]. Phys. Rev. B 2006; **73**: 045307.
- [13] G. V. Astakhov, M. M. Glazov, D. R. Yakovlev, E. A. Zhukov, W. Ossau, L. W. Molenkamp, et al. Time-resolved and continuous-wave optical spin pumping of semiconductor quantum wells[J]. Semiconductor Science and Technology 2008; **23**: 114001G.
- [14] I. A. Merkulov, A. L. Efros, M. Rosen. Electron spin relaxation by nuclei in semiconductor quantum dots[J]. Phys. Rev. B 2002; **65**: 205309.
- [15] R. I. Dzhioev, V. L. Korenev, B. P. Zakharchenya, D. Gammon, A. S. Bracker, J. G. Tischler, et al. Optical orientation and the Hanle effect of neutral and negatively charged excitons in GaAs/Al_xGa_{1-x}As quantum wells[J]. Phys. Rev. B 2002; **66**: 153409.
- [16] Z. Chen, S. G. Carter, R. Bratschitsch, S. T. Cundiff. Optical excitation and control of electron spins in semiconductor quantum wells[J]. Physica E: Low-dimensional Systems and Nanostructures 2010; **42**: 1803-1819.
- [17] J. Tribollet, E. Aubry, G. Karczewski, B. Sermage, F. Bernardot, C. Testelin, et al. Enhancement of the electron spin memory by localization on donors in a CdTe quantum well[J]. Phys. Rev. B 2007; **75**: 205304.
- [18] E. A. Zhukov, D. R. Yakovlev, M. Gerbracht, G. V. Mikhailov, G. Karczewski, T. Wojtowicz, et al. Spin coherence of holes and electrons in undoped CdTe/(Cd,Mg)Te quantum wells[J]. Phys. Rev. B 2009; **79**: 155318.
- [19] C. R. L. P. N. Jeukens, P. C. M. Christianen, J. C. Maan, D. R. Yakovlev, W. Ossau, V. P. Kochereshko, et al. Dynamical equilibrium between excitons and trions in CdTe quantum wells in high magnetic fields[J]. Phys. Rev. B 2002; **66**: 235318.

CHAPTER 5

DYNAMIC NUCLEAR SPIN POLARIZATION

5.1 Nuclear Hyperfine Research Background

5.1.1 Nuclear Spin Research Review

The coupling HFI between the electron and the ensemble nuclear spins recently has attracted considerable attentions for the prospect of the electronic and nuclear spins applications in spin-based quantum information processing [1]. While a controllable DNSP acting as an effective magnetic field can also be employed as an effective tool to study and manipulate electron spin dynamics in spin-based electronic devices [2]. This NSP has been largely observed in the past in bulk semiconductors [3], even in QWs [4-6] and recently in QDs [7-10].

In addition, as we mentioned firstly, the long spin coherence for RESP is required in the potential applications of the spin degree of freedom [11-14]. However, the great obstacle lies in creating RESP without any loss of polarization during the process. While, along external magnetic field, the main remaining electrons spin dynamic channel for RESP is the contact HFI serves as a conveying pipe between itinerant carriers (conduction electrons) and the surrounding stationary moments (lattice nuclei) as a result of the establishment of equilibrium between these two reservoirs [15]. The angular momentum can be transferred from the electronic to nuclear reservoirs and vice-versa through mutual spin flips. But other than that, we know the dynamic nuclear spin

polarization (DNSP) fluctuation would modify their spin Hamiltonians and has a destructive effect leading to electron spin relaxation and decoherence. In addition, it would limit the number of quantum operations and reduces the potential performance [9].which influence the functionality of spintronic devices, especially for the quantum information processing devices in nanostructures. To suppress or avoid the influence of HFI for utilization of a potential long carrier spin coherence, the use of hole spin instead of electron spin has been studied [16, 17]. This is because the dipole-dipole type HFI that affects hole spins is believed to be considerably weaker than the contact-type HFI that affects electron spins. Alternative way is a choice of semiconductor materials consisting of isotopes with zero nuclear spin or low abundance isotopes with small nuclear spins and small HFI constants.

From this viewpoint, II-VI compound semiconductors, such as CdTe, are more preferable, since those generally have a smaller hyperfine constant compared to III-V compound materials such as GaAs [5]. Thus, it could expect smaller influence for electron spins coherence. Because CdTe [6] consists of the isotopes with $I_{Cd} = 1/2$; $P_{Cd} = 25\%$, $I_{Te} = 1/2$; $P_{Te} = 8\%$ and the other isotopes with $I_{Cd;Te} = 0$, where I_i ; P_i are nuclear spin and natural abundance of the isotope i, respectively. Since the II-VI semiconductor of CdTe has generally small abundance of the isotopes with $I=0$, the effect of HFI acting back on electron is expected to be 1 to 2 orders magnitude smaller than that in III-V counterparts such as InAs ($I_{In} = 9/2$; $P_{In} = 100\%$, $I_{As} = 3/2$; $P_{As} = 100\%$). However, a lot of researchers focus on the nuclear spin of InAs, GaAs-based quantum structures and a few SiGe structures [18, 19], only a few people have studied the CdTe QWs [20, 21] about the nuclear spins, recently. Besides, it is necessary to make a rather precise

measurement of intrinsic nuclear field value for the NSP estimation to perfectly complete the RESP study. However, the precise measurements of the NSP amount with this order of magnitude hold several experimental challenges and additional difficulties in the valuation of nuclear field effects. For example, it is difficult to study nuclear spins by creating equilibrium nuclear polarization directly due to the small value of nuclear magnetic moment. Therefore, we try to measure the DNSP through the RESP precession in a single CdTe QW by a TRKR method accurately.

Incidentally, the trions formed by one hole and a pair of electrons with opposite spins in a singlet state induce no effect of the HFI with nuclei, since the total electron spin in the charged exciton is zero and the hole spin is only weakly coupled to the nuclear spins due to the p-symmetry of the heavy-hole Bloch wave function [22] in the valence band for zinc-blende semiconductor crystals. DNSP is commonly induced by the component of electron spin along the applied field direction [23]. The spin relaxation of the electron spin component by transferring to nuclear spins along the external magnetic field would happen through HFI. In turn, the nuclei, as the charged particles, by the spinning movement can create an electromagnetic field in the same direction with the external field, like that from a bar magnet. As a result, the NSP reacts back on the normal component of electron spins as an effective magnetic field, which modifies the total magnetic field experienced by the electron spins. Therefore we have been attracted great interests on the evaluation and manipulation of nuclear spin effective field created from NSP and to keep the long coherence of resident electrons spins at the same time.

5.1.2 Hyperfine Interaction Theory

Commonly nuclear spins are subject to kinds of interactions, such as, the interaction with phonons [24], the HFI which is here considered, as well as the nuclear spins interaction with each other, leading to both relaxation mechanisms and nuclear spin diffusion [25], important in bulk semiconductors. However, nuclear spin diffusion is strongly suppressed by the natural confinement of the geometry in low dimensional nanostructures, such as QWs [26] and QDs [27, 28]. The HFI is a dominated coupling interaction for the nuclei and RESP in QWs.

The contact HFI conserves the total spin of the electronic-nuclear system and that through mutual spin flips, or “flip-flop” interactions, angular momentum can be transferred from the electronic to the nuclear reservoirs and vice-versa. To be specific, a nuclear spin alignment can be built up by the corresponding HFI: $\text{AI}\cdot\text{S}$ between the nuclear spins and the residual net electron spins. The magnetic moment of a nucleus due to its intrinsic angular momentum equation can be written as $M_I = I^* \gamma_N$. Then we can write the coupling Hamiltonian between the zinc-blende conduction band electron's spins and lattice nuclear spins, known as the contact hyperfine coupling which can be described in detail by the Fermi-contact Hamiltonian [29]:

$$H_{hf} = \frac{8\pi}{3} \frac{g\mu_B}{\hbar} \gamma_N \eta |\Psi(R)|^2 \mathbf{I} \bullet \mathbf{S} \quad \text{Eq. 5-1}$$

where, γ_N is the gyromagnetic ratio of nuclear spins, R is the position of the nucleus, $\Psi(R)$ is the envelope wave function and η is the Bloch amplitude at the site of the nucleus normalized by the volume of the unit cell, \mathbf{I} is the spin of nucleus; \mathbf{S} is the spin of electrons. Moreover, the constants of electron g-factor, Bohr magneton μ_B and reduced Plank constant \hbar are also included in the equation. So we can see the total interaction

energy is dependent on the electron spin and the orientation of each of the nuclear spins. From **Eq. 5-1**, the nuclear hyperfine coupling comes up as the electron density is overlapped with the nuclear site. Integrating over the unit cell, it was found that the contact hyperfine coupling leads to a variety of phenomena in zinc blende semiconductors including the Overhauser and Knight shifts in electron and nuclear magnetic resonance experiments, respectively. The detailed Fermi-contact Hamiltonian of HFI would be addressed later.

While, in return, as the electronic spins overlap with nuclear spins, the contact HFI will modify electrons spin Hamiltonians, such as the spin splitting:

$$\Delta E = h\Omega_L = g_z \mu_B B_0 + A_H \langle I_Z \rangle \quad \text{Eq. 5-2}$$

where A_H is the hyperfine constant and $\langle I_Z \rangle$ is the component of nuclear spin along the magnetic field. This is the main mechanism used to study DNSP in this dissertation.

5.2 Nuclear Spin Polarization Experiment

Although the above mentioned NSP [23] created by the component of optically injected spin-polarized electrons spin along the applied field direction via HFI has been largely observed in bulk semiconductors [30] in the past. It is difficult to study nuclear spins by creating equilibrium nuclear polarization directly due to the small value of nuclear magnetic moment and the reduced number of nuclei in low dimensional quantum nanostructures.

5.2.1 Overview of Experimental Techniques

In history, nuclear spins are usually investigated using standard experimental techniques such as nuclear magnetic resonance (NMR) [31-34]. In this technology, an applied magnetic field is used to orient nuclear spins, resulting in the polarization of

about 1% of all the nuclei in the sample, which is enough to detect and investigate the nuclear spin dynamics. In this experiment, the sample with a minimum of 10^{17} nuclei is required for a detectable NMR signal [25]. Nevertheless, the number of available nuclei in most QWs and QDs is less than 10^{12} and 10^5 orders of magnitude, respectively. Therefore, the nuclear spins in these kinds of low dimensional samples are hard to be investigated using NMR.

To compensate for the small number of nuclei in low dimensional systems, DNP can be used to increase the percentage of polarized nuclei available for investigation. For DNP measurement, an initial non-equilibrium electron spin polarization is transferred to the nuclear system via the HFI interaction [35, 36], as mentioned above. Consequently, nuclear spin dynamics can be directly investigated using optical nuclear magnetic resonance (ONMR) [36, 37] or TRFR or TRKR. In this dissertation, the nuclear spin field is investigated indirectly using tilted configuration of TRKR.

5.2.2 Tilted Configuration

In order to transfer the spin angular momentum from optically oriented electrons to the lattice nuclei, it is necessary to make the parallel or anti-parallel component S_{\parallel} of electron spin to Larmor frequency vector, because S_{\parallel} is a stationary component against the external magnetic field. Therefore, DNSP effect only occurs if a longitudinal component of electron spin polarization exists. In the Voigt geometry, which is necessary to observe spin precession, RESP is orientated perpendicular to the field, in principle and DNSP should not be observed since the longitudinal spin polarization averages to zero. Additionally, a direct longitudinal component of spin-injection can be created by simply tilting the applied magnetic field. Then, the nuclear effective field can be regarded as

additional effective magnetic field \mathbf{B}_N acting on the electron spins [28]. Accordingly, TRKR measurements were performed via the altered Larmor frequency under \mathbf{B}_N in the tilted-field geometry which is shown in **Figure 5-1** (a). The states of electron spin component perpendicular to \mathbf{B} would precess to reflect the Larmor frequency of total field of external magnetic field \mathbf{B} and the created nuclear field \mathbf{B}_N , as displayed in **Figure 5-1** (b), since the unpaired electron spins are sensitive to the local fields in their surroundings.

Here, the magnetic field was applied at an angle θ to the sample surface. After σ^- excitation, the component S_{\parallel} of RESP gives rise to DNSP. Thus, the observed Larmor frequency ω_L at which the transverse component of RESP rotates can be affected by the total energy of an electron spin consisting of the Zeeman energy $H_s (g\mu_B B \cdot S/\hbar)$ and the hyperfine energy $H_{hf} (A I \cdot S)$ in (creating an internal nuclear field \mathbf{B}_N), as stated in **Eq. 5-2**. Subsequently, the resulting polarized nuclear spins produce an Overhauser field \mathbf{B}_N around the Larmor frequency vector Ω , which is slightly tilted away from the \mathbf{B} direction by the ratio of the anisotropic g-factors with the correlation of $\tan\varphi/\tan\theta = g_{\parallel}/g_{\perp}$. However, for a small tilted angle, Ω , \mathbf{B}_N and \mathbf{B} point approximately into the same direction, the nuclear field just enhances ω_L . This indicates that RESP precesses about an axis can be given by the following function:

$$\omega_L = g_{\theta}\mu_B(\mathbf{B} \pm |\mathbf{B}_N|)/\hbar \quad \text{Eq. 5-3}$$

We also can make use of the good approximation: $|\mathbf{B}_N| = B(\bar{\omega}_L - \omega_L^{\text{PEM}})/\omega_L^{\text{PEM}}$.

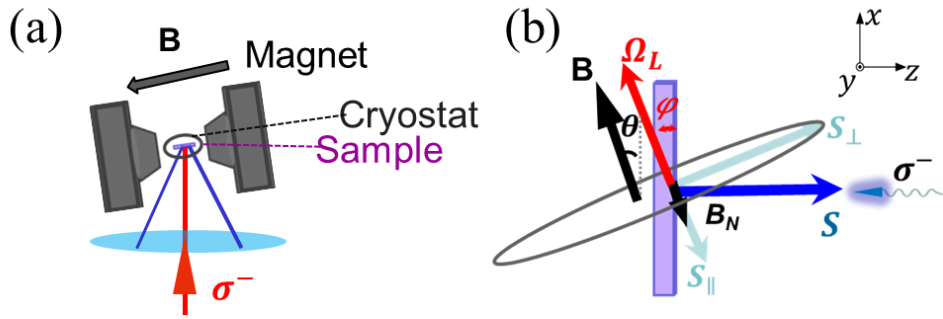


Figure 5-1: (a) Experimental tilted configuration and (b) its schematic illustration of tilted-field geometry under σ^- pump excitation with the tilted magnetic field by an angle of θ .

5.2.3 PEM Configuration

In the PEM modulation configuration, only the pump beam is modulated by a PEM which was set as at 50 kHz with retarding by quarter wave in phase, as shown in **Figure 5-2**. Thus this modulation can change the pump polarization between σ^+ and σ^- circular polarizations frequently minimizing the effect of \mathbf{B}_N via HFI. Since the build-up time of \mathbf{B}_N is much longer than the modulation period, the time-averaged zero electron spin population cannot create \mathbf{B}_N .

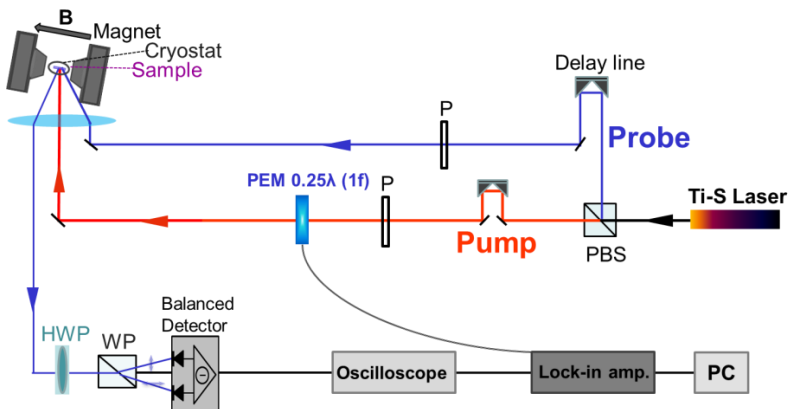


Figure 5-2: Experimental PEM modulation configuration. All other detailed illustrations are same as that in **Section 3.5** and **Figure 4-14**.

5.3 Experimental Results

5.3.1 G-factors

Before moving on to the precise estimation for nuclear field \mathbf{B}_N , we have to make a careful evaluation for the g-factors in the SQW sample under no effect of \mathbf{B}_N via the PEM setup above, because the accurate measurement of g-factors is one of the key components for detecting NSP and its influence on RESP coherence.

Due to quantum-confinement and the penetration of the electron wave function into the QW barriers, the g factor in a narrow QW can differ substantially from the bulk semiconductors value. There are different values of g between the in-plane direction (g_{\perp}) and the growth quantization axis (g_{\parallel}). All the g-factors in the previous chapters mean the in-plane g_{\perp} .

A. Transverse g-factor

Figure 5-3 (a) indicates that a set of TRKR signal curves generated by the σ^- pump pulse under $\mathbf{B} = 0 \sim 452$ mT in Voigt geometry. Under the transverse magnetic field \mathbf{B} , RESP precesses with the Larmor frequency ω_L that is given by $\omega_L = g_{\perp}\mu_B B / \hbar$. The observed signal of RESP precession was fitted well by an exponentially damped oscillation function containing the beating frequency ω_L and an initial phase shift ϕ , as we mentioned; in the equation: $S_K(t) = A^e \exp(-\frac{t}{T^*}) \cos(\omega_L t + \phi)$, where $S_K(t)$ corresponds to Kerr rotation angle of the probe pulse for recording the RESP precession, the coefficient A^e is the amplitude of RESP, t is the pump-probe delay, T^* is almost the transverse spin-relaxation time T_2^* , as explained in Chapter 2.

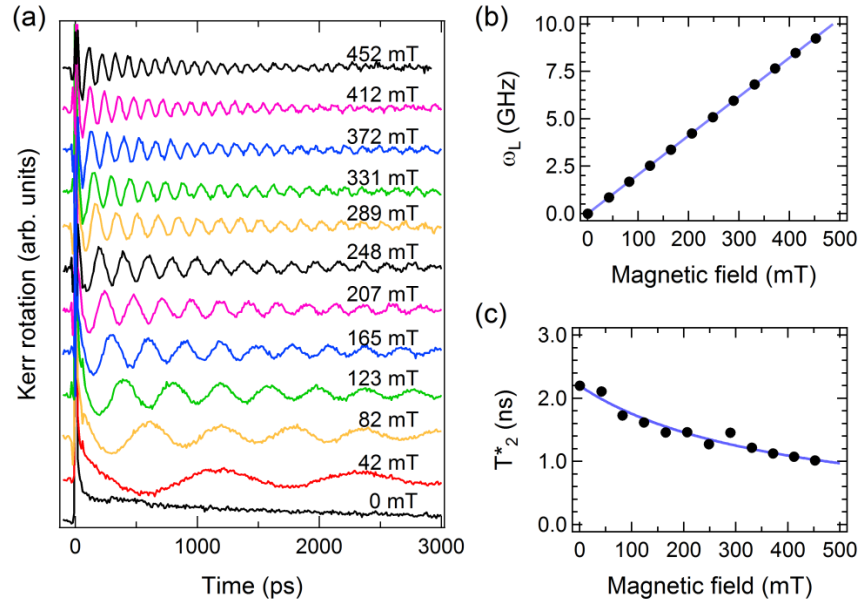


Figure 5-3: (a) The magnetic field strength dependence of TRKR signals $S_K(t)$ in Voigt geometry; (b) Observed Larmor frequencies in different magnitude from 0 mT to 452 mT; (c) The dependence of T^* on the magnetic field in the same range. The solid curve indicates the expected values assuming the Gaussian distribution of g factor with the FWHM of $\Delta g = 0.009$.

From these signals, the Larmor frequency increases linearly by $\omega_L(B)/(2\pi)(GHz) = 0.02056 B(mT)$ as shown in **Figure 5-3** (b). Then, the magnitude of the in-plane g factor $|g_{\perp}| = 1.468 \pm 0.003$ is deduced, which is comparable to the literature data measured by spin-flip Raman scattering method [38] and TRKR method [39].

Looking close to the signal damping, the T^* of RESP is found to decrease from 2198 ps at 0 mT to 1016 ps at 452 mT as shown in **Figure 5-3** (c). This reduction can be explained by the distribution of g_{\perp} due to the inhomogeneous fluctuation of well width and the alloy composition of the barrier material. Assuming Gaussian distribution of g_{\perp} with the FWHM of Δg_{\perp} , the relation $1/T^*(B) = 1/T^*(0) + \Delta g_{\perp} \mu_B B / \hbar$ can be applied. From the experimental data, Δg_{\perp} and $T_2^*(0)$ was estimated to be 0.009 ns and 2.2 ns.

Note that this reduction of T_2^* originates from an effect of the macroscopic averaging of individual spin precession with slightly different ω_L via the g_{\perp} distribution.

B. Longitudinal g-factor

Even under the tilted magnetic field, there is not any build-up effective nuclear polarization field \mathbf{B}_N via the σ^+/σ^- alternating polarization excitation at 50 kHz provided by a PEM, since nuclear spin build-up time is much longer than the polarization modulation period. Therefore, the Larmor frequency of RESP is decided by an effective g factor and the external magnetic field in the (x, z) plane without any nuclear field. In this case, $|g_{\theta}|$ is determined by the components of the g tensor along and normal to the plane as a following function [40]:

$$|g_{\theta}| = \sqrt{(g_{\perp} \cos \theta)^2 + (g_{\parallel} \sin \theta)^2} \quad \text{Eq. 5-4}$$

The effective g_{θ} factor values of fitting TRKR curves obtained from external magnetic field \mathbf{B} of 170 mT are varying between 1.468 and 1.480 with the tilted angle (θ) of applied magnetic field to sample plane as displayed in **Figure 5-4**. This means that g -factors have a large anisotropy: $g_{\parallel} \neq g_{\perp}$. By using the relationship in **Eq. 5-4** and the observed in-plane component ($g_{\perp} = 1.468$) as mentioned above, the g -factor perpendicular to the sample plane of $|g_{\parallel}| = 1.562 \pm 0.003$ can be evaluated. Due to the strongly anisotropic g -factors, an actual angle φ between the sample plane and the Larmor frequency vector $\Omega_L = g_{\theta}\mu_B B/\hbar$ is different from θ , which is slightly tilted away from the magnetic field direction. Likewise, the angle φ changes with the oblique magnetic field angle.

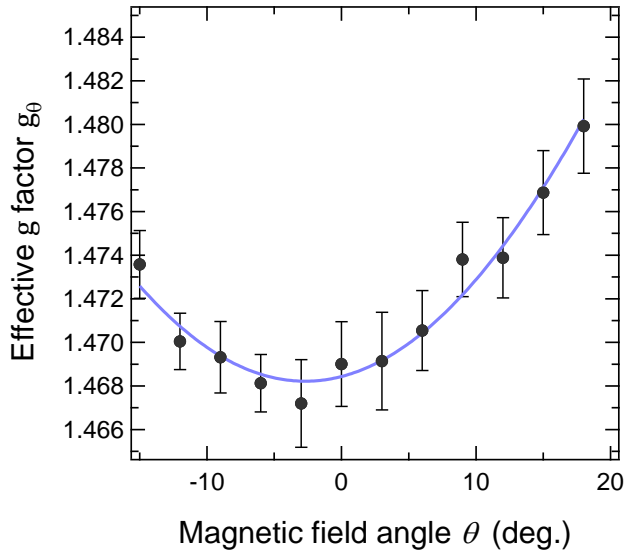


Figure 5-4: Effective g factor g_θ of RESP measured by using a PEM with different tilted angle θ of magnetic field. The solid line is a fitting curve according to Eq. 5-4.

5.3.2 Nuclear Field on Magnetic Field Angle

The key feature for the nuclear spin polarization generation is that the precession frequency is reduced due to the effective magnetic field B_N , which can be indicated by the changing in the precession frequency of Kerr rotations for PEM (blue curve) and σ^- (green curve) pump in **Figure 5-5**. The Larmor frequency for σ^- pump is reduced to 3.500 GHz from 3.544 GHz for PEM at $\theta = 18^\circ$ and $B = 170$ mT.

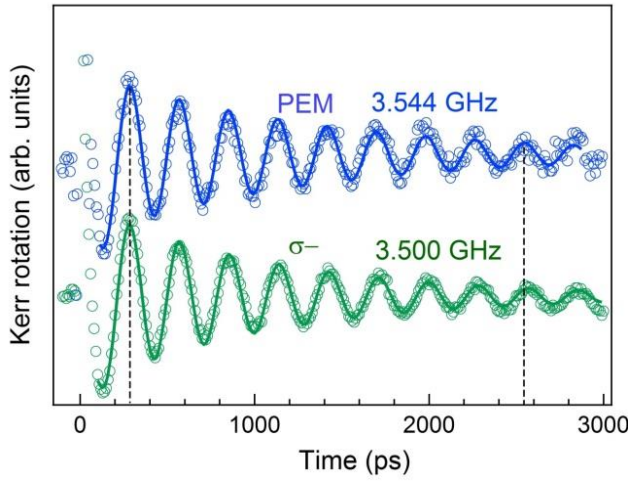


Figure 5-5: TRKR signals after PEM (upper) and σ^- (lower) pump excited at $\theta = 18^\circ$, $B = 170$ mT, $T = 9$ K.

As a consequence, there are nonprecessing spin component S_{\parallel} and precessing component S_{\perp} of the electron spin under the oblique magnetic field in TRKR signal, according to **Figure 5-1** (b). Therefore, the Kerr rotation angle $S_K(t)$ as a function of the pump-probe time delay is expressed by the following function exhibiting two kinds of exponential decays:

$$S_K(t) = A_{\parallel}^e \exp\left(\frac{-t}{T_{\parallel}^*}\right) + A_{\perp}^e \exp\left(\frac{-t}{T_{\perp}^*}\right) \cos(\bar{\omega}_{\perp} t + \phi) \quad \text{Eq. 5-5}$$

where the coefficients A_{\parallel}^e and A_{\perp}^e are proportional to the amplitudes of nonprecessing spin component S_{\parallel} and precessing component S_{\perp} in the polar Kerr effect scheme; T_{\parallel}^* and T_{\perp}^* are the longitudinal and transverse spin relaxation times of RESP, respectively.

Based on this kind of sample setup described by **Figure 5-1**, a set of TRKR curves have been measured via changing the direction of constant applied magnetic field of 170 mT. Then through **Eq. 5-5**, all the Larmor frequencies acquired from fitting TRKR exponential curves for PEM and σ^- pump excitation are shown in **Figure 5-6** (a),

which indicates that Larmor frequency could vary depending on the effective nuclear field and the changing g-factor induced by the tilted direction of applied magnetic field. The Larmor-frequency under σ^- pump excitation clearly decreases with increasing the tilted angle from -15° to 18° .

In the case of σ^- pump excitation, the nuclear effective field obtained under the tilted external magnetic field of around 170 mT is plotted as a function of the tilting angle in **Figure 5-6** (b). Its absolute value tended to increase as the magnetic field angle increases, as **Figure 5-6** (b) displays. The data displays a pronounced symmetry with the sign of angle. This is because the spin component S_{\parallel} , in proportion to the negative of $\sin\theta$, increases with the increasing absolute inclination of applied magnetic field. Obviously we can notice that the nuclear magnetic field value B_N (from 1.8 mT to -2.1 mT) changes in the same way that is proportional to $-\sin\theta$ of the tilted angle (between -15° and 18°). Thus the available nuclear field for applying magnetic field perpendicular to QW sample plane should be $B_N(90^\circ) = -7.3$ mT, which is similar to that of reported QW [21] and CdTe bulk [41]. Nevertheless, this nuclear field is still much weaker than the value of 700 mT obtained in III-V semiconductors reported [42]. Therefore, the CdTe compound as a kind of II-VI compound semiconductors is attractive material for RESP application, because of small nuclear spins with small natural abundance compared with the most investigated materials such as GaAs and InAs.

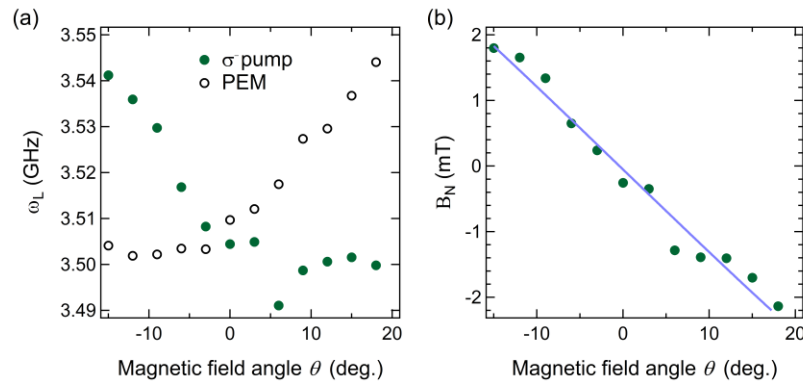


Figure 5-6: (a) Larmor frequencies of RESP measured for PEM model and σ -pump polarization excitations; (b) The effective nuclei magnetic field and its trendline for circularly polarized pump excitation at $T = 9$ K under the external magnetic field of 170 mT with different slope angle.

5.3.3 Nuclear Field on Magnetic Field Strength and Pump Power

HFI not only generates an effect on the precession of transverse component of RESP, but also induces a fast relaxation on the longitudinal component of electron spins. We mainly attribute the initial longitudinal polarization decay of RESP to the role of HFI. In turn, the RESP decay would influence the DNP generating rate. This is due to the fact that the nuclear spin polarization is formed through that residual electron spin component S_{\parallel} are reversely transferred to nuclear spin.

Figure 5-7 shows the effective nuclei magnetic field absolute values which are dependent on the varying external magnetic field strength (a) and the pump pulse power (b), respectively. In the presence of anisotropic g-factors, the average Larmor frequency under the combination of NSP effective field and external magnetic field was not totally collinear with the strong applied field from time to time. Then the larger transverse magnetic field will result in a faster decrease for the RESP. Therefore, the nuclear field with a long duration lifetime, when HFI reaches a balance, could decrease with the increasing external field, as shown in **Figure 5-7** (a), even a low magnetic field is

necessary for the dynamic nuclear polarization, in strong contrast to the findings in QDs [43]. However, the nuclear polarization changes with the excitation power nonlinearly indicated by **Figure 5-7** (b). In the first place, the RESP would go down quickly with the increasing electron spin density [44], which would give rise to the decline of HFI rate. In addition, the nuclear field rises with increasing the longitudinal RESP component seen from **Figure 5-6** (b), owing to the increased RESP by magnifying the excitation power. As a result, the nuclear field changes nonlinearly under the varying pulse power.

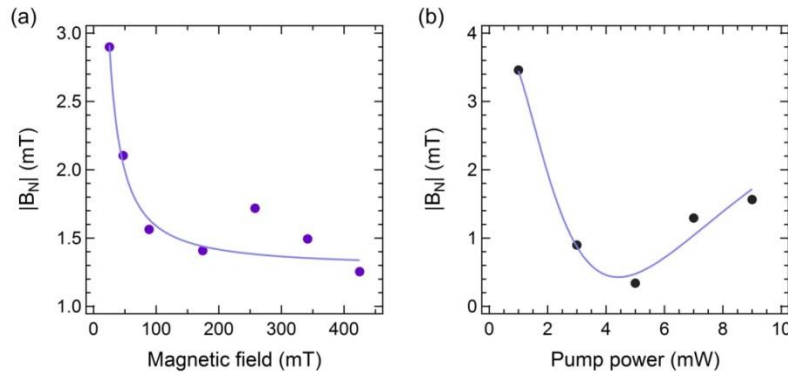


Figure 5-7: (a) The nuclear field and its trend line for pump power 9 mW on the dependence of the external magnetic field strength with the tilted angle of $\theta = 15^\circ$; (b) The nuclear field and its trend line with the varying pump excitation power under the external magnetic field of 88 mT at $\theta = 15^\circ$.

5.4 Theoretical Nuclear Field

In addition, the theoretical max value of \mathbf{B}_N along electron spin z direction can be obtained below. As given by Eq. 5-1, the hyperfine Hamiltonian is

$$H_{hf} = \sum_i p_i A_i |\Psi(R_i)|^2 \hat{I}_i S, \text{ Whilst, the hyperfine Hamiltonian causes a mean effective magnetic field } \mathbf{B}_N [45]:$$

$$\mathbf{B}_N^{\max} = \sum_i p_i A_i \langle I_i \rangle / (g_z \mu_B) \quad \text{Eq. 5-6}$$

where, $\langle I_i \rangle$ is the mean spin of the nuclei of the type i , not of the individual nuclei. Here, $i = \text{Cd}$ or Te in the CdTe compound and the nonzero nuclear spins are written here $I_{\text{Cd}} = I_{\text{Te}} = 1/2$; p_i is their corresponding abundances coefficient ($P_{\text{Cd}} = 25\%$; $P_{\text{Te}} = 8\%$); and A_i is the constant of HFI with the electron for each nuclei type ($A_{\text{Cd}} = 31\mu\text{eV}$ and $A_{\text{Te}} = 45\mu\text{eV}$) weighted by the overlap between electrons and nuclear spin learned from the reference [46]. Thus, the max value of \mathbf{B}_N : $\mathbf{B}_N^{\max} \sim 63$ mT for the 90° titled magnetic field in this QW has be expected by Eq. 5-6 with the previous g-tensor of $|g_\parallel| = 1.562$. Therefore, the measured nuclear polarization effective field factor $|B_N(90^\circ)/B_N^{\max}|$ will be 12% for a pump power of 10 mW with an expected external magnetic field along the sample growth direction. Although the generated BN is very small compared to the III-V semiconductors such as GaAs and InAs, the converted degree of NSP is comparable to $\langle I_i \rangle/I \sim 30\%$ in III-V semiconductor QDs [9] and is far beyond the value in thermal equilibrium.

In this dissertation, the effective nuclear field is about the order magnitude of few milli-Tesla, mainly due to double reasons potentially. One reason is the small effective strength of the hyperfine term in the CdTe nanostructure, because the hyperfine constant is weighted by the overlap between electrons and nuclear spin waves. In addition, the spin wave is quantized. Anyway, there is a small hyperfine constant in a CdTe QW, which is not preferable for studying DNP except evaluating RESP coupling with nuclear spins, but it gives quantum information great significance for RESP application. The other reason is as a result of the low electron probability density.

5.5 Summary

In this chapter, the DNSP was created via the HFI between nuclei spins and RESP after optically polarized negatively charged trions. To be specific, the resultant nuclear field was detected by using the TRKR technique in a tilted configuration. Non-precessing stationary component of RESP along the Larmor frequency vector was confirmed to be able to transfer the electron spin angular momenta to nonzero nuclear spins through a tilting angle of external magnetic field. For a picosecond circularly polarized excitation with ~ 10 mW in the oblique magnetic field of ~ 170 mT, the created NSP was found to produce an order of a few milli-Tesla of effective nuclear field B_N , which was much weaker than the value obtained in III-V semiconductor nanostructures, even the converted nuclear spin polarization was achieved up to 12% of the maximal NSP in the Faraday geometry. The value depends drastically on the applied external magnetic field and photo-injected electron spin polarization. Consequently we found CdTe is one of attractive compounds in terms of smaller effect of HFI due to its small abundance of the isotopes with one-half nuclear spin, compared to III-V semiconductors such as GaAs and InAs. Along with the feature of low nuclear field, the RESP performances are preferred for spintronic devices that require the long spin coherence and the manipulation at rather low magnetic fields.

5.6 References

- [1] X. M. Dou, B. Q. Sun, D. S. Jiang, H. Q. Ni, Z. C. Niu. Electron spin relaxation in a single InAs quantum dot measured by tunable nuclear spins[J]. *Phys. Rev. B* 2011; **84**: 033302.
- [2] Y. K. Kato, R. C. Myers, A. C. Gossard, D. D. Awschalom. Electron spin interferometry using a semiconductor ring structure[J]. *Applied Physics Letters* 2005; **86**: 162107.
- [3] G. Sukhodub, F. Hohls, R. J. Haug, D. K. Maude, D. Reuter, A. D. Wieck. Dynamics of nuclear spins appearing in transport measurements of an inter-edge spin diode in tilted magnetic fields[J]. *Physica. E: Low Dimens. Syst. Nanostruct.* 2006; **34**: 355-358.
- [4] J. Ishihara, M. Ono, G. Sato, S. Matsuzaka, Y. Ohno, H. Ohno. Magnetic Field Dependence of Quadrupolar Splitting and Nuclear Spin Coherence Time in a Strained (110) GaAs Quantum Well[J]. *Jpn. J. Appl. Phys.* 2011; **50**: 04DM03.
- [5] V. K. Kalevich, V. L. Korenev. Optical Polarization of Nuclei and ODNMR in GaAs/AlGaAs Quantum Wells[J]. *Appl. Magn. Reson.* 1991; **2**: 397-411.
- [6] B. Li, P. Coles, J. A. Reimer, P. Dawson, C. A. Meriles. Optical pumping of nuclear spin magnetization in GaAs/AlAs quantum wells of variable electron density[J]. *Solid State Commun.* 2010; **150**: 450-453.
- [7] R. Kaji, S. Adachi, H. Sasakura, S. Muto. Hysteretic response of the electron-nuclear spin system in single In(0.75)Al(0.25)As quantum dots: Dependences on excitation power and polarization[J]. *Phys. Rev. B* 2008; **77**: 115345.
- [8] M. S. Rudner, L. S. Levitov. Self-Sustaining Dynamical Nuclear Polarization Oscillations in Quantum Dots[J]. *Phys. Rev. Lett.* 2013; **110**: 086601.
- [9] R. Kaji, S. Adachi, H. Sasakura, S. Muto. Direct observation of nuclear field fluctuations in single quantum dots[J]. *Phys. Rev. B* 2012; **85**: 155315.
- [10] J. Kim, J. Puls, Y. S. Chen, G. Bacher, F. Henneberger. Electron-nuclear spin control in charged semiconductor quantum dots by electrical currents through micro-coils[J]. *Appl Phys Lett* 2010; **96**: 151908.
- [11] W. H. Lau, M. E. Flatte. Tunability of electron spin coherence in III-V quantum wells[J]. *Journal of Applied Physics* 2002; **91**: 8682-8684.

- [12] S. Crankshaw, F. G. Sedgwick, M. Moewe, C. Chang-Hasnain, H. L. Wang, S. L. Chuang. Electron Spin Polarization Induced by Linearly Polarized Light in a (110) GaAs Quantum-Well Waveguide[J]. *Phys. Rev. Lett.* 2009; **102**: 206604.
- [13] M. M. Glazov. Coherent spin dynamics of electrons and excitons in nanostructures (a review)[J]. *Phys. Solid State* 2012; **54**: 1-27.
- [14] A. Tackeuchi, T. Kuroda, S. Muto, Y. Nishikawa, O. Wada. Electron spin-relaxation dynamics in GaAs/AlGaAs quantum wells and InGaAs/InP quantum wells[J]. *Jpn. J. Appl. Phys.* 1999; **38**: 4680-4687.
- [15] A. V. Khaetskii, D. Loss, L. Glazman. Electron spin decoherence in quantum dots due to interaction with nuclei[J]. *Phys. Rev. Lett.* 2002; **88**: 186802.
- [16] R. Kaji, S. Ohno, T. Hozumi, S. Adachi. Effects of valence band mixing on hole spin coherence via hole-nuclei hyperfine interaction in InAlAs quantum dots[J]. *Journal of Applied Physics* 2013; **113**: 203511.
- [17] C. Testelin, F. Bernardot, B. Eble, M. Chamarro. Hole-spin dephasing time associated with hyperfine interaction in quantum dots[J]. *Phys. Rev. B* 2009; **79**: 195440
- [18] M. Fanciulli, P. Höfer, A. Ponti. Shallow donor electron spins as qubits in Si and SiGe: a pulsed ESR study[J]. *Physica B: Condensed Matter* 2003; **340–342**: 895-902.
- [19] J. Matsunami, M. Ooya, T. Okamoto. Electron spin resonance of the two-dimensional metallic state and the quantum Hall state in a Si/SiGe quantum well[J]. *Physica E-Low-Dimensional Systems & Nanostructures* 2006; **34**: 248-251.
- [20] I. Leung, C. Michal. Optical enhancement of NMR signals in CdTe[J]. *Phys. Rev. B* 2004; **70**: 035213.
- [21] C. Testelin, B. Eble, F. Bernardot, G. Karczewski, M. Chamarro. Signature of the Overhauser field on the coherent spin dynamics of donor-bound electrons in a single CdTe quantum well[J]. *Phys. Rev. B* 2008; **77**: 235306.
- [22] B. Eble, P. F. Braun, O. Krebs, L. Lombez, X. Marie, B. Urbaszek, et al. Spin dynamics and hyperfine interaction in InAs semiconductor quantum dots[J]. *Physica Status Solidi B-Basic Solid State Physics* 2006; **243**: 2266-2273.
- [23] G. Lampel. Nuclear Dynamic Polarization by Optical Electronic Saturation and Optical Pumping in Semiconductors[J]. *Phys. Rev. Lett.* 1968; **20**: 491-493.

- [24] J. A. Mcneil, W. G. Clark. Nuclear Quadrupolar Spin-Lattice Relaxation in Some 3-4 Compounds[J]. Phys. Rev. B 1976; **13**: 4705-4713.
- [25] D. Henriksen, T. Kim, I. Tifrea. Nuclear spin diffusion effects in optically pumped quantum wells[J]. Eur Phys J B 2014; **87**: 17.
- [26] A. Malinowski, M. A. Brand, R. T. Harley. Tilted-field exciton beats in a quantum well[J]. Solid State Commun. 2000; **116**: 333-337.
- [27] C. Latta, A. Srivastava, A. Imamoglu. Hyperfine Interaction-Dominated Dynamics of Nuclear Spins in Self-Assembled InGaAs Quantum Dots[J]. Phys. Rev. Lett. 2011; **107**: 167401.
- [28] B. Eble, P. F. Braun, O. Krebs, L. Lombez, X. Marie, B. Urbaszek, et al. Spin dynamics and hyperfine interaction in InAs semiconductor quantum dots[J]. physica status solidi (b) 2006; **243**: 2266-2273.
- [29] M. I. Dyakonov. Spin Physics in Semiconductors[B]. 2008.
- [30] G. Sukhodub, F. Hohls, R. J. Haug, D. K. Maude, D. Reuter, A. D. Wieck. Dynamics of nuclear spins appearing in transport measurements of an inter-edge spin diode in tilted magnetic fields[J]. Physica E: Low-dimensional Systems and Nanostructures 2006; **34**: 355-358.
- [31] M. Eickhoff, D. Suter. Pulsed optically detected NMR of single GaAs/AlGaAs quantum wells[J]. Journal of Magnetic Resonance 2004; **166**: 69-75.
- [32] M. Eickhoff, B. Lenzman, G. Flinn, D. Suter. Coupling mechanisms for optically induced NMR in GaAs quantum wells[J]. Phys. Rev. B 2002; **65**: 125301.
- [33] J. J. Baumberg, D. D. Awschalom, N. Samarth, H. Luo, J. K. Furdyna. Spin Beats and Dynamical Magnetization in Quantum Structures[J]. Phys. Rev. Lett. 1994; **72**: 717-720.
- [34] H. Chudo, C. Michioka, Y. Itoh, K. Yoshimura. Te-125 NMR studies of single-crystal CeTe₃[J]. Phys. Rev. B 2007; **75**: 045113.
- [35] G. P. Flinn, R. T. Harley, M. J. Snelling, A. C. Tropper, T. M. Kerr. Optically detected nuclear magnetic resonance in semiconductor quantum wells[J]. J. Lumin. 1990; **45**: 218-220.

- [36] S. E. Barrett, R. Tycko, L. N. Pfeiffer, K. W. West. DIRECTLY DETECTED NUCLEAR-MAGNETIC-RESONANCE OF OPTICALLY PUMPED GAAS QUANTUM-WELLS[J]. Phys. Rev. Lett. 1994; **72**: 1368-1371.
- [37] R. Tycko, S. E. Barrett, G. Dabbagh, L. N. Pfeiffer, K. W. West. ELECTRONIC STATES IN GALLIUM-ARSENIDE QUANTUM-WELLS PROBED BY OPTICALLY PUMPED NMR[J]. Science 1995; **268**: 1460-1463.
- [38] A. A. Sirenko, T. Ruf, M. Cardona, D. R. Yakovlev, W. Ossau, A. Waag, et al. Electron and hole g factors measured by spin-flip Raman scattering in CdTe/Cd_{1-x}MgxTe single quantum wells[J]. Phys. Rev. B 1997; **56**: 2114-2119.
- [39] E. A. Zhukov, D. R. Yakovlev, M. Bayer, G. Karczewski, T. Wojtowicz, J. Kossut. Spin coherence of two-dimensional electron gas in CdTe/(Cd,Mg)Te quantum wells[J]. physica status solidi (b) 2006; **243**: 878-881.
- [40] G. Salis, D. Awschalom, Y. Ohno, H. Ohno. Origin of enhanced dynamic nuclear polarization and all-optical nuclear magnetic resonance in GaAs quantum wells[J]. Phys. Rev. B 2001; **64**: 195304.
- [41] A. Nakamura, D. Paget, C. Hermann, C. Weisbuch, G. Lampel, B. C. Cavenett. Optical detection of electron spin resonance in CdTe[J]. Solid State Commun. 1979; **30**: 411-414.
- [42] A. Malinowski, R. T. Harley. Dynamic nuclear Overhauser shifts in Larmor beats from a quantum well[J]. Solid State Commun. 2000; **114**: 419.
- [43] G. Sallen, S. Kunz, T. Amand, L. Bouet, T. Kuroda, T. Mano, et al. Nuclear magnetization in gallium arsenide quantum dots at zero magnetic field[J]. Nat Commun 2014; **5**: 3268.
- [44] G. Wang, A. Balocchi, A. V. Poshakinskiy, C. R. Zhu, S. A. Tarasenko, T. Amand, et al. Magnetic field effect on electron spin dynamics in (110) GaAs quantum wells[J]. New J. Phys. 2014; **16**: 045008.
- [45] T. A. Kennedy, A. Shabaev, M. Scheibner, A. L. Efros, A. S. Bracker, D. Gammon. Optical initialization and dynamics of spin in a remotely doped quantum well[J]. Phys. Rev. B 2006; **73**: 045307.
- [46] I. A. Merkulov, A. L. Efros, M. Rosen. Electron spin relaxation by nuclei in semiconductor quantum dots[J]. Phys. Rev. B 2002; **65**: 205309.

CHAPTER 6

CONCLUSIONS AND OUTLOOK

6.1 Conclusions

To summarize, for studying the ensemble resident electron spin dynamics, a naturally n-doped CdTe/Cd_{0.85}Mg_{0.15}Te SQW with the well width of 30 monolayers (100 Å) grown by molecular-beam epitaxy on a (001)-GaAs substrate had been used to perform the TRKR experiments. All the experiments with the double lock-in detection techniques were carried out in a cold-finger optical cryostat set at the center of a magnet by a mode-locked Ti-doped sapphire laser (2-ps pulse width and 76-MHz pulse repetition rate). Through the experimental and theoretical analysis investigation, we have identified RESP formation process, as well as the relationship with the spin dynamics of bound trions and excitons. Furthermore, we investigated the manipulation of the ensemble spin coherence under low external magnetic fields after RESP forming.

This dissertation presents a transient IPS process via systematically investigating the precessional traces of RESP involving the trion and exciton spin dynamics in the SQW with the low-density resident electrons. All the above experimental results indicate that there was always remarkable negative IPS appeared for any TRKR signal at various conditions, which was identified as a result of the intrinsic spin polarization dynamics, especially confirmed by a more proof of the double pump excitation experiments. As a

result, the physical interpretation of initial phases in the RESP transient signals has been fully established.

What is more, this dissertation demonstrates that the absolute value of the negative IPS mainly increases with the excitation power. Moreover, it changes nonlinearly with the Larmor frequency. Additionally, the pulse photon energy in the range of $1.6035 \text{ eV} \sim 1.6127 \text{ eV}$, around the transition energy in resonance with trion, has a negligible effect on the negative IPS. However, the absolute value of the negative IPS for RESP (as the weak precessional signal with a long transverse decay time here) quickly starts to raise with the photon energy increases from 1.6131 eV to 1.6164 eV after just passing over the neutral exciton resonance. Thus, combined with the Kerr signals analysis, we concluded that the excitons perform another kind of spin dynamics with the exchange interactions between hole spins and electron spins.

Comparison of the experimental data with theory shows that the theoretical assumption is in good agreement with the experimental findings for all the overall trends of IPSs mentioned above. The calculation model presented in this work is just a concise model capturing the essential physics of many body effects about exciton, trion with RESP evolutions, respectively. Most of all, through the interpretation of the nonzero IPSs in the RESP precessions, the trion spin dynamical process and the RESP formation can be determined in the calculations as well as in the experiments, where the briskly asymmetric hole spin reversal accounts for the negative initial phase. For such a scenario, the negative IPS can come out as far as there is a one-way fast hole spin flip-stop from T^{\Downarrow} to T^{\Uparrow} alone under σ^- polarized excitation, vice versa for σ^+ excitation, especially shorter than their recombination time.

This research also indicates that RESP gave rise to a little NSP by the non-precessing stationary component along Larmor frequency vector: an effective nuclear field of a few mT ups to 12% of the maximal NSP for a picosecond circularly polarized excitation with 10 mW in the oblique magnetic field of 170 mT at 9 K, which was extremely weak compared with that in III-V semiconductor nanostructures as expected. The RESP performances with the feature of low nuclear field are preferred for spintronic devices which require the long spin coherence and the manipulation at rather low magnetic fields.

6.2 Outlook

We believe that the results presented in this dissertation will be valuable and can contribute to the better manipulation and understanding of the RESP and charged excitons dynamics. The clear physical picture of the resident electron spin dynamic allows us to apply RESP better in future.

Non-degenerate pump and probe would be used to further explore the spin dynamics in excitons by ruling out the possibility of light holes' effect.

Moreover, the more relationship between the specific behaviors of hole spin relaxation and reversal with the internal quantum environment should be confirmed again by a kind of combined experiment of time/polarization-resolved photoluminescence excitation/emission. The more samples with varying the density of excess electrons and the controllable subtle imperfections would be used to investigate more trion spin dynamics mechanisms. Meanwhile, the potential impurities and strain in the lattice structure might be measured without destroying the sample in the future technology.

ACKNOWLEDGMENTS

The work in this dissertation has required the great help of a number of people, whom I would like to thank here for helping to make this work possible.

Firstly, I would like to express my forever deep and sincere gratitude to my advisor, mentor: Prof. S. Adachi. Thanks to his hands-on approach to the wise and patient education, guidance and encouragement, I have learnt more than I ever could have achieved by only reading any book or any literature over the past 3 years. In addition, those he strived for perfection in almost every aspect, paid attention to academic exchanges; the spirit of never giving up, as well as improving experimental conditions and the description and analysis meticulously, in combination with his friendly, helpful and tolerant excellent qualities have given me the extremely valuable tools to be a brand-new and real mature person, and a useful scientific worker. The ordinary words "thank", "grateful" are so mild and entirely inadequate to express how much grateful I am.

Secondly, my gratitude extends to Prof. R. Kaji for her constant intellectual, mental assistance and incredible ability to explain things. I always could get comprehensive, coherent, specific and in-depth explanation from her to clear up my confusion and to greatly enrich my knowledge whenever I need.

Additionally, thanks to all colleagues, past and present, of the laboratory of ultrafast quantum optics. I never forgot the huge help from Mr. Ohno, Mr. Yokoyama, Mr. Kurosawa, Mr. Hozumi, Mr. Makita, Mr. Hsu. Particularly, Mr. Ohno often imparted

his some expertise to me. Moreover, Mr. Kurosawa gave me a step-by-step guide and experience on any devices and more advices for handling everything from experiments to traditional custom behaviors. The special thanks go to the current kind colleagues and friends in our lab: Mr. Hatanaka, Mr. Fujiwara, Mr. Tomi, especially Mr. Kawakami, who spent the time and effort in helping me a great deal during my experiments. They have always been infinitely generous with their time and knowledge. Furthermore, without their companionship, PhD graduate life in Hokkaido University would have been rather tough.

Also, I would like to thank Prof. S. Muto and Prof. N. Nishiguchi, who taught me a lot about quantum nanostructures, information and physics theory during my course period. Additional thanks to other professors and doctors especially from other universities of Universität Regensburg, Sakarya University, University of Oregon, University of Science and Technology of China, the University of Hong Kong, who carefully answered me any basic and even stupid questions by email and on the telephone, taught me various quantum physics and optics knowledge and experience, especially when I just stepped into this scientific field.

Finally I would like to thank my family, who try their best to get me better education. Especially my brother spiritually and financially supported me time and again. And my grandparents' most endless love gave me the strength to move forward. Also, thanks to my husband Dr. Liu for help in improving this dissertation work. Moreover, China Scholarship Council is acknowledged for the studentship financial support at Hokkaido University. For most of them, I find an ordinary "thank you" is simply not enough.

LIST OF PUBLICATIONS

Publications

1. "Negative initial phase shift of Kerr rotation generated from the building-up process of resident electron spin polarization in a CdTe single quantum well", L. Yan, M. Kurosawa, R. Kaji, G. Karczewski, S. Takeyama, and S. Adachi. *Physical Review B* **90**, 205307/1-6 (2014).
2. "Effective nuclear field measurement in a single quantum well via time-resolved Kerr rotation technique", L.-P. Yan, R. Kaji, and S. Adachi. *Advanced Materials Research* **936**, 534-539 (2014).
3. "Optical detection of anisotropic g factor and nuclear spin polarization in a single CdTe quantum well", L. Yan, M. Kurosawa, W.-T. Hsu, W.-H. Chang, S. Adachi. *Japanese Journal of Applied Physics* **54**, 033003/1-4 (2015).

Conferences

1. "Effective nuclear field measurement in a single quantum well via time-resolved Kerr rotation technique" (oral) L.-P. Yan*, R. Kaji, and S. Adachi. International Conference on Materials Science and Engineering Technology (MSET 2014) (Shanghai, China, 28-29 June, 2014).
2. "Resident electron spin polarization via trion dynamics in a single quantum well" (19a-A27-4) L.-P. Yan*, S. Adachi, and R. Kaji, 第 75 回応用物理学会秋季学術講演会 (2014 年 9 月 17-20 日, 北海道大学札幌キャンパス).
3. "Resident electrons spin formation and spin dephasing in a single CdTe quantum well" (poster and short oral), L.-P. Yan*, W.-T. Hsu, and S. Adachi. International Conference on Solid State Devices and Materials (SSDM13) (Fukuoka, Japan, 24-27 September, 2013).
4. "Optical detection of nuclear spin polarization in a single CdTe quantum well" (12p-PA1-6) 黒澤雅博, 巖麗平*, 錫治怜奈, 足立智. 第 73 回応用物理学会秋季学術講演会 (2012 年 9 月 11-14 日 愛媛大学・松山大学).

